

Changes of valence state and local structure in anode materials for lithium-ion batteries by X-ray absorption spectroscopy

vorgelegt von

Master of Science in Engineering

Dong Zhou

von der Fakultät III – Prozesswissenschaften
der Technischen Universität Berlin
zur Erlangung des akademischen Grades

Doktor der Ingenieurwissenschaften

-Dr. -Ing.-

genehmigte

Dissertation

Promotionsausschuss:

Vorsitzender: Prof. Dr. Aleksander Gurlo

Gutachter: Prof. Dr. John Banhart

Gutachter: Prof. Dr. Christiane Stephan-Scherb

Gutachter: Dr. Tobias Placke

Tag der wissenschaftlichen Aussprache: 24th. July. 2017

Berlin 2017

Abstract

Electronic and local structural changes in three different promising anode materials (porous NiSi₂/Si composite, nano-crystalline NiFe₂O₄ and ZnFe₂O₄) for lithium ion batteries are investigated by X-ray absorption spectroscopy. The lithium storage mechanism and associated structural changes are derived not only from the average valence states of the absorption atoms (Ni, Fe and Zn) estimated from the X-ray absorption near-edge spectra (XANES), but also from the fitting of the extended X-ray absorption fine structure (EXAFS) with theoretical models.

The NiSi₂ phase of the porous NiSi₂/Si composite shows a strong Ni-Si metal-metal bond character and partially reacts with lithium during lithiation and de-lithiation, forming a non-stoichiometric compound NiSi_{2-y} with the same crystal structure as that of NiSi₂. The NiSi₂ phase of the composite acts mainly as a buffer in order to accommodate the huge volume changes during lithium alloying/de-alloying with silicon.

As for the nano-crystalline NiFe₂O₄, Fe³⁺ ions are firstly reduced and move from tetrahedral sites to empty octahedral sites, followed by the conversion reaction during the 1st discharge process. Upon continuous lithiation, highly disordered metallic Fe/Ni nanoparticles are formed and during subsequent lithium extraction, the metallic nanoparticles are re-oxidized to Fe₂O₃ and NiO phases, respectively, instead of the original NiFe₂O₄ spinel.

Similar to NiFe₂O₄, lithium insertion into nano-crystalline ZnFe₂O₄ occurs with the collapse and transition of spinel matrix to FeO and ZnO phases. However, unlike FeO, ZnO is only partially reduced with further lithiation. A mixture of metallic iron, ZnO, metallic zinc, LiZn and Li₂O phases seems to be formed in the first deep lithiation. During the subsequent de-lithiation in the 1st cycle, part of the iron and zinc nanoparticles are re-oxidized to Fe₂O₃ and ZnO phases, respectively. Moreover, the redox activity of the transition metal oxides are much improved in the 2nd cycle. The poor reversible electrochemical properties of the nano-crystalline ZnFe₂O₄ anode may mainly be attributed to the unreactive ZnO in the electrode during cycling.

Zusammenfassung

Elektronische und lokale strukturelle Änderungen in drei unterschiedlichen erfolgversprechenden Anodenmaterialien (poröser NiSi₂/Si Verbundwerkstoff, nano-kristallines NiFe₂O₄ und ZnFe₂O₄) für Lithiumionen-Batterien wurden mittels Röntgenabsorptionsspektroskopie untersucht. Der Lithium Speicherungsmechanismus und damit verbundene strukturelle Änderungen werden abgeleitet aus den mittleren Valenzzuständen der Absorptionsatome (Ni, Fe und Zn) bestimmt aus den Nahkanten-Absorptionsspektren und aus den Anpassungen theoretischer Modelle an die Röntgenabsorptionsspektren.

Die NiSi₂ Phase des porösen NiSi₂/Si Verbundwerkstoffes zeigt einen starken Ni-Si Metal-Metal Bindungscharakter und partielle Reaktionen mit Lithium während der Lithium Einlagerung und Extraktion, welche eine nicht-stöchiometrische NiSi_{2-y}-Verbindung mit der gleichen Kristallstruktur wie NiSi₂ bildet. Die NiSi₂ Phase des Komposits fungiert hauptsächlich als Puffer um die riesigen Volumenänderungen während der Legierungsbildung mit Silikon anzupassen.

In nano-kristallinem NiFe₂O₄, werden zunächst Fe³⁺ Ionen reduziert, welche sich dabei von tetraedrischen Plätzen zu leeren oktaedrischen Plätzen bewegen, gefolgt von der Konversionsreaktion während des ersten Entladungsprozesses. Bei kontinuierlicher Entladung bilden sich stark ungeordnete metallische Fe/Ni Nanopartikel, und während der darauf folgenden Lithium Extraktion werden die metallischen Nanopartikel zu Fe₂O₃- bzw. NiO-Phasen oxidiert anstatt zu dem ursprünglichen NiFe₂O₄ Spinell.

Ähnlich wie bei NiFe₂O₄ ist die Lithium Einlagerung in nano-kristallines ZnFe₂O₄ verbunden mit dem strukturellen Übergang der Spinell Matrix zu FeO und ZnO Phasen. Anders als bei FeO, wird ZnO bei weiterem Einlagern von Lithium jedoch nur partiell reduziert. Während der ersten tiefen Lithium Einlagerung scheint sich eine Mischung von metallischem Eisen, ZnO, metallischem Zink, LiZn und Li₂O Phasen zu bilden. Während der darauf folgenden Lithium Extraktion im ersten Zyklus wird ein Teil der Eisen- und Zink-Nanopartikel zu Fe₂O₃ bzw. ZnO re-oxidiert. Darüber hinaus ist die Redox Aktivität der Übergangsmetall-Oxide im zweiten Zyklus viel besser. Die schlechten reversiblen elektrochemischen Eigenschaften der nano-kristallinen ZnFe₂O₄ Anode sind teilweise verursacht durch das unreaktive ZnO in der Elektrode während des Zyklirens.

Contents

1 Introduction.....	- 1 -
1.1 Introduction to lithium ion batteries.....	- 1 -
1.2 Current status of the electrode materials for lithium ion batteries.....	- 3 -
1.3 Advantages of X-ray Absorption Spectroscopy (XAS) and goals of the thesis.....	- 6 -
2 Experimental.....	- 11 -
2.1 Physics of XAS.....	- 11 -
2.2 Experiment.....	- 13 -
2.2 Sample preparation.....	- 13 -
2.3 XAS data analysis.....	- 14 -
2.4 Modelling theory for XAS.....	- 15 -
3 Published parts of work.....	- 19 -
3.1 Porous NiSi ₂ /Si composite anode material.....	- 20 -
3.1.1 Supporting information.....	- 35 -
3.2 Nano-crystalline NiFe ₂ O ₄ anode material.....	- 37 -
3.2.1 Supporting information.....	- 55 -
3.3 Nano-crystalline ZnFe ₂ O ₄ anode material.....	- 62 -
4 Conclusions.....	- 82 -
5 Outlook.....	- 84 -
6 Acknowledgements.....	- 85 -

1 Introduction

1.1 Introduction to lithium ion batteries

With the increasing demand of energy consumption in the world, exploration of renewable energy is urgently required due to the unsustainable nature of traditional energy sources and the decrease of CO₂ emission. Therefore, in the last two centuries a large amount of research[1, 2] is focused on the application of the environmental friendly alternative energies, such as solar energy, wind energy, nuclear energy *etc.*. Concurrently, development of the efficient energy storage and mobile systems is becoming more and more unavoidable because of the unstable nature of these renewable energies. In this regard, rechargeable lithium ion batteries are well positioned to act as portable stores of electric power compared to other energy storage systems due to their high energy (gravimetric and volumetric), long cycle life and low self-discharge property[3, 4].

Lithium ion batteries were proposed by M. Stanley Whittingham in 1970s[5] and firstly commercialized in 1990 by Sony Company[6]. A lithium ion battery is a transducer that works by converting chemical energy into electrical energy during discharge and vice versa. It contains three major components: anode, cathode and electrolyte. The anode is the source of lithium ions and the cathode is the tank for lithium ions. The electrolyte is a conductor which allows the ionic and electronic transportation.

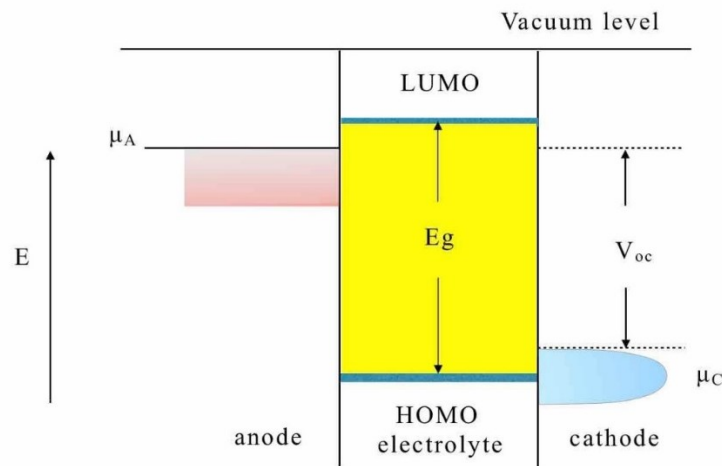


Fig. 1.1 Relative energies of electrode potentials versus the LUMO-HOMO window of the electrolyte[7].

Reprinted with permission from Ref.7.

1. Introduction

The potential of the battery not only depends on the electrochemical potential differences between the cathode and anode, but also strongly on the HOMO-LUMO energy gap (E_g) of the electrolyte. If the electrochemical potential of the anode (μ_A) is higher in energy than the LUMO of the electrolyte, the electrolyte itself will be reduced instead of the anode. On the other hand, if the electrochemical potential of the cathode (μ_C) is lower in energy than the HOMO of the electrolyte, the electrolyte will be oxidized, as shown in Fig. 1.1. The stability of electrolyte should not be overlooked during the designing of lithium ion cell.

In the first generation lithium ion batteries, graphite and layered LiCoO_2 were used as the negative and positive electrode, respectively. A porous lithium ion permeable membrane made of polypropylene/polyethylene is placed between the anode and cathode in order to get rid of the short circuit caused by the direct contact of electrodes. The lithium storage mechanism is shown in Fig. 1.2 based on the following reactions:

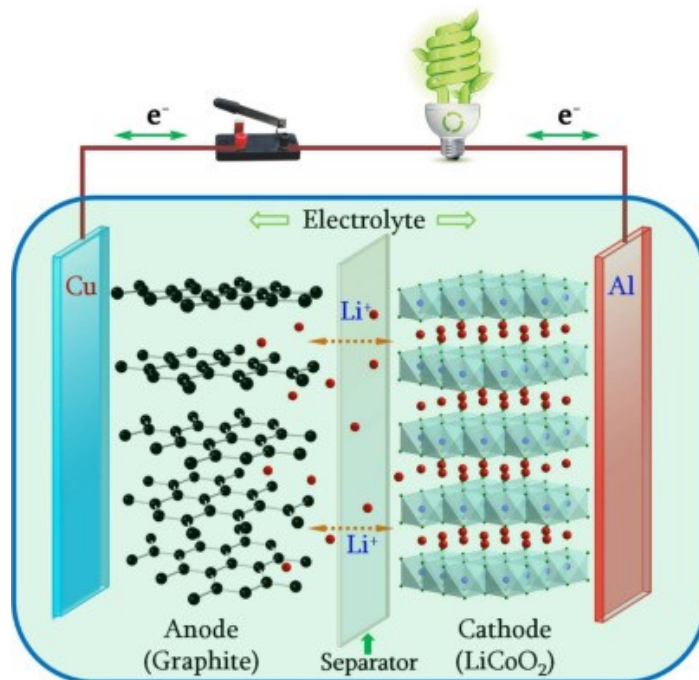
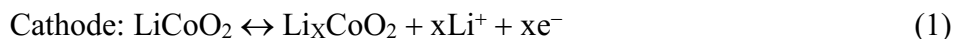


Fig. 1.2 Schematic diagram of the first generation lithium ion batteries based on the intercalation/de-intercalation reaction[8]. Reprinted with permission from Ref.8.

During charging, Li^+ ions are extracted from the layered LiCoO_2 cathode and inserted into the graphite anode. Meanwhile, the electrons travel through the external electrical circuit to compensate the extra positive charge in the anode. A reverse reaction can be observed during the discharging process.

The successful application of lithium ion batteries in portable devices such as cell phones, laptops and other digital electronics strongly boosts the economic growth of the world and improves the quality of human being's life. However, the low energy density and power of present lithium ion batteries are bottlenecks which impede the development of the electric vehicles (EV) industry and other emerging applications[4]. The demand for better performance of lithium ion batteries had never been so intense.

1.2 Current status of the electrode materials for lithium ion batteries

Incremental progresses have been witnessed in intercalation materials in the past 40 years under the continuous efforts of chemistry and materials scientists[9, 10]. In 1983, Thackeray *et al.*[11] proposed the spinel LiMn_2O_4 cathode material which drew much interest due to its excellent rate performance. However, it is plagued by the self-discharge phenomenon when stored under full charge. Then, in 1997, Padhi *et al.*[12] discovered the electrochemical properties of the olivine phase LiFePO_4 which gave a comparable high capacity of 170 Ah/kg with a discharge potential at about 3.4 V vs Lithium. This discovery had a big impact in electrochemical energy storage since it was the first potential cathode material which was much cheaper and more environmental friendly than LiCoO_2 . Unfortunately, this material could only achieve its theoretical capacity partially at room temperature due to the low conductivity caused by the low lithium diffusion at the electrode/electrolyte interface[13]. Many research groups are still working on the materials now and are trying to solve this problem[14-17]. Meanwhile, in 1999 Liu *et al.*[18] announced the mixed $\text{LiNi}_{1-y-z}\text{Mn}_y\text{Co}_z\text{O}_2$ layered compound with the lithium insertion capacities over 150 mAh g^{-1} . Many groups subsequently intended to find out the relation between the ratio of the three transition metal atoms and their corresponding electrochemical performance[19-22].

As a counter part of cathode, graphite is the most widely used anode due to its low cost, low working potential vs. lithium and long service life. However, the formation of the electronically

1. Introduction

insulating solid electrolyte interface (SEI) on the surface of the graphite spoils its capacity a lot. In 1994, the spinel structured $\text{Li}_4\text{Ti}_5\text{O}_{12}$ (LTO) was firstly reported by Thackeray's group as a substitute anode material for graphite[23]. Unlike graphite, $\text{Li}_4\text{Ti}_5\text{O}_{12}$ has no strain and volume change during discharge and charge process resulting in an excellent cyclic stability. More importantly, it can get rid of the SEI formation with a high working potential (1.5 V vs. Li/Li^+) and show a high specific capacity ($\sim 170 \text{ mAh g}^{-1}$)[24]. Unfortunately, the low electronic conductivity $\sim 10^{-13} \text{ S cm}^{-1}$ and moderate diffusion coefficient of lithium ions hinder its application at high discharge and charge rates. Materials scientists are now trying to settle these issues by surface coating and reducing the size of LTO particles[25-27].

Due to the intrinsic limitation of all the intercalation materials from both redox mechanism and structural aspects in terms of capacity, metallic alloys have drawn much attention after being proposed as high capacity electrode materials based on the alloying reaction[28]. Extensive investigations were carried out in the electroactive metals and semiconductors such as Si[29-32], Sn[33, 34], Al[35-37], Ga[38], Ge[39, 40], Pb[41] and Sb[42, 43] since they can react with lithium and form different Li-M phases reversibly during the discharge-charge process. Among these materials, Si is the most promising material as it has both the highest gravimetric capacity (4200 mAh g^{-1}) and volumetric capacity (9786 mAh cm^{-3}) compared to others[44]. The high specific capacity of Si is coming from alloying formation with inserted lithium ions as $\text{Li}_{12}\text{Si}_7$, Li_7Si_3 , $\text{Li}_{13}\text{Si}_4$ and $\text{Li}_{22}\text{Si}_5$ in different steps[45].

Although, these metal alloy electrodes show an extremely high reversible capacity, the unavoidable huge volume modification during lithiation/de-lithiation leads to a poor cycling life and large capacity loss[46, 47]. Several strategies[48-51] have been proposed and used to alleviate the effects of volume changes. One main approach is to optimize the content ratios of the active material, conductive additive and polymeric binder in the electrode and it has already been proved very successfully in Sn-based negative anodes[44]. Another main strategy is to design an intermetallic $\text{M}_1\text{-M}_2$ composite system[49, 51-54]. If the M_1 and M_2 are both electrochemically active to lithium ions, it is believed that the phases formed during the lithiation process can mutually buffer each other so as to suppress the volume expansion to some extent and achieve better stability of the electrode[51]. If one metal of the intermetallic $\text{M}_1\text{-M}_2$ composite system is inactive, it will serve as the buffer matrix to prevent volume changes[55, 56].

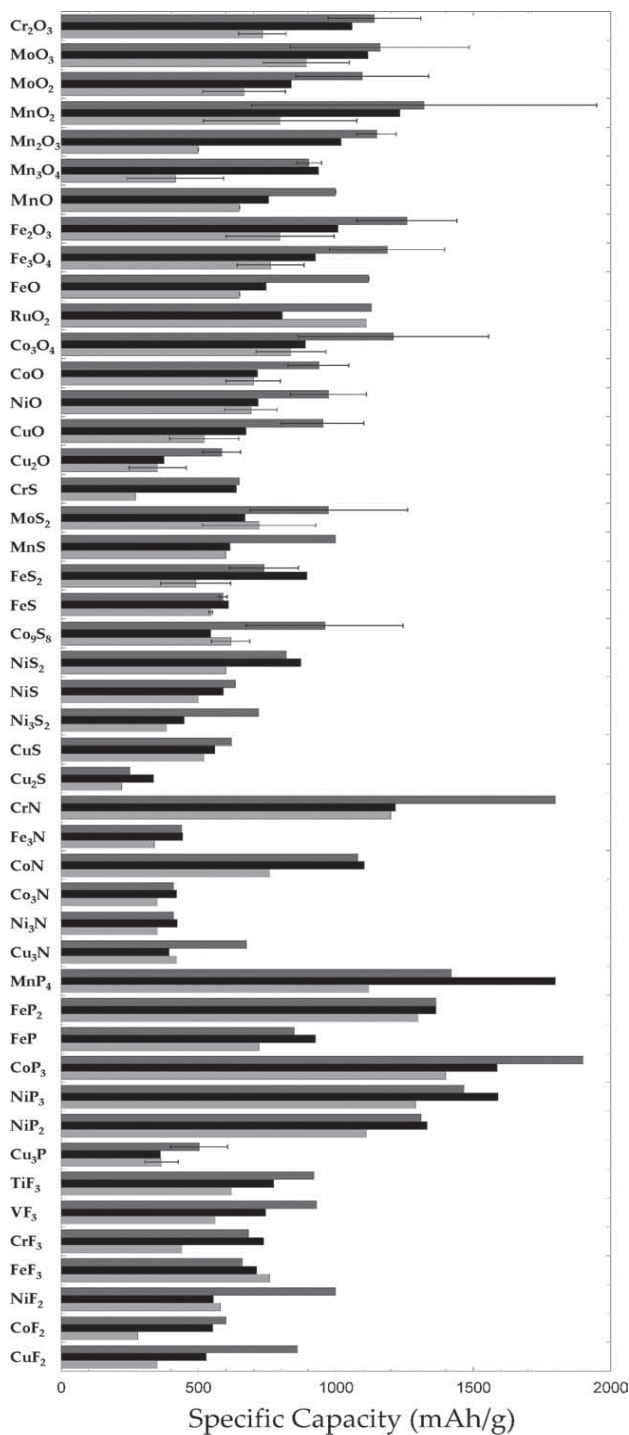
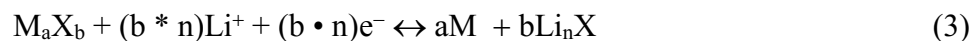


Fig.1.3 Electrochemical properties of different transition metal compounds that react with lithium through the conversion reaction [44]. Notations: black bars, dark grey and light grey represent the theoretical, first discharge, and charge gravimetric capacities, respectively. The “error” bars are provided as an indication of the dispersion of values reported in different literatures. Data with no bar is taken from a single literature source. Reprinted with permission from Ref.44.

In 2000, Poizot *et al.*[57] found that nano-sized transition metal oxides can reversibly react with lithium based on the conversion reaction, which delivered stable gravimetric capacities three times higher than that of carbon. This brought a new opportunity to explore materials for the substitutions of current graphite anodes with better performance. The conversion reaction is generalized as follows:



Where M = transition metal, X = anion (O, S, N, P and F), and n = formal oxidation state of X.

The forward reaction of the conversion reaction is proved to be thermodynamically favorable. However, the key to the reaction in the backward direction seems to depend on the decomposition of the lithium binary compound (Li_nX) when a reverse potential is applied since formation of Li^+ from Li_nX is thermodynamically unfavorable. It is believed that the reduced nano metal particles facilitate the Li_nX decomposition process. Although the conversion reaction has already been reported for various compounds with high capacity as shown in Fig. 1.3, several obstacles such as the poor structural integrity and cycling performance, large energy density loss and voltage hysteresis, are still need to be addressed before the commercial implementation.

1.3 Advantages of X-ray Absorption Spectroscopy (XAS) and goals of the thesis

Although, various techniques such as X-ray diffraction (XRD), neutron diffraction, Transmission Electron Microscopy (TEM), X-ray photoelectron spectroscopy (XPS), Mössbauer spectroscopy *etc.* have already been used and showed powerful ability to characterize the structural changes and reaction mechanism of lithium ion batteries during Li extraction/insertion. The following advantages of XAS make it unique to the lithium-ion battery research:

- (1) As an element-specific probe, XAS provides both electronic and physical information of each absorber atom contained in the material.
- (2) Practically, XAS measurements can be performed with any atom in any state of organization.
- (3) The results of XAS are more statistically reliable than other localized probe techniques since it averages the local structure from several square millimeters on the sample.

- (4) XAS can provide not only surface but also bulk information of the material depending on the measuring mode.

In this thesis, X-ray absorption spectroscopy measurements were performed at various states of discharge and charge in three potential anode materials for next generation lithium-ion battery: the porous NiSi₂/Si composite, spinel NiFe₂O₄ and ZnFe₂O₄ ferrites. The porous NiSi₂/Si composite is one of the most representatives of the intermetallic M₁-M₂ composite system, while NiFe₂O₄ and ZnFe₂O₄ attract a lot of interest from the materials scientist. All of them show several times higher capacities (NiSi₂/Si composite: 1856 mA h g⁻¹, NiFe₂O₄: 1534 mAh g⁻¹ and ZnFe₂O₄: 1590 mAh g⁻¹) than the commercial graphite anode (~370 mA h g⁻¹) during the first lithiation. However, how lithium ions react with these three materials during lithiation/delithiation process is still not well understood yet. The goals of this thesis are to understand the lithium storage mechanism and associated electronic and local structural changes in the three different anode systems of current interest.

References:

- [1] O. Ellabban, H. Abu-Rub, F. Blaabjerg, *Renewable and Sustainable Energy Reviews* 39 (2014) 748-764.
- [2] N.Y. Amponsah, M. Troldborg, B. Kington, I. Aalders, R.L. Hough, *Renewable and Sustainable Energy Reviews* 39 (2014) 461-475.
- [3] J.B. Goodenough, K.-S. Park, *J Am Chem Soc* 135 (2013) 1167-1176.
- [4] M. Armand, J.M. Tarascon, *Nature* 451 (2008) 652-657.
- [5] M.S. WHITTINGHAM, *Science* 192 (1976) 1126-1127.
- [6] Y. Nishi, *The Chemical Record* 1 (2001) 406-413.
- [7] J.B. Goodenough, *Accounts of Chemical Research* 46 (2013) 1053-1061.
- [8] C. Liu, Z.G. Neale, G. Cao, *Materials Today* 19 (2016) 109-123.
- [9] M.S. Whittingham, *Chem Rev* 104 (2004) 4271-4302.
- [10] B.L. Ellis, K.T. Lee, L.F. Nazar, *Chem Mater* 22 (2010) 691-714.
- [11] M.M. Thackeray, W.I.F. David, P.G. Bruce, J.B. Goodenough, *Mater Res Bull* 18 (1983) 461-472.
- [12] A.K. Padhi, K.S. Nanjundaswamy, J.B. Goodenough, *J Electrochem Soc* 144 (1997) 1188-1194.
- [13] A. Yamada, S.C. Chung, K. Hinokuma *J Electrochem Soc* 148 (2001) A224-A229.
- [14] H. Huang, S.-C. Yin, L.F. Nazar, *Electrochemical and Solid-State Letters* 4 (2001) A170-A172.
- [15] F. Croce, A. D' Epifanio, J. Hassoun, A. Deptula, T. Olczac, B. Scrosati, *Electrochemical and Solid-State Letters* 5 (2002) A47-A50.
- [16] S.-Y. Chung, J.T. Bloking, Y.-M. Chiang, *Nat Mater* 1 (2002) 123-128.
- [17] P.S. Herle, B. Ellis, N. Coombs, L.F. Nazar, *Nat Mater* 3 (2004) 147-152.
- [18] Z. Liu, A. Yu, J.Y. Lee, *J Power Sources* 81-82 (1999) 416-419.
- [19] O. Tsutomu, M. Yoshinari, *Chem Lett* 30 (2001) 642-643.

- [20] J.K. Ngala, N.A. Chernova, M. Ma, M. Mamak, P.Y. Zavalij, M.S. Whittingham, *J Mater Chem* 14 (2004) 214-220.
- [21] Y. Sun, C. Ouyang, Z. Wang, X. Huang, L. Chen, *J Electrochem Soc* 151 (2004) A504-A508.
- [22] D.D. MacNeil, Z. Lu, J.R. Dahn, *J Electrochem Soc* 149 (2002) A1332-A1336.
- [23] E. Ferg, R.J. Gummow, A. de Kock, M.M. Thackeray, *J Electrochem Soc* 141 (1994) L147-L150.
- [24] S.Y. Yin, L. Song, X.Y. Wang, M.F. Zhang, K.L. Zhang, Y.X. Zhang, *Electrochim Acta* 54 (2009) 5629-5633.
- [25] W.J.H. Borghols, M. Wagemaker, U. Lafont, E.M. Kelder, F.M. Mulder, *J Am Chem Soc* 131 (2009) 17786-17792.
- [26] M.V. Reddy, G.V. Subba Rao, B.V.R. Chowdari, *Chem Rev* 113 (2013) 5364-5457.
- [27] D. Peramunage, K.M. Abraham, *J Electrochem Soc* 145 (1998) 2609-2615.
- [28] J. Yang, M. Winter, J.O. Besenhard, *Solid State Ionics* 90 (1996) 281-287.
- [29] M.T. McDowell, I. Ryu, S.W. Lee, C. Wang, W.D. Nix, Y. Cui, *Adv Mater* 24 (2012) 6034-6041.
- [30] X.H. Liu, J.W. Wang, S. Huang, F. Fan, X. Huang, Y. Liu, S. Krylyuk, J. Yoo, S.A. Dayeh, A.V. Davydov, S.X. Mao, S.T. Picraux, S. Zhang, J. Li, T. Zhu, J.Y. Huang, *Nat Nano* 7 (2012) 749-756.
- [31] S.W. Lee, M.T. McDowell, J.W. Choi, Y. Cui, *Nano Lett* 11 (2011) 3034-3039.
- [32] M. Pharr, K. Zhao, X. Wang, Z. Suo, J.J. Vlassak, *Nano Lett* 12 (2012) 5039-5047.
- [33] L. Xu, C. Kim, A.K. Shukla, A. Dong, T.M. Mattox, D.J. Milliron, J. Cabana, *Nano Lett* 13 (2013) 1800-1805.
- [34] B. Wang, B. Luo, X. Li, L. Zhi, *Materials Today* 15 (2012) 544-552.
- [35] J. Benson, S. Boukhalifa, A. Magasinski, A. Kvit, G. Yushin, *ACS Nano* 6 (2012) 118-125.
- [36] Y. Liu, N.S. Hudak, D.L. Huber, S.J. Limmer, J.P. Sullivan, J.Y. Huang, *Nano Lett* 11 (2011) 4188-4194.
- [37] C.J. Wen, B.A. Boukamp, R.A. Huggins, W. Weppner, *J Electrochem Soc* 126 (1979) 2258-2266.
- [38] J. Saint, M. Morcrette, D. Larcher, J.M. Tarascon, *Solid State Ionics* 176 (2005) 189-197.

- [39] L. Baggetto, P.H.L. Notten, *J Electrochem Soc* 156 (2009) A169-A175.
- [40] S. Yoon, C.-M. Park, H.-J. Sohn, *Electrochemical and Solid-State Letters* 11 (2008) A42-A45.
- [41] M. Martos, J. Morales, L. Sánchez, *Electrochim Acta* 48 (2003) 615-621.
- [42] J. Wang, I.D. Raistrick, R.A. Huggins, *J Electrochem Soc* 133 (1986) 457-460.
- [43] A. Dailly, J. Ghanbaja, P. Willmann, D. Billaud, *Electrochim Acta* 48 (2003) 977-984.
- [44] J. Cabana, L. Monconduit, D. Larcher, M.R. Palacín, *Adv Mater* 22 (2010) E170-E192.
- [45] C.J. Wen, R.A. Huggins, *J Solid State Chem* 37 (1981) 271-278.
- [46] A. Timmons, J.R. Dahn, *J Electrochem Soc* 153 (2006) A1206-A1210.
- [47] M.M. Thackeray, J.T. Vaughey, C.S. Johnson, A.J. Kropf, R. Benedek, L.M.L. Fransson, K. Edstrom, *J Power Sources* 113 (2003) 124-130.
- [48] J.-B. Kim, H.-Y. Lee, K.-S. Lee, S.-H. Lim, S.-M. Lee, *Electrochem Commun* 5 (2003) 544-548.
- [49] M.D. Fleischauer, J.M. Topple, J.R. Dahn, *Electrochemical and Solid-State Letters* 8 (2005) A137-A140.
- [50] U. Kasavajjula, C. Wang, A.J. Appleby, *J Power Sources* 163 (2007) 1003-1039.
- [51] H. Kim, J. Choi, H.J. Sohn, T. Kang, *J Electrochem Soc* 146 (1999) 4401-4405.
- [52] X. Fan, H. Zhang, N. Du, P. Wu, X. Xu, Y. Li, D. Yang, *Nanoscale* 4 (2012) 5343-5347.
- [53] M.-S. Park, S. Rajendran, Y.-M. Kang, K.-S. Han, Y.-S. Han, J.-Y. Lee, *J Power Sources* 158 (2006) 650-653.
- [54] D. Zhou, H. Jia, J. Rana, T. Placke, R. Klöpsch, G. Schumacher, M. Winter, J. Banhart, *J Power Sources* 324 (2016) 830-835.
- [55] T. Kim, S. Park, S.M. Oh, *Electrochem Commun* 8 (2006) 1461-1467.
- [56] S. Zhou, X. Liu, D. Wang, *Nano Lett* 10 (2010) 860-863.
- [57] P. Poizot, S. Laruelle, S. Grugeon, L. Dupont, J.M. Tarascon, *Nature* 407 (2000) 496-499.

2 Experimental

2.1 Physics of XAS

X-rays are a form of electromagnetic radiation with a wavelength ranging from 0.01 to 10 nanometers which can be absorbed by all matter through the photo-electric effect. According Beer-Lambert's law, when an X-ray beam transmitted through a sample as shown in Fig 2.1, the absorption co-efficient $\mu(E)$ can be given as follows:

$$I_t = I_0 e^{-\mu(E)t} \quad (2.1)$$

$$\mu(E) t = \ln \left(\frac{I_0}{I_t} \right) \quad (2.2)$$

where I_0 is the intensity of incident X-ray on the sample, t is the sample thickness, and I_t is the intensity of transmitted X-ray through the sample. The absorption co-efficient $\mu(E)$ is highly related to the I_t , which describes the probability of the absorbed X-rays.

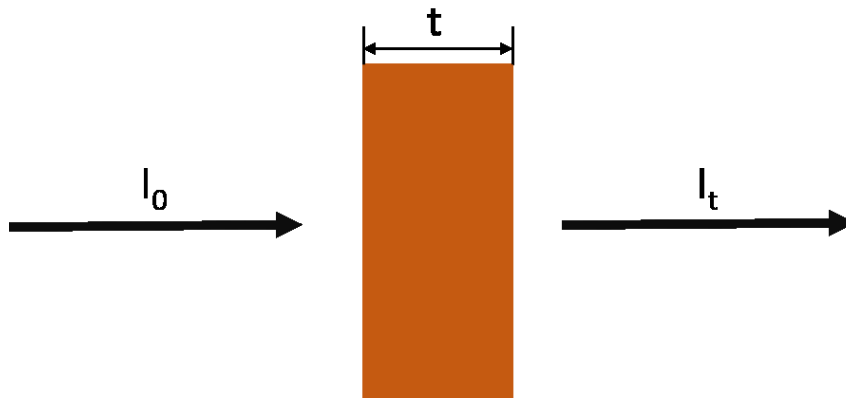


Fig. 2.1: Schematic view of X-ray absorption measurement

XAS concerns the variation of the intensity of $\mu(E)$ as a function of the incident X-ray energy. When the energy of incident X-ray equals to that of the binding energy of a core-level electron in absorbing atoms, a sharp rise can be observed in $\mu(E)$, which is called absorption edge. During the absorption event, the core electron is knocked out and becomes a photoelectron leaving a core hole in the core level. The ejected photoelectrons can either occupy the unoccupied bound states near the Fermi level or go into the continuum strongly depending on their kinetic energy. As can

2. Experimental

be seen in Fig 2.2, strong oscillations can be observed at the energy around the absorption edge (~ 50 eV) which is named as the X-ray Absorption Near Edge Structure (XANES) due to the dominant multiple scattering events of the photoelectrons with lower kinetic energy. Much qualitative information can be extracted from the XANES, such as chemical bonding, average valence state, crystal or cluster symmetry of the absorbing atoms.

If imaging the outgoing photoelectron as a spherical wave and the surrounding atoms as point scatters, the photoelectron wave can be backscattered by neighboring atoms and interferes with each other. Destructive and constructive interference can happen between these waves depending on the type of the atoms, the distance from the absorbing atoms to neighboring atoms and the wavelength of incident photon. This results in an interference pattern which shows up as a modulation in $\mu(E)$ with the change of incident X-ray energy during the experiment. The oscillatory part after XANES region of the absorption spectrum (between 50 eV – 1000 eV above the absorption edge) as shown in Fig 2.2, is called the Extended X-ray Absorption Fine Structure (EXAFS) which can provide quantitative information of the original absorbing atom such as coordination number, bond distance, static disorder and *etc.*

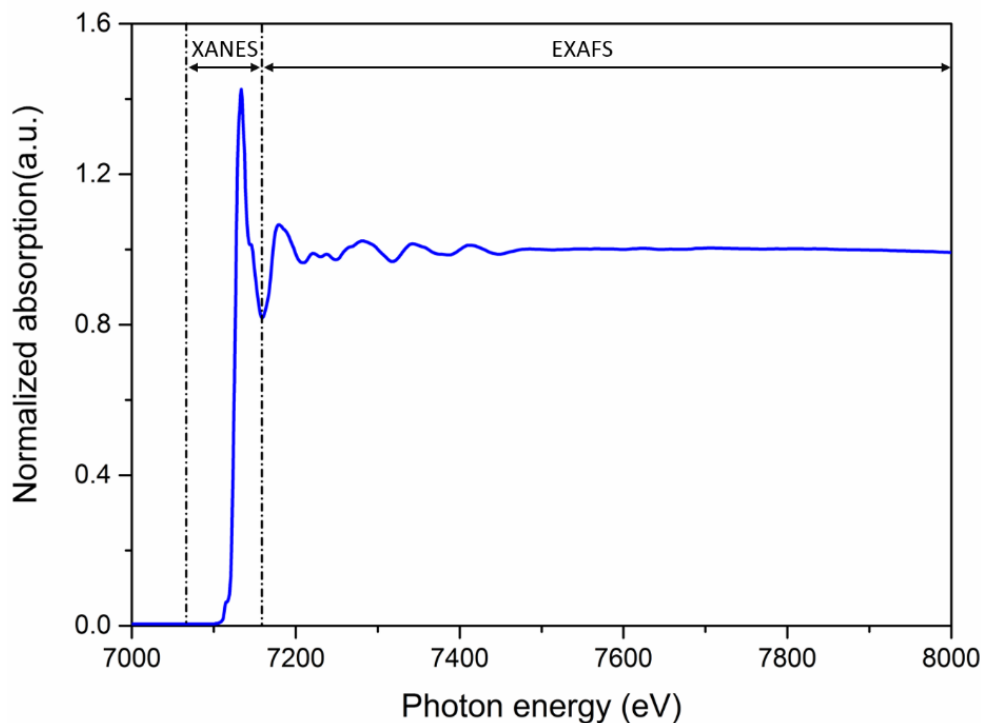


Fig. 2.2: Illustration of X-ray absorption spectrum using the reference of FeO.

2.2 Experiment

All XAS measurements in this thesis were performed in the transmission mode at the KMC-2 beamline of the synchrotron BESSY at Helmholtz-Zentrum Berlin, Germany. The X-rays were monochromatized by a graded Si-Ge (111) double crystal monochromator as shown in Fig. 2.3. Intensities of the incident beam, transmitted beam through the sample and reference foil were measured by three ionization chambers (I_1 , I_2 and I_3) filled with different gases in order to get a good signal-to-noise ratio. The total absorption in I_1 was about 10% by filling N_2 , while the absorption in I_2 was about 60-70 % by using a mixture of N_2 and Ar. I_3 absorbed the rest of the beam with fully filled pure Ar. Reference metal foil was measured simultaneously with the sample for the absolute energy calibration of the monochromator. Each sample was measured at least two times in order to ensure the recorded data was reproducible and reliable.

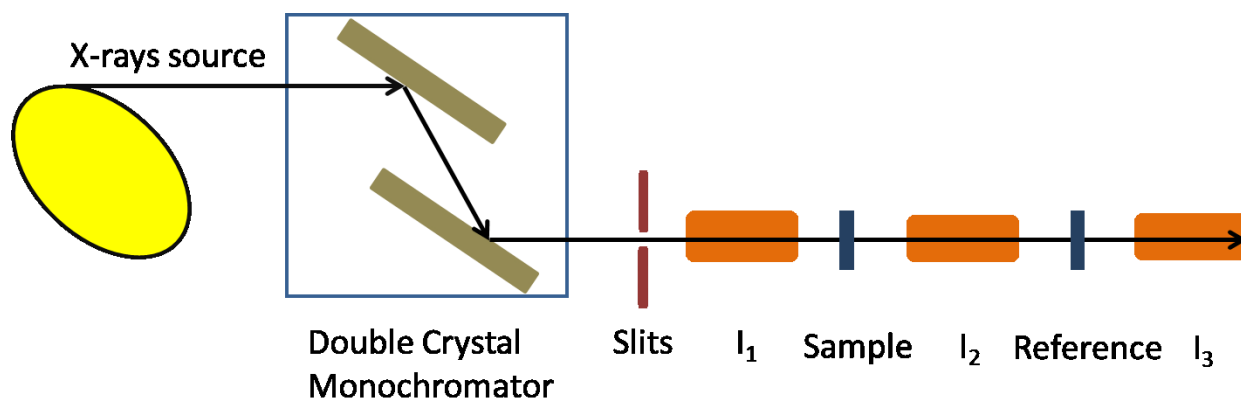


Fig. 2.3: Schematic illustration of XAS measurement in transmission mode.

2.2 Sample preparation

Sample preparation is one of the most important steps for XAS measurements. The quality of the XAS data measured in transmission mode is highly related to the way how the samples were prepared. If the sample is too thin, the random noise will destroy the signal due to insufficient absorption of the sample. If the sample is too thick, it will absorb so much that the small transmitted signals will be suppressed statistically. It has been reported that the best signal-to-noise can be achieved when the absorption length ($\mu(E) t$) of the sample equals 2.5[1]. The absorption length is the distance where the intensity of the incident beam reduces to 37% of its original intensity. Moreover, it is important to make sure that the sample is uniform and free of

2. Experimental

pinholes or cracks in order to get rid of the thickness-effect[2]. When the sample is thick enough, a significant decrease for the amplitude of the extended X-ray absorption fine structure can be observed due to the inevitable leakage radiation. In this thesis, the mass of the sample was calculated by the software *HEPHAESTUS* and about ~15mg of the material was used for each sample which is equivalent to $\mu(E) t = 2.5 \sim 3$ during the measurement. All the samples from the electrodes were sealed with Kapton tape in order to prevent the contamination from air as shown in Fig. 2.4.

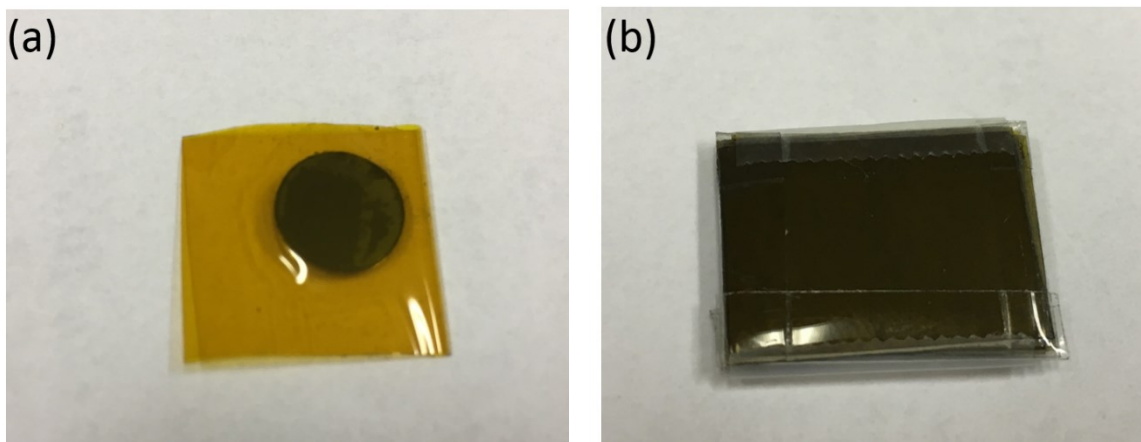


Fig. 2.4: Example of the samples for XAS measurement in transmission mode. (a) is an example for samples of NiFe_2O_4 anode and (b) is an example for samples of NiSi_2/Si composite and ZnFe_2O_4 anode.

2.3 XAS data analysis

The XAS data was firstly processed in the following steps by using the software *ATHENA* of the package *IFEFFIT* [3] before fitting to the model theory:

- (1) Converting measured XAS raw data to the absorption co-efficient $\mu(E)$.
- (2) Merging, deglitching, truncation and energy calibration of the scans.
- (3) Background removing by subtract the pre-edge and post-edge function.
- (4) Normalization of the absorption co-efficient.
- (5) Converting the data from E to k space.
- (6) Fourier transforming the $\chi(k)$ signal from k to R space.

The background is subtracted using *AUTOBK* algorithm in *ATHENA* by fitting the pre-edge and post-edge regions of an absorption spectrum which are extrapolated to the edge energy E_0 . Since

2. Experimental

the absorption co-efficient without neighboring atoms cannot be measured, the $\mu_0(E)$ is approximated by an adjustable spline. Therefore, the normalized $\chi(E)$ is obtained by dividing the subtracted spectrum to the edge step $\Delta\mu(E)$ according to:

$$\chi(E) = \frac{\mu(E) - \mu_0(E)}{\Delta\mu(E)} \quad (2.3)$$

Due to the wave-particle duality of the photoelectrons, $\chi(E)$ is then converted to $\chi(k)$ to relate $\chi(E)$ to structural parameters via Eq. 2.4:

$$k = \sqrt{\frac{2m(E - E_0)}{\hbar^2}} \quad (2.4)$$

Where m is the electron mass, E is the incident photon energy, E_0 is the threshold energy and \hbar is the reduced Plank's constant.

In order to emphasize the data in higher- k portion, the raw $\chi(k)$ is multiplied by K^3 . Since the scattering abilities of the neighboring atoms around the absorber vary a lot, $\chi(k)$ is composed of sine waves with different amplitude, frequency and phases. During Fourier transformation, the frequencies in $\chi(k)$ are filtered in distances R and window functions are used to avoid "ringing". In this thesis, the $\chi(k)$ was multiplied by the *Hanning* window with $dk = 1$, as reported before[4]. Peaks in $\chi(R)$ represent the coordination shells of the absorbing atoms. The amplitude of a peak is mainly depending on the type and number of neighboring atoms. While the Gaussian width of a peak represents the distribution and average atomic distance between the central absorber and its neighbors.

2.4 Modelling theory for XAS

Before extracting structural information from an EXAFS fit, it is necessary to understand each term in the EXAFS equation and how the equation was constructed. The absorption co-efficient μ can be estimated as follows with converting the energy E into the photoelectron wave vector k via Eq. 2.4[5] after various approximations[5-7]:

$$\chi(k) = \frac{1}{k R_j^2} \sum_j N_j S_o^2 F_j(k) e^{\frac{-2 R_j}{\lambda(k)}} e^{-2 \sigma_j^2 k^2} \sin(2kR_j + \phi_j(k)) \quad (2.5)$$

2. Experimental

$\frac{1}{k R_j^2}$: R_j is the atomic distance between the absorber and the j -type backscattering neighbor atom.

This $\frac{1}{k R_j^2}$ product make EXAFS a local probe which is sensitive to about 5 Å around the central absorbing atom. It also shows that EXAFS is strongly dependent on the photon energy due to the small wavelength of incident photon at very high k .

$N_j S_o^2$: N_j is the number of j -type atoms around the absorbers and S_o^2 is the amplitude reduction factor due to multi-electron excitations or many-body effects. When an X-ray photon is absorbed by an atom, an electron of the tightly bound inner state is ejected along with the excitation of the valence electrons from outer states, which is known as the multi-electron excitations. Therefore, the kinetic energy of the ejected photoelectron decreases resulting in the overall amplitude reduction of EXAFS oscillations. Normally, S_o^2 is a constant value between 0.7 – 1.0 for a given absorber since it accounts for the property of the absorbing atom[8, 9]. It is transferable for the samples measured under identical conditions and can be determined by fitting the reference compound with known structure and coordinates.

It is important to note that S_o^2 must be constrained when the number of j -type nearest neighbors N_j or the fraction of second phase containing the same absorbing atom needed to be refined.

$F_j(k)$: is the backscattering amplitude from each of the N_j neighboring atoms of the j -type. It only depends on the type of the backscatters.

$e^{-\frac{2 R_j}{\lambda(k)}}$: $\lambda(k)$ is the inelastic electron mean free path. The term $e^{-\frac{2 R_j}{\lambda(k)}}$ describes the inelastic losses in the scattering process which are primarily caused by the excitations of loosely bound valence electrons. It increases as the atomic number Z of the scatters decreases and it is higher for high order shells due to the large distances that photoelectron has to travel[10].

$e^{-2 \sigma_j^2 k^2}$: This term is defined as the EXAFS Debye-Waller factor, which contains important structural and chemical information. Unlike the Debye-Waller factor determined from X-ray diffraction, it is measured with respect to the absorbing atom. σ_j^2 is the Mean Squared Relative Displacement (MSRD) between absorber-scatter pairs, which estimates the distribution of the j -type neighboring atoms about its mean position R_j . Generally speaking, the σ_j^2 is affected by two components σ_{stat} (static disorder) and σ_{vib} (thermal vibrations). Thus, the structural disorder in a

2. Experimental

material subjected to physical or chemical treatment can be estimated by comparing the refined σ_j^2 if all the samples are identical and measured at the same temperature.

One thing need to be kept in mind is that both $N_j S_o^2$ and σ_j^2 can influence the EXAFS amplitude in a fit, errors in the determination of any term of them will introduce errors in the determination of other terms.

$\sin(2kR_j + \phi_j(k))$: The EXAFS oscillation can be treated as a sum of the interference $\sin(2kR_j + \phi_j(k))$ term with frequency $2R_j$ and phase $\phi_j(k)$ in k space. Since the total phase shift $\phi_j(k)$ depends on k and k depends on E_0 , the phase of the experimental $\chi(k)$ was aligned to that of the theoretical one by adjusting E_0 in the fit[10].

In this thesis, the terms such as $F_j(k)$, $\lambda(k)$ and $\phi_j(k)$ were calculated using *ab-initio* code *FEFF8.2* developed by Rehr's group[11]. All data were least-square fitted to the modelling theory using the software *ARTEMIS* of the package *IFEFFIT*[3]. The quality of a fit is estimated by the EXAFS R-factor which is given by Eq. 2.6:

$$R = \sum_{i=1}^N \frac{[\bar{\chi}(R_i)_{the} - \bar{\chi}(R_i)_{exp}]^2}{[\bar{\chi}(R_i)_{exp}]^2} \quad (2.6)$$

The R-factor describes the difference between the experimental data and theory at each data point i in complex Fourier transform space. For a good fit, the R-factor should be less than 0.02.

Reference

- [1] P.A. Lee, P.H. Citrin, P. Eisenberger, B.M. Kincaid, *Reviews of Modern Physics*, 53 (1981) 769-806.
- [2] E.A. Stern, K. Kim, *Physical Review B*, 23 (1981) 3781-3787.
- [3] B. Ravel, M. Newville, *Journal of Synchrotron Radiation*, 12 (2005) 537-541.
- [4] S. Kelly, D. Hesterberg, B. Ravel, *Methods of Soil Analysis Part 5*, 2008.
- [5] J.J. Rehr, R.C. Albers, *Reviews of Modern Physics*, 72 (2000) 621-654.
- [6] E.A. Stern, *Physical Review B*, 10 (1974) 3027-3037.
- [7] P.A. Lee, J.B. Pendry, *Physical Review B*, 11 (1975) 2795-2811.
- [8] J.J. Rehr, E.A. Stern, R.L. Martin, E.R. Davidson, *Physical Review B*, 17 (1978) 560-565.
- [9] E.A. Stern, B.A. Bunker, S.M. Heald, *Physical Review B*, 21 (1980) 5521-5539.
- [10] B.K. Teo, *EXAFS: Basic Principles and Data Analysis*, Springer, Berlin, 1986.
- [11] A.L. Ankudinov, B. Ravel, J.J. Rehr, S.D. Conradson, *Physical Review B*, 58 (1998) 7565-7576.

3 Published parts of work

3.1 Porous NiSi₂/Si Composite Anode Material (paper titled “Investigation of a Porous NiSi₂/Si Composite Anode Material Used for Lithium-Ion Batteries by X-Ray Absorption Spectroscopy”, Journal of Power Sources, 324 (2016) 830-835) [Accepted Version]

DOI: <https://doi.org/10.1016/j.jpowsour.2016.05.137>

Link: <http://www.sciencedirect.com/science/article/pii/S0378775316307017>

Own contributions: XAS sample preparation; results interpretation; manuscript composition and submission

3.1.1 Supporting information

3.2 Nano-crystalline NiFe₂O₄ Anode Material (“Investigation of Electronic and Local Structural Changes during Lithium Uptake and Release of Nano-crystalline NiFe₂O₄ by X-ray Absorption Spectroscopy”, Journal of Power Sources, 342 (2017) 56-63) [Accepted Version]

DOI: <https://doi.org/10.1016/j.jpowsour.2016.12.038>

Link: <http://www.sciencedirect.com/science/article/pii/S0378775316317335>

Own contributions: XAS sample preparation; results interpretation; manuscript composition and submission

3.2.1 Supporting information

3.3 Nano-crystalline ZnFe₂O₄ Anode Material (“Local structural changes of Nano-crystalline ZnFe₂O₄ during lithiation and de-lithiation studied by X-ray Absorption Spectroscopy”, Electrochimica Acta, 246 (2017) 699-706) [Accepted Version]

DOI: <https://doi.org/10.1016/j.electacta.2017.06.098>

Link: <http://www.sciencedirect.com/science/article/pii/S0013468617313361>

Own contributions: XAS sample preparation; results interpretation; manuscript composition and submission

3.1 Porous NiSi₂/Si composite anode material

Investigation of a Porous NiSi₂/Si Composite Anode Material Used for Lithium-Ion Batteries by X-Ray Absorption Spectroscopy

Dong Zhou^a, Haiping Jia^b, Jatinkumar Rana^a, Tobias Placke^b, Richard Klöpsch^b, Gerhard Schumacher^a, Martin Winter^b, John Banhart^{a,c}

^a Helmholtz-Zentrum Berlin für Materialien und Energie, Hahn-Meitner-Platz 1, 14109 Berlin, Germany

^b MEET Battery Research Center & Institute of Physical Chemistry, University of Münster, Corrensstr. 46&28/30, 48149 Münster, Germany

^c Technische Universität Berlin, Materials Science and Technology, Hardenberg str. 36, 10623 Berlin, Germany

Abstract

Local structural changes in a porous NiSi₂/Si composite anode material are investigated by X-ray absorption spectroscopy. It is observed that the NiSi₂ phase shows a strong metal-metal bond character and no clear changes can be observed in XANES during lithiation and de-lithiation. The variation of the number of nearest neighbors of the Ni atom for the 1st coordinate Ni-Si shell and σ^2 in the 1st cycle, both determined by refinement, demonstrates that NiSi₂ can partially react with lithium during discharge and charge. A partially reversible non-stoichiometric compound NiSi_{2-y} is formed during cell operation, the crystal structure of which is the same as that of the NiSi₂ phase. It can be concluded that NiSi₂ in the composite not only accommodates the pronounced volume changes caused by the lithium uptake into silicon, but also contributes to the reversible capacity of the cell.

1. Introduction

Silicon is one of the most promising anode materials for the next generation of high-performance lithium-ion batteries, and exhibits not only a moderate de-lithiation potential of 0.4 V vs. Li/Li⁺, but also the highest theoretical capacity (~3500 mA h g⁻¹), which is about one order of magnitude more than the capacity of commercially available graphite anode material (~370 mA h g⁻¹). Beside these advantages, several serious problems exist, such as tremendous volume changes

3.1 Porous NiSi₂/Si composite

($\geq 300\%$) during Li⁺ insertion/extraction and low electronic conductivity. Both impede the commercial application of silicon anodes up to now [1-4].

Three main approaches focusing on the modification and improvement of the active material have been proposed in order to overcome these drawbacks. The first approach follows earlier works on Sn based anode materials [5,6] and involves the use of nano-scaled materials such as nanowires [7], nanosheets [8], and nanotubes [9] instead of “classical” materials. The second approach involves designing new (e.g., porous, nanoweb and hierarchical) structures which can supply enough free space to accommodate the expansion of silicon [10-13]. The third approach has been demonstrated by several groups [14-16], and is based on introducing a volumetrically stable, highly electronically conducting second phase into the silicon host matrix which can act as a buffer to accommodate volume changes of silicon and maintain the electrode integrity. For example, Zhou et al.[16] synthesized a hetero-nanostructure consisting of two-dimensional TiSi₂ nano-nets and Si coating, which exhibited a capacity retention of $> 99\%$ per cycle at the level of $> 1000 \text{ mA h g}^{-1}$ over 100 cycles at the charging rate of 8400 mA g^{-1} . Liu et al. ball-milled Si and Ni powder jointly and then synthesized a porous NiSi/Si composite[15]. A big improvement of capacity retention compared to pure Si electrodes was observed. Kang et al. reported an amorphous-Si/NiSi_x core-shell nanowire anode, produced by a catalyst-free two-step SiH₄ chemical vapor deposition, and achieved high reversible capacities above 3000 mA h g^{-1} at a rate of 2C [17]. Recently, Jia et al. proposed a porous NiSi₂/Si/carbon core-shell structured anode material by using a ball milling and chemical vapor deposition (CVD) process, which resulted in a stable capacity of 1272 mA h g^{-1} for 200 cycles (at a rate of 1C) and a reversible capacity of 740 mA h g^{-1} (at 5C rate)[18]. However, the exact role of the NiSi₂ phase in the composite during discharge/charge remains unclear.

As a unique element-sensitive technique, X-ray absorption spectroscopy (XAS) has been shown to be useful to clarify the electronic configuration of absorbing atoms and their immediate neighborhood in different kinds of materials, e.g., in metal oxide cathodes in lithium-ion batteries [19-21] or polysulfide radicals in lithium/sulfur batteries [22,23]. The X-ray absorption near edge structure (XANES) is resulting from the transition of a core electron to bound states, which gives information about the oxidation state, site symmetry and the covalent bond strength of absorbing atoms. Extended X-ray absorption fine structure (EXAFS) spectra provide quantitative information about changes in the local structure absorbing atoms by the refinement, such as the

the metal-ligand bond length, coordination number and Debye-Waller factor. [24].

This paper reports local electronic and structural changes in a porous NiSi₂/Si anode material as revealed by X-ray absorption spectroscopy (XAS). X-ray absorption near edge structure (XANES) and extended X-ray absorption fine structure (EXAFS) were employed to elucidate the reaction mechanism between lithium and the NiSi₂ phase upon discharge or charge.

2. Experimental

Porous NiSi₂/Si composite was synthesized by high-energy ball milling followed by annealing at 900°C and washing according to the procedure described previously[18]. Since not the electrochemical performance but the activity of the NiSi₂ phase with respect to lithiation was in the focus of research, no additional carbon coating was applied. Inductively coupled plasma-optical emission spectrometry (ICP-OES) and X-ray diffraction (XRD) measurements were performed in order to determine the chemical composition and crystal structure, respectively, of the NiSi₂/Si composite by using a Bruker D8 Advance X-ray diffractometer equipped with a copper target X-ray tube, operated at a radiation wavelength of $\lambda = 0.154$ nm.

Composite electrodes were prepared by mixing 70 wt.% of active material (NiSi₂/Si composite powder), 15 wt.% of conductive carbon black C-nergy Super C65 (Imerys Graphite & Carbon) and 15 wt.% of sodium carboxymethylcellulose (CMC, Walocel CRT 2000 PA 12) as a binder. Before mixing with the solid compounds, the binder was firstly dissolved in deionized water to obtain a 2.0 wt.% solution. Then, Super C65 and the active material were added to the binder solution and stirred in order to homogenize the mixture. Afterwards, a high-energy dispersion step using an Ultra-Turrax T25 (1h at 5000 rpm) was conducted in order to eliminate particle agglomerates. The resulting paste was cast onto a copper current collector and dried in air for 1 h at 80 °C. Electrodes with an area of 40×40 mm² were cut out and dried under reduced pressure (< 0.1 mbar) at 120°C for 24 hours. The electrode contained ~ 3 mg cm⁻² of active material. Electrochemical experiments were accomplished by using two-electrode pouch cells with Celgard 2400 as the separator and high purity lithium metal (Rockwood Lithium) as the counter electrode. A solution of 1M LiPF₆ in 30 wt.% ethylene carbonate (EC) and 70 wt.% diethylcarbonate (DEC), was used as an electrolyte. All the cells were assembled in a dry room with an atmospheric water content of less than 10 ppm. The specific capacity was calculated on the basis of the total composite weight, and the C-rate was calculated with respect to the

3.1 Porous NiSi₂/Si composite

theoretical capacity of 2300 mAh g⁻¹ (1C) for the NiSi₂/Si composite. Galvanostatic experiments were performed in a Maccor 4300 battery test system at a charge/discharge rate of 0.1C in the voltage range of 1.5-0.02 V at 20 °C. The cells were charged or discharged to a certain state of charge, opened again in a dry room and the electrodes were washed with DEC solution in order to remove the electrolyte salt. In order to get a homogenous sample for XAS measurements, active materials were ground and coated on a Kapton tape (Goodfellow, 25µm thick) using brushes, after which the coated Kapton tape was cut into 8 pieces and sealed together to prevent exposure to air.

XAS measurements at the Ni K-edge on NiSi₂/Si composite samples at various state of 1st lithiation and de-lithiation were performed in the transmission mode at beamline KMC-2 of the BESSY-II synchrotron light source, Berlin, Germany. A graded Si-Ge (111) double crystal monochromator was used in this beamline and higher harmonics were rejected by detuning the monochromator such that the intensity of the beam at the sample location was 65% of the maximum possible intensity. Pure Ni foil was measured simultaneously with each sample for an absolute energy calibration of the monochromator. An ionization chamber filled with a mixture of argon and nitrogen was used to get an optimum signal-to-noise ratio.

The data were pre-processed as described elsewhere [25] using the software ATHENA of the package IFEFFIT [26]. All spectra were energy-calibrated with respect to the first peak in the derivative spectrum of pure nickel. Normalized EXAFS signals were transformed to *k* space and multiplied by *k*³ in order to compensate for the damping of signal at high *k*. Then the *k*³-weighted $\chi(k)$ signal was Fourier transformed and left uncorrected for a phase shift. A model function was generated by performing ab-initio calculations using the code FEFF8.2 [27] and least-square fitted to the data using the software ARTEMIS of the package IFEFFIT. The fitting parameters, amplitude reduction factor S_0^2 and an overall energy parameter ΔE_0 , were involved for each dataset. A fractional change α_{fit} of bond length for each coordination shell was refined such that a change in the bond length ΔR was calculated by $\Delta R = \alpha_{fit} \times R_{theory}$. Moreover, separate mean-squared relative displacement parameters σ^2 were given for each coordination shell depending on the type of backscattering atoms it contained and its mean distance from the central absorbing atom. The parameters for multiple scattering paths were constrained in terms of those of corresponding single scattering paths [28]. The statistical quality of each EXAFS fit was evaluated based on its R-factor.

3. Results

Fig. 1 shows the XRD powder diffraction patterns of the NiSi₂/Si composite and pure Si. All major reflections at 28.6°, 47.5°, 56.3°, 69.5° 76.5° and 88.6° of NiSi₂/Si composite can be indexed to the NiSi₂ (JCPDS 04-006-9129) and silicon (JCPDS 04-002-0118) phases, with a cubic crystal structure (space group: $Fm\bar{3}m$ for NiSi₂ and $Fd\bar{3}m$ for silicon respectively), which is consistent with results reported in the literature [18, 29]. However, because of the very small lattice mismatch (about 4%) between NiSi₂ and Si phase [30] and the very low intensity (specifically less than 1% compared to the main reflection) of the two additional peaks at 33.3° and 79.7° of NiSi₂ phase, no clear differences can be resolved between the XRD patterns of the two phases. ICP-OES measurements showed that the mass ratio of silicon and NiSi₂ in the composite is 50 wt.% and 50 wt.% respectively, which is consistent with the designed starting mass ratio of Si:Ni=3:1.

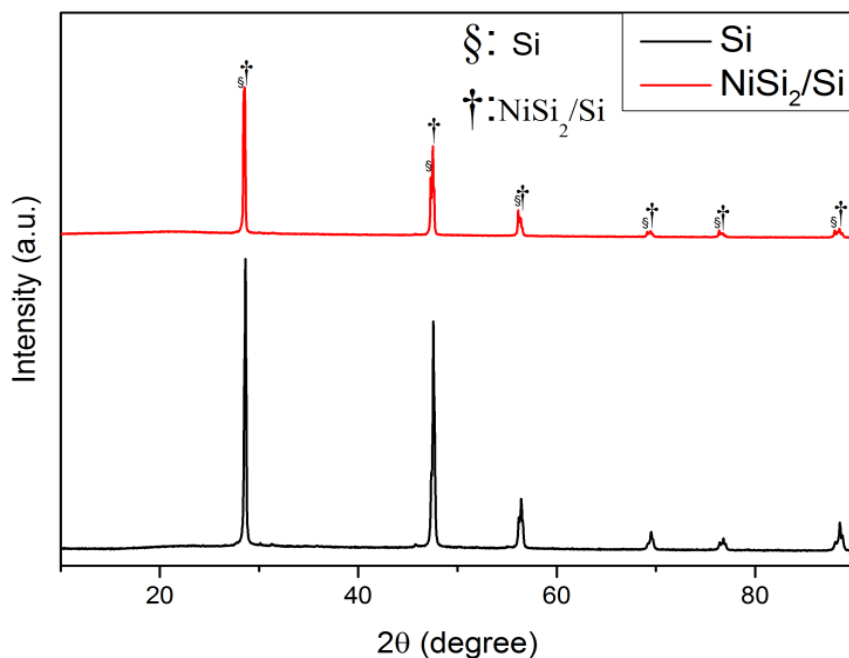


Fig. 1. XRD patterns of the NiSi₂/Si composite material (red line) and silicon (black line).

Discharge/charge voltage profiles for the 1st cycle of the NiSi₂/Si composite are given in Fig. 2. A specific capacity of 1856 mA h g⁻¹ is attained as the cell is lithiated to 0.02 V, while it delivers a capacity of 1372 mA h g⁻¹ as it is de-lithiated to 1.5 V with a first cycle coulombic efficiency of ~74%. The five marked circles at the voltage profiles (Fig. 2) display the five different states of

3.1 Porous NiSi₂/Si composite

charge studied by X-ray absorption spectroscopy (including XANES and EXAFS), i.e., pristine state, at 0.02 V (during discharge), at 0.3 V, 0.5 V and 1.5 V (during charge).

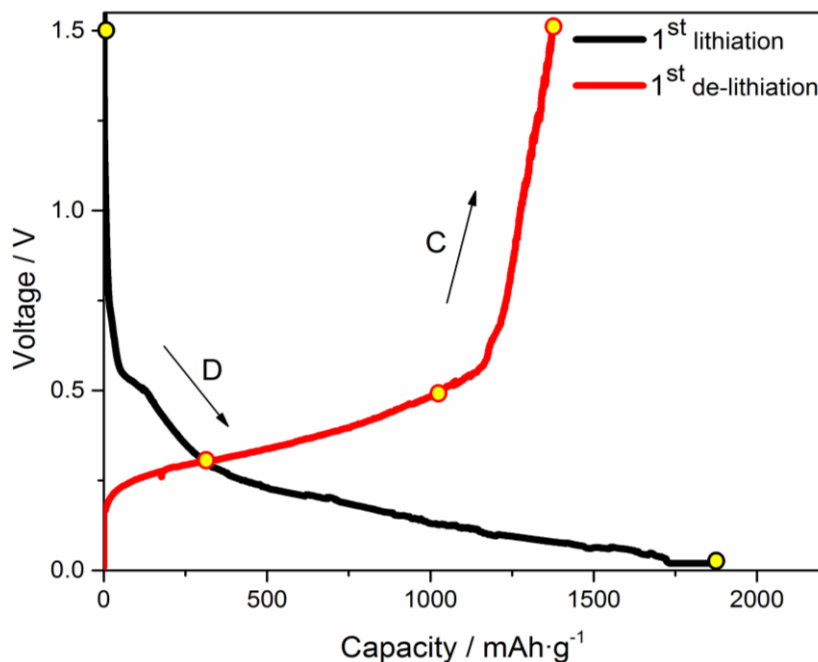


Fig. 2. Voltage vs. specific capacity profiles of NiSi₂/Si composite for the 1st discharge (D)/charge (C) cycle measured at constant current and using charge and discharge rates of 0.1C (1C = 2300 mA g⁻¹). Arrows mark progressing time, circles the states selected for XAS measurements.

The normalized XANES region at the Ni K-edge of the NiSi₂/Si composite for different states of charge is shown in Fig. 3. The absorption edge in the pristine state is characterized by a broad and smooth absorption line corresponding to the 1s → 4p transition[31], which is consistent with the metallic Ni K-edge. No clear shifts in the position of the 1s → 4p peak can be observed during lithiation or de-lithiation.

Fig. 4a displays k^3 -weighted $\chi(k)$ signals at the Ni K-edge of the material in the different states of charge. As the cell is fully discharged to 0.02 V, the corresponding $\chi(k)$ signal is not only suppressed but also noisier than other signals at high k . However, it is restored to that of the pristine state after being charged up to 0.5 V. No significant changes can be observed as the cell is charged from 0.5 V to 1.5 V. In the corresponding Fourier transforms in Fig. 4b, the amplitude of the 1st peak corresponding to the 1st shell of silicon atoms around Ni (i.e. Ni-Si) in the NiSi₂ phase varies systematically. It decreases during discharge, but begins to increase upon subsequent charging to 0.3 V and 0.5 V, and approximates the magnitude of the pristine state at 1.5 V.

3.1 Porous NiSi₂/Si composite

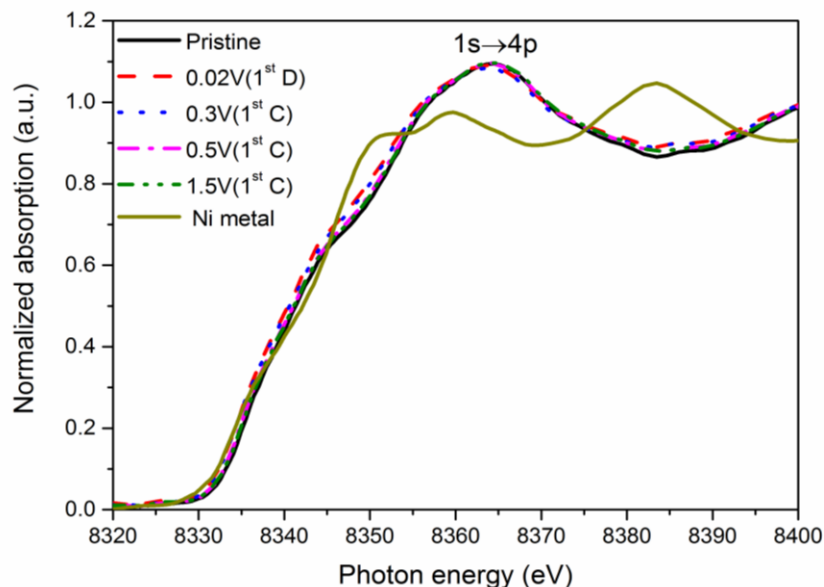


Fig. 3. Normalized absorption spectra at the Ni K-edge of a NiSi₂/Si composite during discharge and charge.

Notation: D stands for discharge and C stands for charge.

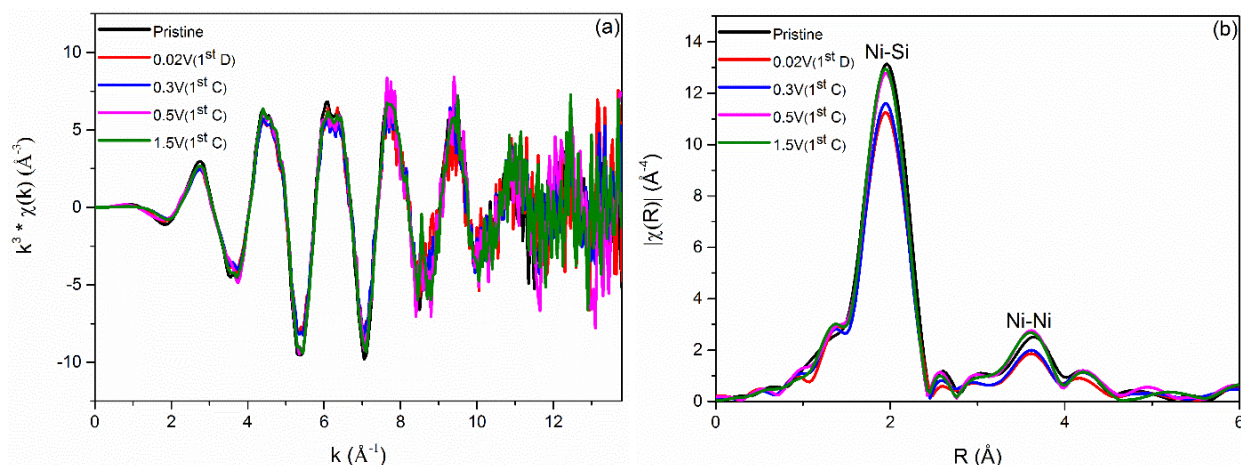


Fig. 4. (a) k^3 -weighted EXAFS signals $\chi(k)$ at the Ni K-edge and (b) their Fourier transforms of a NiSi₂/Si composite in various states of charge. Notation: Ni-Si corresponds to silicon atoms in the 1st shell around Ni absorbers and Ni-Ni corresponds to Ni atoms in the 2nd shell around Ni absorbers in Fig. 4(b).

All the data measured at the Ni K-edge fit well to the cubic fluorite structure of NiSi₂ (space group $Fm\bar{3}m$). Good agreement between the data and theory is observed for all samples indicated by R-factors lower than 0.02. The fits are shown in Fig. 5 for all the 5 stages investigated. The fit parameters for each EXAFS data are reported in Tables S1-S6 in the SI. Theoretically, the amplitude of the EXAFS signal for each coordination shell in the structure primarily depends on the product of $S_0^2 \times N$, where S_0^2 is the amplitude reduction factor and N is the number of

3.1 Porous NiSi₂/Si composite

coordinating atoms in the corresponding shell [21]. Therefore, these two parameters for any shell cannot be refined simultaneously in a fit. This can easily be justified from the fit to the EXAFS data of the pristine sample. When the number of nearest neighbors (N_{Ni-Si}) for the 1st Ni-Si shell in a fit to the EXAFS data at the Ni K-edge was constrained to 8 as obtained from the theoretical model, the fit refined S_o^2 to 0.72(4) which is consistent for Ni absorbers. When S_o^2 was constrained to 0.73, the fit refined N_{Ni-Si} to 7.9(5) which is also in accordance with the coordination of Si in the NiSi₂ component.

Moreover, concerning the effect of disorder on the EXAFS amplitudes, the terms $S_o^2 \times N$ and σ^2 (σ^2 represents statistic and thermal disorder) for a given shell are highly correlated in a fit. Since S_o^2 is a property of the absorbing atom, it accounts for amplitude suppression independent of k and R [32], and is transferable between compounds with the same absorbing atom–ligand combination, whereas N and σ^2 for any shell can be refined in one fit. Thus, S_o^2 can be constrained to the value obtained for the pristine state.

Fig. 6(a) shows the variation in the number of silicon nearest neighbors (N_{Ni-Si}) around the central Ni atoms in the NiSi₂ component of NiSi₂/Si composite during discharge and charge. N_{Ni-Si} for the sample discharged to 0.02 V decreases to 7.2(5), and then stays at 6.9(5) when the cell is charged to 0.3 V. However, upon subsequently charging the cell to 0.5 V and 1.5 V, N_{Ni-Si} increases again. Fig. 6(b) illustrates the variation in the σ^2 parameter of the 1st Ni-Si coordination shell around Ni atoms of the NiSi₂/Si composite. σ^2 is the term which accounts for the disorder of atoms and represents the distribution of the backscattering atoms around their mean position. Since all samples in this paper were prepared and measured at room temperature, the variation of σ^2 in different states can be attributed to fluctuating structural disorder during cycling. It is clear from Fig. 6(b) that the discharged sample has the highest disorder, while the other samples have nearly the same lower disorder.

Unfortunately, the error bars for the refined sigma squares σ^2 are of similar magnitude to the degree of variation. There are two reasons for that. Firstly, since the changes of the NiSi₂ phase during lithiation and de-lithiation process are quite small as can be observed in Fig. 4(a) and (b), the refined value of sigma square which stands for the disorder in the structure is small. Secondly, the sigma square is highly correlated to the number of silicon nearest neighbors (N_{ni-si}), and are refined simultaneously in a fit. Therefore, uncertainties in the refined value of N_{ni-si} will

3.1 Porous NiSi₂/Si composite

affect the uncertainties of the refined sigma square. Although the size of error bars for the refined sigma squares are big, the trend of the changes can still be observed in Fig. 6(b).

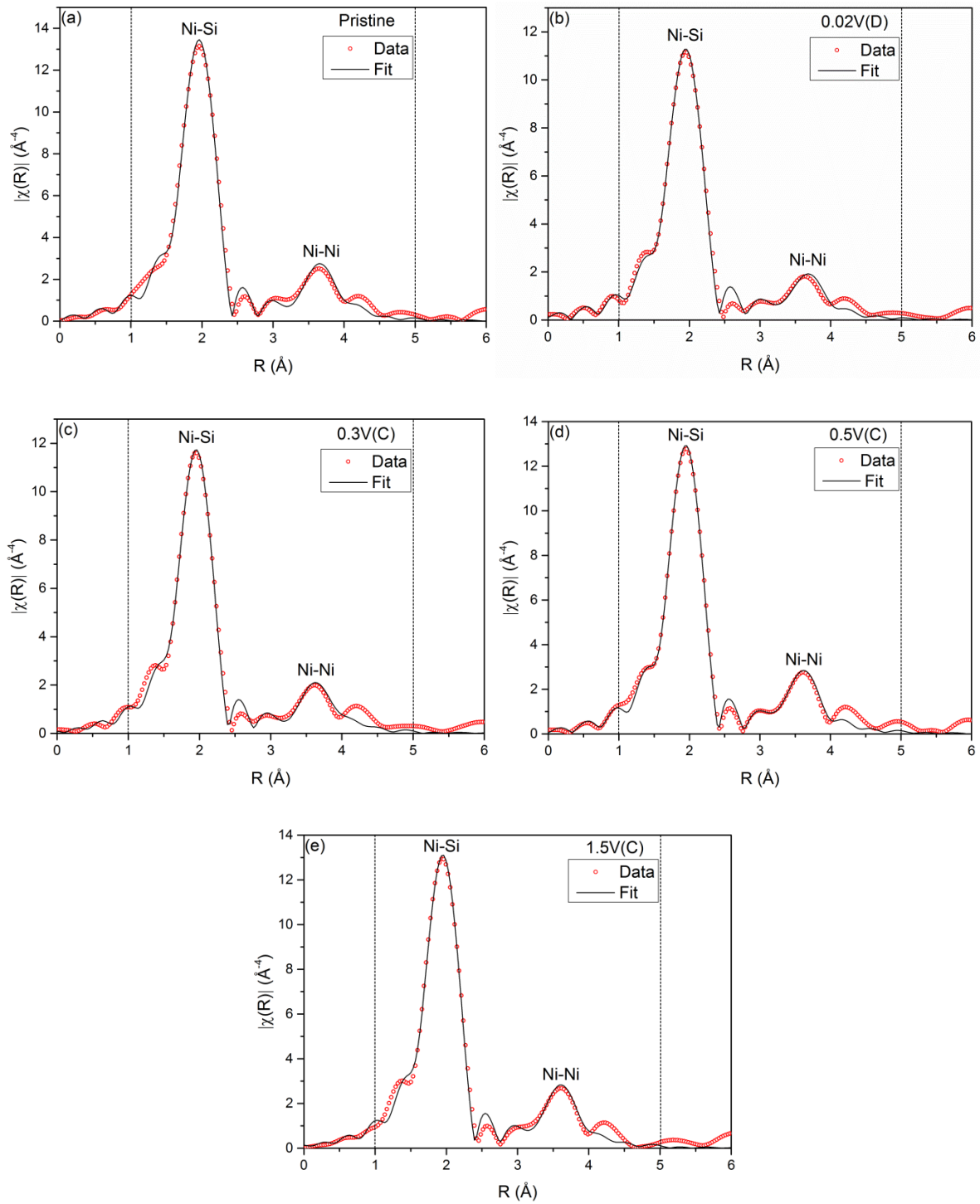


Fig. 5. EXAFS fits to the data measured at the Ni K-edge of NiSi₂/Si composite in various states of discharge and charge. Dotted lines indicate the fitting range. Notation: D stands for discharge and C stands for charge respectively.

3.1 Porous NiSi₂/Si composite

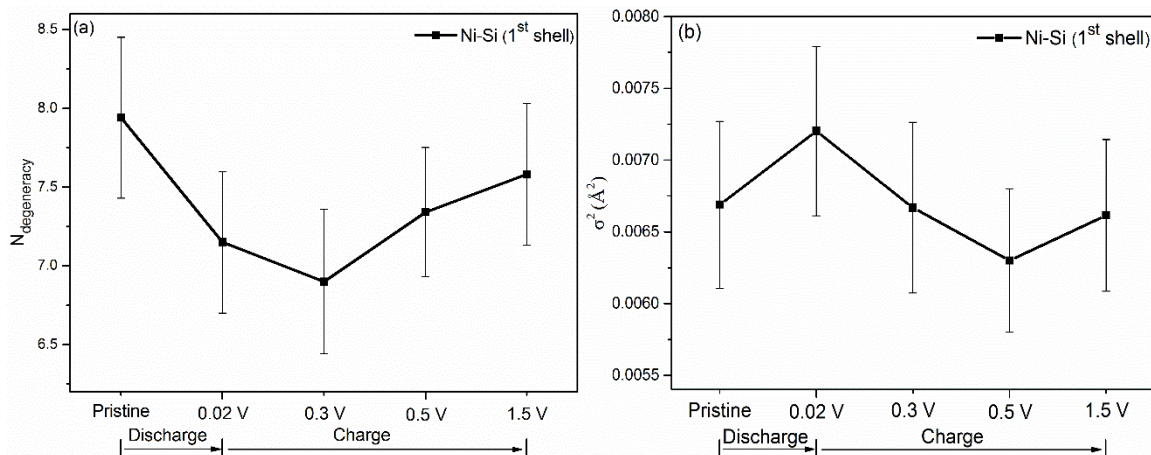


Fig. 6. (a) Number of silicon nearest neighbors (N_{Ni-Si}) for the 1st shell of NiSi₂/Si composite during discharge and charge obtained by constraining S_0^2 to 0.73. (b) Comparison of structural disorder around central Ni atoms of NiSi₂/Si composite in the pristine, discharged and differently charged states.

4. Discussion

It is well known that changes in the average valence state of an absorbing atom can be estimated by comparing the position shift of edge features, also called chemical shift. If the valence state of an absorbing atom increases, all the features of the edge should in principle also systematically shift to higher energy and vice versa. However, this approach has proved to be subjective because apart from valence, chemical shifts are affected by many other factors, such as type, symmetry and number of nearest neighbors, nature of bond etc. [31]. In addition, the relative contribution of each factor to an observed chemical shifts differs widely between different systems. This can be realized by comparing the XANES region at the Ni K-edge of the Ni reference foil and NiSi₂/Si composite in various states. Compare to the metal nickel reference foil, the 1s → 4p peak shifts to higher energy for all NiSi₂ samples at the Ni K-edge in XANES. Meanwhile all the main absorption peaks of NiSi₂ samples broaden. These chemical shifts demonstrate that the existence of the Si atom has a strong effect on the electron distribution around the Ni atom in NiSi₂. However NiSi₂ phase still shows a typical metal-metal bond character. No chemical shift can be observed in the composite during discharge and charge, which implies that the valence state of the NiSi₂ phase is invariant during cycling.

The fits to the EXAFS data at the Ni K-edge for all samples in various states of discharge and charge are in good agreement with XRD results. This suggests that the crystal structure of NiSi₂

3.1 Porous NiSi₂/Si composite

does not change during the 1st cycle. As shown in Fig. 6(a), a reduction of the refined number of nearest neighbors (N_{Ni-Si}) for the 1st Ni-Si shell around absorbing Ni atoms during discharge can be seen, which points to an increasing amount of silicon vacancies with increasing amount of inserted lithium. With continuous charging, the N_{Ni-Si} increases gradually and seems to recover to the value of the pristine state. The same trend has also been observed by Jia et al.[18]. They found that during *in situ* XRD measurement, the intensity of the NiSi₂ phase peak decreases with ongoing lithiation, but the peak did not vanish when the lithiation process ended. During the charge process, the peak intensity of the NiSi₂ phase increases gradually. These results imply that NiSi₂ react with lithium ions partly during discharge and charge.

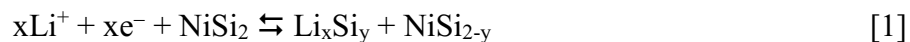
Generally, for the metal silicide $MeSi$ phase, e.g., FeSi[33] and NiSi[34], the metal element Me is assumed to be inactive with respect to lithiation, but the Si component can react with lithium to form different kinds of Li_xSi_y alloys during first lithiation. After this, the metal atom can relieve stress and volume changes caused by the formation of Li_xSi_y phases during subsequent cycling. However, no signal from metallic Ni can be seen neither during discharge nor charge of the cell, which indicates that no metallic Ni forms during discharge. At the beginning of lithium insertion into the porous NiSi₂/Si composite, lithium firstly reacts with silicon. The NiSi₂ phase serves as a buffer to relieve the stress and drastic volume changes caused by the alloying reaction. As soon as all the free silicon is consumed, lithium ions start to react with NiSi₂ and generate a large amount of silicon vacancies which is associated to the decrease of the number of nearest neighbors around an absorbing Ni atom. After this, a non-stoichiometric compound NiSi_{2-y} and amorphous Li_xSi_y form towards the end of discharge, which is consistent with the result reported by Wen et al.[35] for pure NiSi₂ anode materials based on XRD and XPS measurements. Although the crystal structure of the NiSi_{2-y} compound is the same as NiSi₂, the refined σ^2 value implies that a big structural disorder exists in the non-stoichiometric compound. As the cell is charged back to 1.5 V, the concentration of Si vacancies gradually decreases since lithium ions are extracted from the Li_xSi_y and Li_zSi phases and go back to the original structure.

Overall, the XANES and refined EXAFS results show that the NiSi₂ phase in the composite is partially reversible active to Li⁺. However, it is difficult to determine the exact amount of capacity for NiSi₂ phase during lithiation/ de-lithiation process. Cyclic voltammetry for the NiSi₂/Si composite, as demonstrated in a previous publication[18], shows the property of the pure silicon electrode, and no specific peak corresponding to the NiSi₂ phase is observed. Therefore, it

3.1 Porous NiSi₂/Si composite

is assumed that the capacity contribution of NiSi₂ phase is negligibly small, and its main role is to act as a buffer matrix to accommodate the volume changes during the lithiation/de-lithiation process.

The possible reaction mechanism of the NiSi₂/Si composite during lithiation and de-lithiation is proposed as:



and



for the NiSi₂ and for the Si component, respectively.

5. Conclusions

X-ray absorption spectroscopy experiments were performed on porous NiSi₂/Si composite electrodes in various states of charge during the 1st lithiation and de-lithiation steps. A possible reaction mechanism of NiSi₂/Si composite is proposed by taking into account both the electrochemical characterization, XRD data, XANES and refined parameters from fits of EXAFS data. When the porous NiSi₂/Si composite is used as an anode for lithium-ion batteries, the reversible capacity mainly comes from the lithiation and de-lithiation reactions of lithium with silicon. Only a small amount of NiSi₂ can react reversibly with lithium and form the non-stoichiometric compound NiSi_{2-y} and amorphous Li_xSi_y. The main role of NiSi₂ is to act as a buffer matrix to accommodate the volume changes arising from alloying during cycling.

Acknowledgements

We thank Dr. Stefan Zander, the beamline scientist of KMC-2 in the BESSY-II synchrotron light source, Berlin, Germany, for his valuable assistance. This work is sponsored by the Helmholtz Association and the China Scholarship Council.

Reference

- [1] B.A. Boukamp, G.C. Lesh, R.A. Huggins, *Journal of The Electrochemical Society*, 128 (1981) 725-729.
- [2] M. Winter, J.O. Besenhard, M.E. Spahr, P. Novák, *Advanced Materials*, 10 (1998) 725-763.
- [3] S. Hossain, Y.-K. Kim, Y. Saleh, R. Loutfy, *Journal of Power Sources*, 114 (2003) 264-276.
- [4] M.N. Obrovac, L. Christensen, *Electrochemical and Solid-State Letters*, 7 (2004) A93-A96.
- [5] J.O. Besenhard, J. Yang, M. Winter, *Journal of Power Sources*, 68 (1997) 87-90.
- [6] J.O.B. M. Winter, J. H. Albering, J. Yang and M. Wachtler, *Progress in Batteries & Battery Materials*, 1998 (1998) 208-213.
- [7] L.-F. Cui, Y. Yang, C.-M. Hsu, Y. Cui, *Nano Letters*, 9 (2009) 3370-3374.
- [8] W.-S. Kim, Y. Hwa, J.-H. Shin, M. Yang, H.-J. Sohn, S.-H. Hong, *Nanoscale*, 6 (2014) 4297-4302.
- [9] M.-H. Park, M.G. Kim, J. Joo, K. Kim, J. Kim, S. Ahn, Y. Cui, J. Cho, *Nano Letters*, 9 (2009) 3844-3847.
- [10] H. Ma, F. Cheng, J.Y. Chen, J.Z. Zhao, C.S. Li, Z.L. Tao, J. Liang, *Advanced Materials*, 19 (2007) 4067-4070.
- [11] H. Kim, B. Han, J. Choo, J. Cho, *Angewandte Chemie International Edition*, 47 (2008) 10151-10154.
- [12] Y. Yu, L. Gu, C. Zhu, S. Tsukimoto, P.A. van Aken, J. Maier, *Advanced Materials*, 22 (2010) 2247-2250.
- [13] H. Jia, P. Gao, J. Yang, J. Wang, Y. Nuli, Z. Yang, *Advanced Energy Materials*, 1 (2011) 1036-1039.
- [14] H.-Y. Lee, Y.-L. Kim, M.-K. Hong, S.-M. Lee, *Journal of Power Sources*, 141 (2005) 159-162.
- [15] W.-R. Liu, N.-L. Wu, D.-T. Shieh, H.-C. Wu, M.-H. Yang, C. Korepp, J.O. Besenhard, M. Winter, *Journal of The Electrochemical Society*, 154 (2007) A97-A102.
- [16] S. Zhou, X. Liu, D. Wang, *Nano Letters*, 10 (2010) 860-863.
- [17] K. Kang, K. Song, H. Heo, S. Yoo, G.-S. Kim, G. Lee, Y.-M. Kang, M.-H. Jo, *Chemical Science*, 2 (2011) 1090-1093.

3.1 Porous NiSi₂/Si composite

- [18] H. Jia, C. Stock, R. Kloepsch, X. He, J.P. Badillo, O. Fromm, B. Vortmann, M. Winter, T. Placke, *ACS Applied Materials & Interfaces*, 7 (2015) 1508-1515.
- [19] T. Okumura, T. Fukutsuka, A. Yanagihara, Y. Orikasa, H. Arai, Z. Ogumi, Y. Uchimoto, *Chemistry of Materials*, 23 (2011) 3636-3644.
- [20] J. Rana, S. Glatthaar, H. Gesswein, N. Sharma, J.R. Binder, R. Chernikov, G. Schumacher, J. Banhart, *Journal of Power Sources*, 255 (2014) 439-449.
- [21] J. Rana, M. Stan, R. Kloepsch, J. Li, G. Schumacher, E. Welter, I. Zizak, J. Banhart, M. Winter, *Advanced Energy Materials*, 4 (2014) 1-10.
- [22] T.A. Pascal, C.D. Pemmaraju, D. Prendergast, *Physical Chemistry Chemical Physics*, 17 (2015) 7743-7753.
- [23] K.H. Wujcik, T.A. Pascal, C.D. Pemmaraju, D. Devaux, W.C. Stolte, N.P. Balsara, D. Prendergast, *Advanced Energy Materials*, 5 (2015) 1-10.
- [24] B.K. Teo, *EXAFS: Basic Principles and Data Analysis*, Springer, Berlin, 1986.
- [25] S.D. Kelly, K.M. Kemner, J.B. Fein, D.A. Fowle, M.I. Boyanov, B.A. Bunker, N. Yee, *Geochim. Cosmochim. Acta*, 66 (2002) 3855-3871.
- [26] B. Ravel, M. Newville, *Journal of Synchrotron Radiation*, 12 (2005) 537-541.
- [27] A.L. Ankudinov, B. Ravel, J.J. Rehr, S.D. Conradson, *Physical Review B*, 58 (1998) 7565-7576.
- [28] J. Rana, R. Kloepsch, J. Li, T. Scherb, G. Schumacher, M. Winter, J. Banhart, *Journal of Materials Chemistry A*, 2 (2014) 9099-9110.
- [29] T. Kim, S. Park, S.M. Oh, *Electrochemistry Communications*, 8 (2006) 1461-1467.
- [30] F.F. Zhao, J.Z. Zheng, Z.X. Shen, T. Osipowicz, W.Z. Gao, L.H. Chan, *Microelectronic Engineering*, 71 (2004) 104-111.
- [31] J. Wong, F.W. Lytle, R.P. Messmer, D.H. Maylotte, *Physical Review B*, 30 (1984) 5596-5610.
- [32] H.J. Krappe, H.H. Rossner, *Physical Review B*, 66 (2002) 184303.
- [33] G.X. Wang, L. Sun, D.H. Bradhurst, S. Zhong, S.X. Dou, H.K. Liu, *Journal of Power Sources*, 88 (2000) 278-281.

3.1 Porous NiSi₂/Si composite

[34] G.X. Wang, L. Sun, D.H. Bradhurst, S. Zhong, S.X. Dou, H.K. Liu, *Journal of Alloys and Compounds*, 306 (2000) 249-252.

[35] Z. Wen, S. Ji, J. Sun, F. Tian, R. Tian, J. Xie, *Rare Metals*, 25 (2006) 77-81.

3.1.1 Supporting information

Table S.1: Ni EXAFS fit parameters for NiSi₂/Si composite anode in the pristine state (S_o^2 free).

$S_o^2 = 0.72(4)$ $\Delta E_o = 6.0(8)$						
Path	N_{deg}	$R_{theory}(\text{\AA})$	$\alpha_{fit}(\text{\AA})$	$\Delta R(\text{\AA})$	$R_{fit}(\text{\AA})$	$\sigma_{fit}^2(\text{\AA}^2)$
Ni-Si	8	2.329	0.007(2)	0.016(5)	2.345(5)	0.0066(6)
Ni-Ni	12	3.804	0.007(3)	0.027(11)	3.831(11)	0.0173(16)
Ni-Si	24	4.460	0.008(7)	0.036(31)	4.496(31)	0.0291(59)

Table S.2: Ni EXAFS fit parameters for NiSi₂/Si composite anode in the pristine state (S_o^2 set).

$S_o^2 = 0.73$ $\Delta E_o = 6.0(8)$						
Path	N_{deg}	$R_{theory}(\text{\AA})$	$\alpha_{fit}(\text{\AA})$	$\Delta R(\text{\AA})$	$R_{fit}(\text{\AA})$	$\sigma_{fit}^2(\text{\AA}^2)$
Ni-Si	7.9(5)	2.329	0.007(2)	0.016(5)	2.345(5)	0.0066(5)
Ni-Ni	12	3.804	0.007(3)	0.027(11)	3.831(11)	0.0174(15)
Ni-Si	24	4.460	0.008(7)	0.018(31)	4.496(31)	0.0292(58)

Table S.3: Ni EXAFS fit parameters for NiSi₂/Si composite sample discharged to 20 mV.

$S_o^2 = 0.73$ $\Delta E_o = 5.3(8)$						
Path	N_{deg}	$R_{theory}(\text{\AA})$	$\alpha_{fit}(\text{\AA})$	$\Delta R(\text{\AA})$	$R_{fit}(\text{\AA})$	$\sigma_{fit}^2(\text{\AA}^2)$
Ni-Si	7.1(4)	2.329	0.005(2)	0.012(4)	2.341(4)	0.0072(5)
Ni-Ni	12	3.804	0.006(4)	0.023(15)	3.827(15)	0.0173(16)
Ni-Si	24	4.460	-0.000(6)	-0.000(27)	4.460(27)	0.0291(59)

3.1 Porous NiSi₂/Si composite

Table S.4: Ni EXAFS fit parameters for NiSi₂/Si composite sample charged to 0.3 V.

$S_o^2 = 0.73$		$\Delta E_0 = 5.0(8)$				
Path	N_{degen}	$R_{theory}(\text{\AA})$	$\alpha_{fit}(\text{\AA})$	$\Delta R(\text{\AA})$	$R_{fit}(\text{\AA})$	$\sigma_{fit}^2(\text{\AA}^2)$
Ni-Si	6.9(5)	2.329	0.005(2)	0.011(5)	2.340(5)	0.0066(5)
Ni-Ni	12	3.804	0.006(3)	0.023(11)	3.827(11)	0.0196(18)
Ni-Si	24	4.460	0.001(7)	0.004(28)	4.464(28)	0.0309(61)

Table S.5: Ni EXAFS fit parameters for NiSi₂/Si composite sample charged to 0.5 V.

$S_o^2 = 0.73$		$\Delta E_0 = 5.2(7)$				
Path	N_{degen}	$R_{theory}(\text{\AA})$	$\alpha_{fit}(\text{\AA})$	$\Delta R(\text{\AA})$	$R_{fit}(\text{\AA})$	$\sigma_{fit}^2(\text{\AA}^2)$
Ni-Si	7.3(4)	2.329	0.004(2)	0.009(4)	2.338(4)	0.0063(5)
Ni-Ni	12	3.804	0.004(2)	0.015(8)	3.819(8)	0.0162(10)
Ni-Si	24	4.460	0.001(7)	0.004(28)	4.464(28)	0.0318(59)

Table S.6: Ni EXAFS fit parameters for NiSi₂/Si composite sample charged to 1.5 V.

$S_o^2 = 0.73$		$\Delta E_0 = 5.4(7)$				
Path	N_{degen}	$R_{theory}(\text{\AA})$	$\alpha_{fit}(\text{\AA})$	$\Delta R(\text{\AA})$	$R_{fit}(\text{\AA})$	$\sigma_{fit}^2(\text{\AA}^2)$
Ni-Si	7.6(4)	2.329	0.003(2)	0.006(4)	2.335(4)	0.0066(5)
Ni-Ni	12	3.804	0.004(3)	0.015(11)	3.819(11)	0.0164(12)
Ni-Si	24	4.460	0.000(7)	0.000(31)	4.460(31)	0.0315(62)

3.2 Nano-crystalline NiFe₂O₄ anode material

Investigation of Electronic and Local Structural Changes during Lithium Uptake and Release of Nano-crystalline NiFe₂O₄ by X-ray Absorption Spectroscopy

Dong Zhou*^a, Stefan Permien^b, Jatinkumar Rana^a, Markus Krenzel^b, Fu Sun^a, Gerhard Schumacher^a, Wolfgang Bensch^b, John Banhart^{a,c}

^a Helmholtz-Zentrum Berlin für Materialiens und Energie, Hahn-Meitner-Platz 1, 14109 Berlin, Germany

^b Institute of Inorganic Chemistry, University of Kiel, Max-Eyth-Straße 2, 24118 Kiel, Germany

^c Technische Universität Berlin, Materials Science and Technology, Hardenberg straÙe 36, 10623 Berlin, Germany

Abstract

Nano-crystalline NiFe₂O₄ particles were synthesized and used as active electrode material for a lithium ion battery that showed a high discharge capacity of 1534 mAh g⁻¹ and charge capacity of 1170 mAh g⁻¹ during the 1st cycle. X-ray absorption spectroscopy including XANES and EXAFS were used to investigate electronic and local structural changes of NiFe₂O₄ during the 1st lithiation and de-lithiation process. As lithium is inserted into the structure, tetrahedral site Fe³⁺ ions are reduced to Fe²⁺ and moved from tetrahedral sites to empty octahedral sites, while Ni²⁺ ions are unaffected. As a consequence, the matrix spinel structure collapses and transforms to an intermediate rock-salt monoxide phase. Meanwhile, the inserted Li is partially consumed by the formation of SEI and other side reactions during the conversion reaction. With further lithiation, the monoxide phase is reduced to highly disordered metallic Fe/Ni nanoparticles with a number of nearest neighbors of 6.0(8) and 8.1(4) for Fe and Ni, respectively. During subsequent de-lithiation, the metal particles are individually re-oxidized to Fe₂O₃ and NiO phases instead to the original NiFe₂O₄ spinel phase.

1. Introduction

As the most promising power source for smart phones, laptops, electric vehicles (EVs) and hybrid electric vehicles (HEVs), lithium ion batteries (LIBs) have attracted much attention in past

3.2 Nano-crystalline NiFe₂O₄ anode

decades. In order to meet the ever-increasing demand for high energy density, high capacity and long service life, various transition metal oxides and compounds (TMOs) have been investigated because of their theoretical capacity based on the conversion reactions that is much higher than that of the commercial lithium intercalation or lithium alloying materials[1-6]. During Li uptake, TMOs are first reduced to extremely small metallic nanoparticles dispersed in a Li₂O matrix. During the subsequent de-lithation, the metallic particles are re-oxidized. The formal reaction mechanism can be described using the following general equation[1]:



Among these TMOs, iron-based compounds are particularly interesting candidates as they are less expensive and more environmentally friendly than cobalt-containing oxides. Several papers[7-15] have been published on the exploration of iron-based compounds as a substitute for current commercial graphite anode materials, such as Fe₂O₃[7], Fe₃O₄[11], and spinel ferrite MFe₂O₄ (M =Mg, Cu, Co, Ni, Zn and Mn)[8-10, 12-17]. As a member of iron-based compounds, NiFe₂O₄ comes into notice since it displays a high theoretical capacity of 915 mAh g⁻¹[18]. However, TMO electrodes suffer from a rather fast capacity fading within few cycles because of the formation of an insulating polymeric layer around the particles and poor integrity caused by the marked volume changes upon cycling[9, 19, 20]. Various strategies have been used to improve the electrochemical behavior of NiFe₂O₄. NuLi *et al.*[7] prepared nano-crystalline NiFe₂O₄ ferrite thin films by an electrochemical route, which delivered a reversible capacity of 450–460 mAh g⁻¹ at 10 μAcm⁻² and more than 75% reversible capacity still remaining up to 100 cycles. Ding *et al.*[21] synthesized a hierarchically nanostructured NiFe₂O₄/C composite which showed a high specific capacity of 780 mAh g⁻¹ after 40 cycles. Cherian *et al.*[22] reported NiFe₂O₄ nanofibers with a reversible capacity of 1000 mAh g⁻¹ after 100 cycles.

Though the conversion reaction (1) of simple monoxides (CoO, CuO, FeO or NiO)[1] is thermodynamically favorable and has been widely investigated by ex-situ/in-situ X-ray diffraction (XRD), transmission electron microscopy (TEM), X-ray photoelectron spectroscopy (XPS) and Mössbauer spectroscopy during discharging and charging, the reaction is still not well understood due to the intriguing nature of Li₂O and ultrafine metal particles and limitations for the above mentioned analytic techniques. For example, the highly disordered metallic particles formed during discharge cannot be detected by XRD because they are presumably smaller than

3.2 Nano-crystalline NiFe₂O₄ anode

the coherence length of the corresponding X-rays[1]. Sample preparation for TEM is laborious and it is easy to introduce artifacts which affect the results. XPS is sensitive to the sample surface and cannot provide information about bulk properties. A deeper understanding of the reactions for TMOs occurring during lithiation and de-lithiation is crucially important for the search for new high-performance electrode materials. X-ray absorption spectroscopy (XAS), a unique elementary selective technique, is a very useful tool for clarifying the changes in oxidation state and local environment of each absorbing atom of TMO electrodes since it does not require long-range order, and provides a chance to get a deeper insight into individual reaction steps of the conversion reaction.

In the study presented here, we investigated electrical and local structural changes in nano-crystalline NiFe₂O₄ anode material by using X-ray absorption near edge structure (XANES) and extend X-ray absorption fine structure (EXAFS) in order to establish and elucidate a more detailed conversion reaction mechanism upon charge and discharge.

2. Experimental

2.1 Synthesis

NiFe₂O₄ nanoparticles were synthesized by mixing 5 mmol Ni(NO₃)₂·6H₂O (97 %, Merck), 10 mmol Fe(NO₃)₃·9H₂O (98 %, Riedel-de Haen), 3 mL Ethylenglycol (99 %, Merck Millipore) and 15 mmol succinic acid (99 %, Merck) in a Fritsch Pulverisette ball mill for 2 h with 15 mm agate balls at 500 rpm in air. The viscous product was decomposed at 400 °C in a pre-heated oven for 3 h.

2.2 Materials characterization and electrochemical Li insertion

XRD patterns of pristine NiFe₂O₄ were recorded on a X'PERT PRO (P-analytical) instrument equipped with a PIXcel detector using Cu K_α radiation. EDX spectra were obtained using a Philips ESEM XL 30 equipped with an EDX detector from EDAX company. TEM investigations were performed in a Tecnai F30 G²-STwin microscope operated at 300 kV with a field emission gun cathode and a Si/Li detector (EDAX). The NiFe₂O₄ nanoparticles were suspended in n-butanol and dropped on a holey-carbon copper grid for TEM. For electrochemical characterization, 70 wt% NiFe₂O₄ were mixed with 20 wt% carbon (Super C65 Timcal, Suisse)

3.2 Nano-crystalline NiFe₂O₄ anode

and 10 wt% sodium carboxy methylcellulose (Sigma-Aldrich, Germany) as a binder. The compounds were mixed with distilled water to a viscous slurry, painted on copper foil and dried over night at room temperature. Afterwards, 10 mm discs were cut each containing ~2-3.5 mg of active material. NiFe₂O₄ nanoparticles were used as the anode in a Swagelok-type test cell, using lithium metal as the cathode, glass fiber filter discs (Whatman, UK) as the separator, and a solution of 1 M LiPF₆ in an 1:1 ethylene carbonate-dimethyl carbonate mixture (BASF, Germany) as the electrolyte. Test cells were assembled in an MBraun argon-filled glove box (<1 ppm O₂, <1 ppm H₂O) and discharged with a C/10 rate (theoretical capacity 933 mAh g⁻¹). Galvanostatic charge-discharge experiments were performed with a Material Mates 510 DC until the desired formal composition or the cell potential were reached. The cells were opened under argon atmosphere and active material was scraped off the Cu foil and mixed with graphite (Sigma-Aldrich, 99.99%) in an agate mortar. For the XAS measurements, a pellet with about 18wt% electrode material and 82 wt% graphite were pressed and protected with adhesive Kapton tape. The pellets were transferred to the beam line in an air tight glass container.

Ex-situ XAS analysis at the Fe and Ni K-edge was performed in transmission mode at the KMC-2 beamline of the synchrotron BESSY at Helmholtz-Zentrum Berlin, Germany. This beamline is equipped with a graded Si-Ge (111) double -crystal monochromator. About 65% of the maximum possible intensity of the beam is transmitted through the sample during the measurement. The energy was calibrated using Ni or Fe foil. The data were processed by using the software *ATHENA* and *ARTEMIS* of the package *IFEFFIT* as reported in the literature[23, 24]. Each spectrum was energy-calibrated with respect to the first peak in their corresponding reference metal foil derivative spectrum. The normalized EXAFS signal in k space was multiplied by k^3 in order to obtain a good signal at high k values because of the damping effect and Fourier transformed in R space without phase shift correction. The model for each fitting was generated based on the known crystal structure by performing ab initio calculations using the code *FEFF8*[25]. Change in the bond length ΔR was calculated by $\Delta R = \alpha_{fit} \times R_{theory}$, where α_{fit} is the refined fractional change for each coordination shell. The Debye-Waller factor σ^2 is also given for each coordination shell depending on the mass of the backscattering atoms and their distance from the absorber. Multiple scattering paths were included but the fitting parameters were constrained to those of single scattering paths. The statistical quality of each EXAFS fit was evaluated based on its R-factor.

3. Results and Discussion

Fig. 1 shows the XRD pattern of as-synthesized NiFe₂O₄ together with the calculated diagram. The XRD pattern can be indexed with the $Fd\bar{3}m$ space group in an inverse cubic spinel structure. The lattice parameter and volume-weighted average particle size obtained by Rietveld refinement of the XRD data are $a = 8.3469(5)$ Å and $D = 12(1)$ nm, respectively.

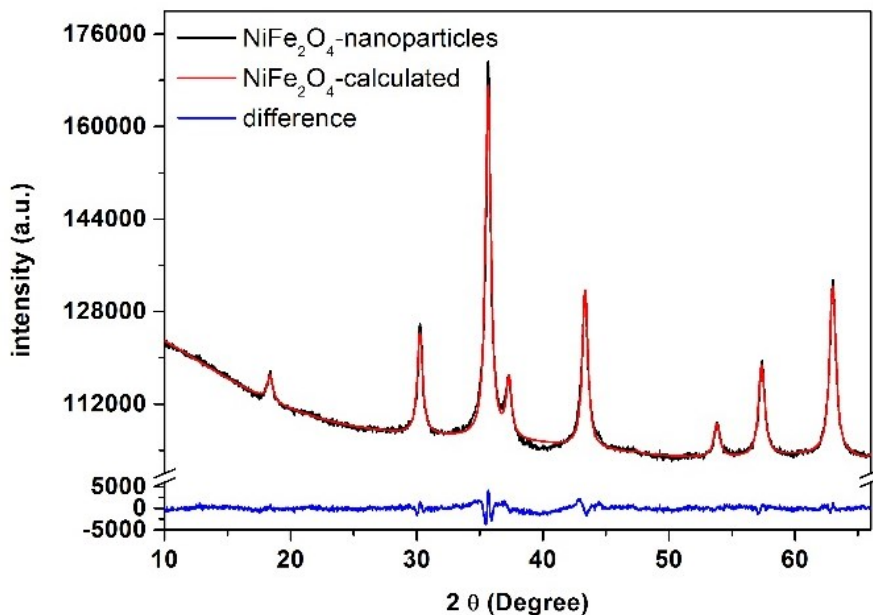


Fig. 1 XRD pattern of the prepared nano-particles. The calculated X-ray pattern of NiFe₂O₄ is shown for comparison.

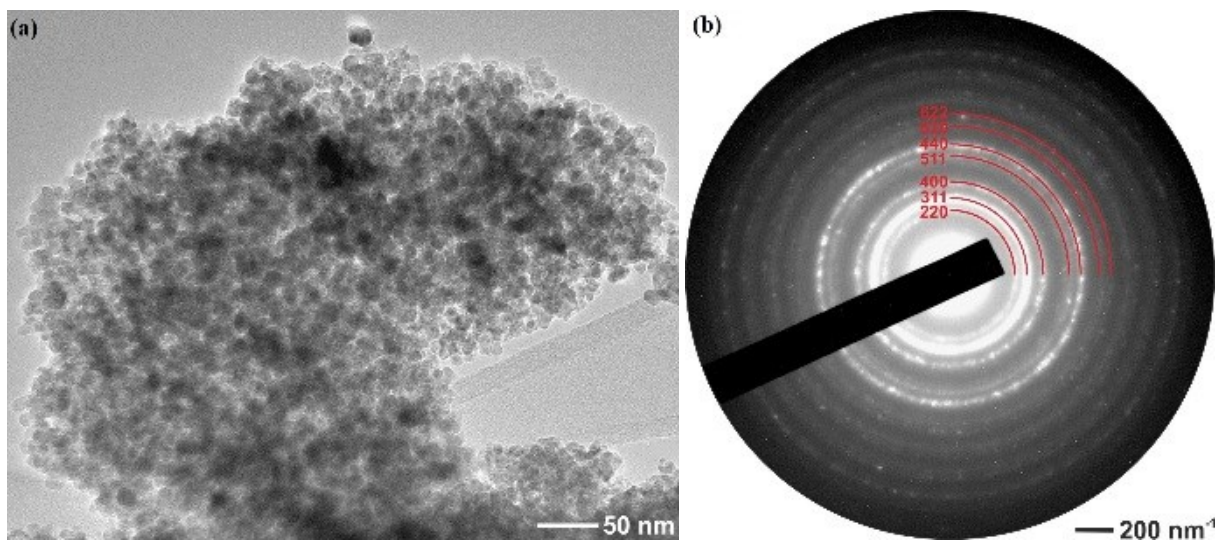


Fig. 2 (a)TEM bright-field image of a pristine NiFe₂O₄ sample; (b) corresponding SAED pattern.

3.2 Nano-crystalline NiFe₂O₄ anode

The morphology of pristine NiFe₂O₄ powder was examined by TEM, and is shown in Fig. 2(a). As can be seen, the nanoparticles agglomerate with each other showing typical sizes around 10 nm. The SAED pattern in Fig. 2(b) verifies the spinel structure of NiFe₂O₄.

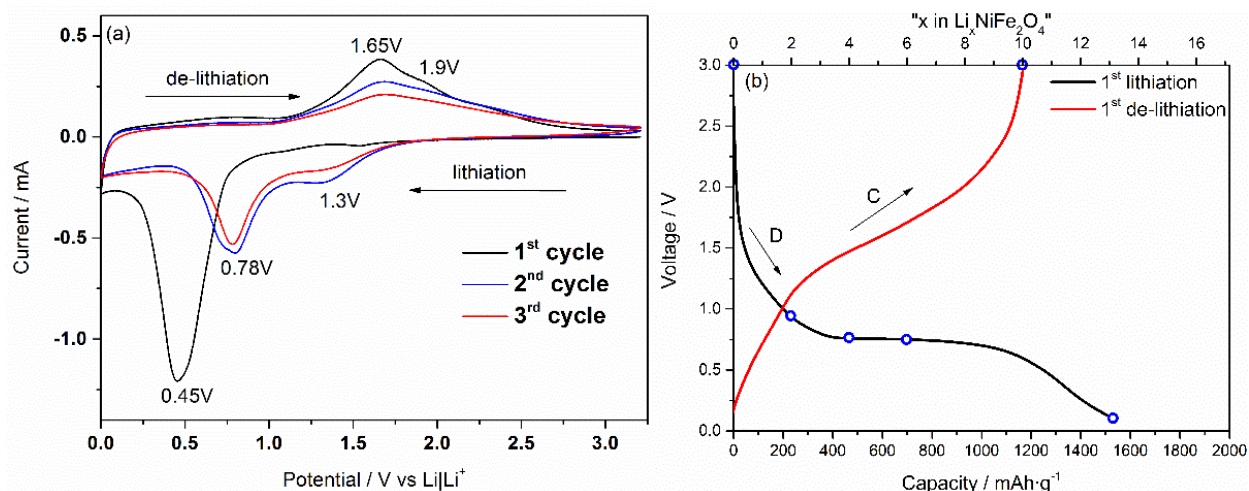


Fig. 3 (a) Cyclic voltammetry of NiFe₂O₄ anodes and (b) Voltage vs. specific capacity profiles of NiFe₂O₄ for the 1st discharge(D)/charge(C) cycle measured at constant current and using charge and discharge rates of 0.1C (1C = 933 mAh g⁻¹). Arrows mark progressing time, circles the states selected for XAS measurements.

The results of cyclic voltammetry (CV) carried out at a scan rate of 0.05 mVs⁻¹ for 3 cycles and discharge/charge voltage profiles for the 1st cycle of the NiFe₂O₄ anodes are given in Fig. 3(a) and (b), respectively. Significant differences can be observed in Fig. 3(a) between the first and subsequent cycles, which is consistent with the results reported in the literature[26]. The sharp cathodic peak at around 0.45V corresponds to the reduction of nickel and iron ions to the metallic state during the first discharge. The hardly resolved two cathodic peaks at around 1.65V and 1.9V are due to the oxidation of metallic nanoparticles during the first charge process. The initial spinel structure does not seem to be restored after the first cycle. A specific capacity of 1534 mAh g⁻¹ is attained as the cell is discharged to 0.1V, while it delivers a capacity of 1170 mAh g⁻¹ as it is charged to 3.0V. The six circles marked in blue in the voltage profiles (Fig. 3(b)) represent the six different states studied by X-ray absorption spectroscopy (including XANES and EXAFS), i.e., pristine state, 0.95V, 0.76V 0.75V and 0.1V during the 1st lithiation and 3.0V during charge after the 1st discharge, respectively.

3.1 XANES

Fig. 4(a) shows the normalized Fe K-edge XANES spectra of NiFe₂O₄ at various states of the 1st cycle. The K-edge XANES spectra of 3d transition metals are usually characterized by a threshold energy, a pre-edge and a main edge, which provide information about the oxidation state and site symmetry of the absorbing atom. In principle, a small pre-edge peak which is due to the dipole-forbidden 1s→3d transition and a main peak which is caused by the 1s → 4p transition can be observed for 3d TMOs. The weak pre-edge peak can only be observed in the presence of 3d → 4p orbital mixing or direct quadrupolar coupling. Since the outer p-orbitals are more sensitive to electronic changes, the average valence state of the absorbing atom can be estimated from the position of the main absorption edge with respect to reference materials[27]. As the valence state of the central absorbing atom decreases, all the main features shift to lower energies and vice versa. From Fig. 4(a) it can be seen that the pre-edge and main edge of the pristine NiFe₂O₄ sample are close to that of the Fe₂O₃ reference compound. Fe ions of pristine NiFe₂O₄ therefore appear to have a formal oxidation state of +3. After the uptake of 6 lithium ions into the NiFe₂O₄ electrode (0.75V, 1st D), the main edge shifts close to that of the FeO compound without a change in shape, pointing at the reduction of Fe³⁺ ions to Fe²⁺ ions. The only explanation for this would be that 4 of the 6 Li are consumed by the SEI formation and other side reactions. With further discharge to 0.1V, the energy position and shape of the main edge seem to be identical to that of the reference Fe metal, suggesting the reduction of iron ions to the metallic state. During the subsequent charge to 3.0V, the pre-edge peak shows up and the main edge shifts to higher energy, reflecting the oxidation of metallic Fe during Li release.

Unlike the Fe K-edge XANES spectra, a very weak pre-edge peak can be observed at the Ni K-edge of the pristine state (Fig. 4(b)) because of the dipole-forbidden 1s→3d transition in a centrosymmetric field, which is expected since Ni atoms have an octahedral coordination in the inverse spinel structure. The main absorption edge stays at the same energy position (around 8351eV) as NiO oxide and remains there until the cell has been discharged to 0.75V. This indicates that most Ni²⁺ ions are not reduced at this voltage because of the SEI formation and other side reactions, which is also in good agreement with the results of Fe. As the cell is further discharged down to 0.1V, similar to Fe, the absorption line becomes smooth and overlaps with that of the reference Ni metal, suggesting the reduction of Ni²⁺ ions to metallic nickel. As the cell is charged to 3.0V, the main absorption edge moves back to 8351 eV along with a steep white

3.2 Nano-crystalline NiFe₂O₄ anode

line. These changes can be interpreted by the re-oxidization of metallic Ni to Ni²⁺ ions during the charge process.

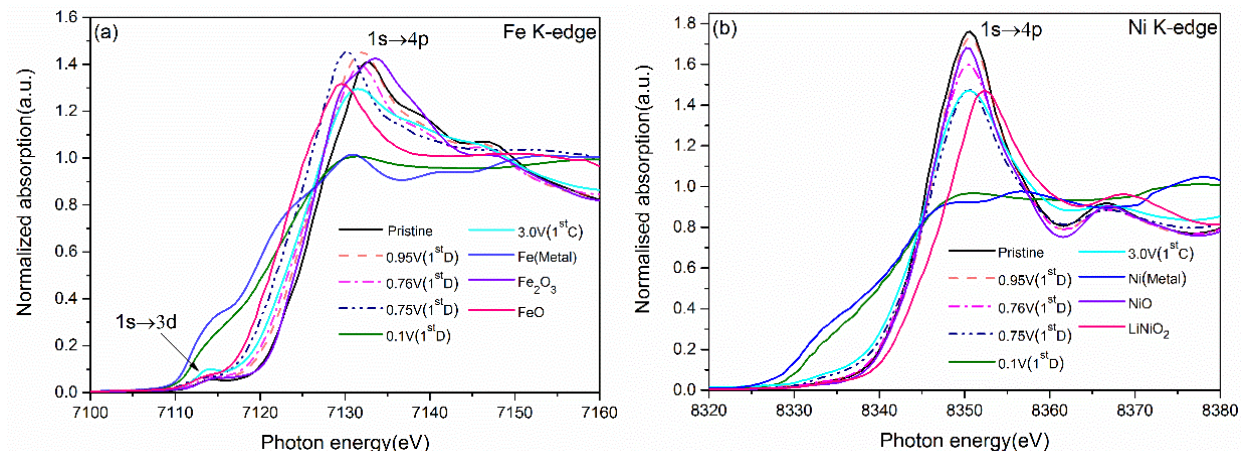


Fig. 4 Normalized absorption spectra at the (a) Fe and (b) Ni K-edge of NiFe₂O₄ in various states during 1st discharge and charge. Notations: 0.95V (1st D) means discharge of the cell to 0.95V in the first cycle, and so on. 3.0V (1st C) means charge the cell to 3.0V after the cell has been discharged to 0.1V in first cycle.

3.2 EXAFS

Fig. 5(a) represents the k^3 -weighted EXAFS $\chi(k)$ signals at the Fe K-edge of NiFe₂O₄, while their corresponding Fourier transforms are shown in Figure 5(b). As can be seen in Fig. 5(a), the $\chi(k)$ signal shifts slightly to lower k values and varies from $k \approx 9 \text{ \AA}^{-1}$ as the cell is discharged to 0.95V. Then the signal gradually fades out with increasing insertion of Li⁺. With further discharge to 0.1V, clear differences in the EXAFS spectrum can be seen compared to that of the pristine NiFe₂O₄ sample and the signal does not recover during the following charge to 3.0V. In the corresponding Fourier transforms in Fig. 5(b), the spectrum of pristine NiFe₂O₄ is in good agreement with that of the inverse spinel structure ($[\text{Fe}^{3+}]_{\text{tetra}}[\text{Ni}^{2+}\text{Fe}^{3+}]_{\text{octa}}\text{O}_4$), where the first-shell peak is due to backscattering from oxygen anions around tetrahedral Fe sites and octahedral Fe/Ni sites[28]. In contrast, the peaks at $\sim 2.8 \text{ \AA}$ and $\sim 3.2 \text{ \AA}$ are arisen from the scattering from metals around the octahedral site and both octahedral and tetrahedral sites respectively. Interestingly, as the cell is discharged to 0.95V, the intensity of Fe-TM_{tetra/octa} peak located at $\sim 3.2 \text{ \AA}$ markedly decreases. This may be caused by the movement of the reduced Fe²⁺ ions from tetrahedral to empty octahedral sites due to the strong repulsive interaction between inserted

3.2 Nano-crystalline NiFe₂O₄ anode

lithium ions and transition metal cations in the structure, which has also been observed by other groups[29, 30]. In the study of structural changes of lithiated magnetite Li_xFe₃O₄, Thackeray *et al.*[29] found that inserted lithium ions first occupy one-half of the interstitial octahedral sites (16c) and then cooperatively displace the tetrahedral site iron ions into the empty octahedral sites at 16c so that the partially ordered rock-salt type structure (LiFe)_{16c}[Fe₂]_{16d}O₄ is produced when x=1.0. They concluded that Fe₃O₄ undergoes a structural phase transition to a FeO-type rock-salt phase upon lithiation to Li₂Fe₃O₄.

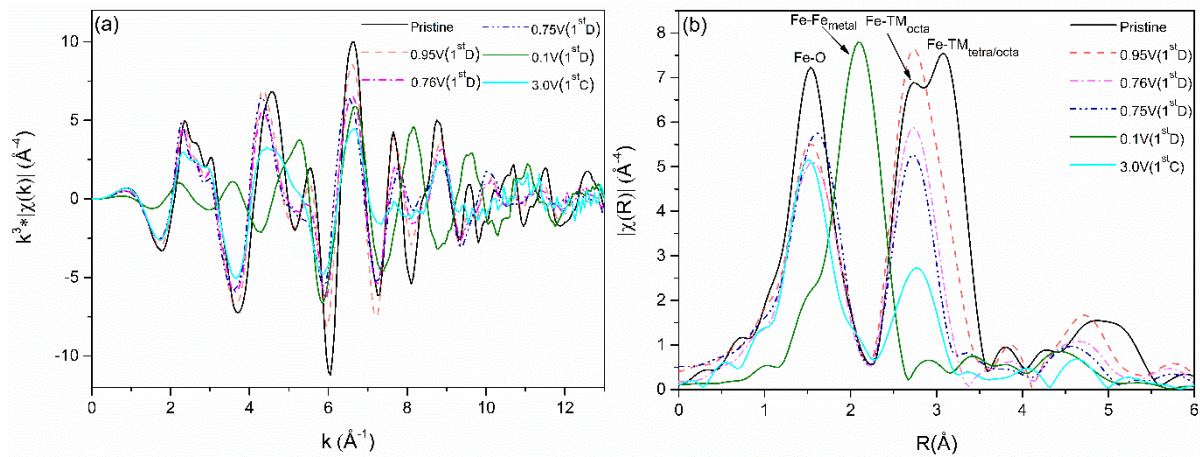


Fig. 5 (a) k^3 -weighted EXAFS $\chi(k)$ signals and, (b) their Fourier transforms at the Fe K-edge of NiFe₂O₄ in various states during discharge and charge. Notations: Fe-O corresponds to oxygen atoms in the 1st shell around Fe absorbers, Fe-TM_{octa} corresponds to Fe/Ni atoms sited on the octahedral situated in the 2nd shell around Fe absorbers, and Fe-TM_{tetra/octa} corresponds to Fe/Ni atoms sited on the octahedral situated and Fe atoms situated on the tetrahedral site in the 3rd shell around Fe absorbers in the inverse spinel structure. Fe-Fe_{metal} corresponds to Fe atoms in the 1st shell around Fe absorbers in metallic iron. Discrete data points are presented by lines for the sake of clarity.

Upon further discharge to 0.75V, no new peak can be observed in Fig. 5(b). Combining the results from EXAFS and XANES measurements, it seems that the phase transition from spinel to rock-salt monoxide is still underway at this state (0.75V, 1stD). Possibly, the inserted lithium ions are partially consumed by the formation of solid electrolyte interface (SEI) around electrode particles instead of reacting with the active electrode material itself, which has been observed in CoO anode materials[31]. As the cell is discharged to 0.1V, only one intense Fe-Fe_{metal} peak ($\sim 2.2\text{\AA}$) can be seen, which is consistent with that of the calculated Fe K-edge EXAFS spectrum of highly disordered Fe nanocrystal (size $\sim 3\text{nm}$) reported by Sobczak *et al.*[32]. The loss of long-

3.2 Nano-crystalline NiFe₂O₄ anode

range order of the newly formed metallic iron nanoparticles suggests the existence of pronounced disorder in the structure. During subsequent charge up to 3.0V, the Fe-Fe_{metal} peak is replaced by the Fe-O peak, manifesting the oxidation of metallic iron during de-lithiation. Guo *et al.*[9] pointed out that in the ZnFe₂O₄ electrode, Fe and Li-Zn alloy were formed as the cell was deeply discharged and Fe₂O₃ was formed after recharging the battery. This was derived from HRTEM and first-principle calculations.

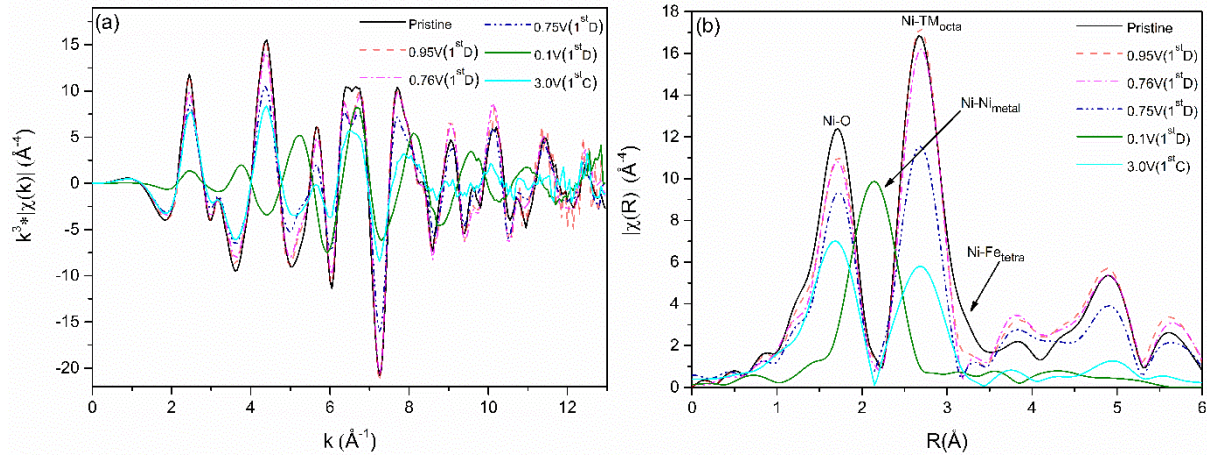


Fig. 6 (a) k^3 -weighted EXAFS $\chi(k)$ signals and, (b) their Fourier transforms at the Ni K-edge of NiFe₂O₄ in various states during discharge and charge. Notations: Ni-O corresponds to oxygen atoms in the 1st shell around Ni absorbers, Ni-TM_{octa} corresponds to Fe/Ni atoms situated on the octahedral site in the 2nd shell around Ni absorbers, and Ni-Fe_{tetra} corresponds to Fe atoms situated on the tetrahedral site in the 3rd shell around Ni absorbers in the inverse spinel structure. Ni-Ni_{metal} corresponds to Ni atoms in the 1st shell around Ni absorbers in metallic nickel. Discrete data points are represented by lines for the sake of clarity.

Fig. 6(a) shows the k^3 -weighted EXAFS $\chi(k)$ signals at the Ni K-edge of NiFe₂O₄. Similar to Fe, the signals in k space are increasingly damped as the cell is discharged from the pristine state to 0.75V. With further discharge to 0.1V and the following charge to 3.0V, the intensity and shape of the $\chi(k)$ signals vary markedly compared to the pristine sample. More pronounced changes can be observed in their corresponding Fourier transforms in Fig. 6(b). At the beginning of lithiation, the small Ni-Fe_{tetra} shoulder which corresponds to the contribution of Fe atoms on tetrahedral sites, first disappear, followed by a systematic reduction of the amplitude of all peaks during further discharge to 0.75V. At the end of discharge, only one single Ni-Ni_{metal} peak located at $\sim 2.1\text{\AA}$ can be observed, suggesting the formation of metallic nickel nanoparticles. Upon subsequent charge to 3.0V, the Ni-Ni_{metal} peak vanishes and the Ni-O peak reappears. Therefore,

3.2 Nano-crystalline NiFe₂O₄ anode

it can be concluded that the newly formed metallic nickel is oxidized during the release of lithium ions in the charge process.

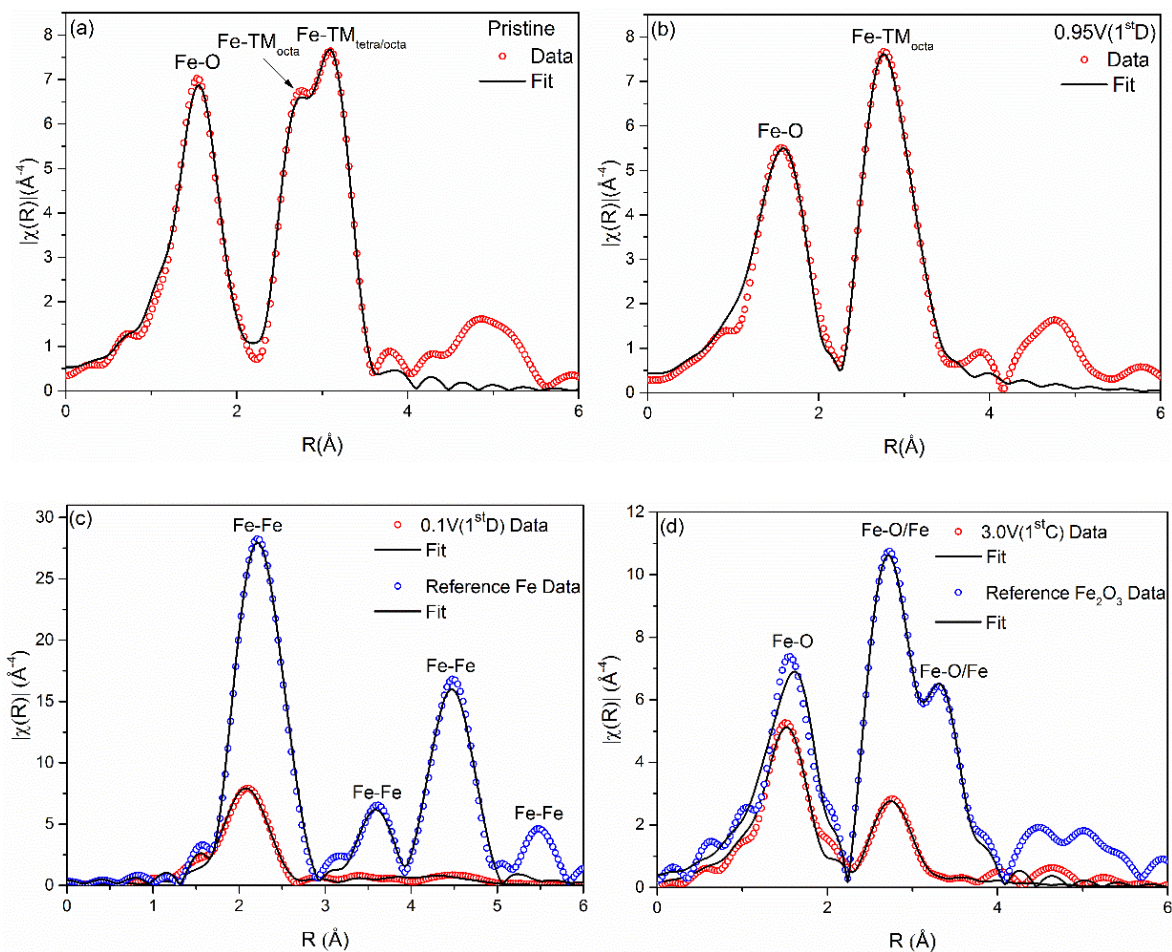


Fig. 7 EXAFS fits to the data measured at the Fe K-edge of NiFe₂O₄ in various states during charge and discharge compared to reference compounds.

In order to get more quantitative information about structural changes during lithiation and delithiation process, the EXAFS data of the most important samples were fitted at various states including few reference materials. Since Fe and Ni are close to each other in the periodic table of the elements and, therefore, have similar backscattering amplitudes, only Fe backscatters are considered at Fe K-edge, and only Ni backscatters are considered at Ni K-edge. The fits are shown in Fig. 7 for the Fe K-edge and in Fig. 8 for the Ni K-edge respectively. The fit parameters for each EXAFS data set are listed in Table S1-S12 in the SI. The data is in good agreement with the model for all states as all the R-factors of the fits are less than 0.02.

The EXAFS data at both the Fe and Ni K-edge of the pristine sample is fitted well up to $\sim 4\text{\AA}$

3.2 Nano-crystalline NiFe₂O₄ anode

a totally inverted spinel structure[33] ($[\text{Fe}^{3+}]_{\text{tetra}}[\text{Ni}^{2+}\text{Fe}^{3+}]_{\text{octa}}\text{O}_4$), where Ni^{2+} ions occupy octahedral sites and Fe^{3+} ions are equally distributed between tetrahedral and octahedral sites. As the cell is discharged to 0.95 V corresponding to 2 lithium ions inserted per formula unit, all the Fe^{3+} ions should be reduced to Fe^{2+} ions and form a rock-salt structure monoxide according to the charge compensation mechanism without consideration of the SEI formation in the electrode. However, in the NiFe_2O_4 electrode, Fe shows a mixed valence state between +2 and +3 at this voltage, which evidences the consumption of lithium ions due to SEI formation. An intermediate model structure $[\text{Ni}^{2+}\text{Fe}^{3+}]_{\text{octa}}[\text{LiFe}^{2+}]_{\text{octa}}\text{O}_4$ is proposed to fit the data collected at 0.95V because of the movement of tetrahedral site Fe cations during lithiation. The data is fitted well with the proposed model structure.

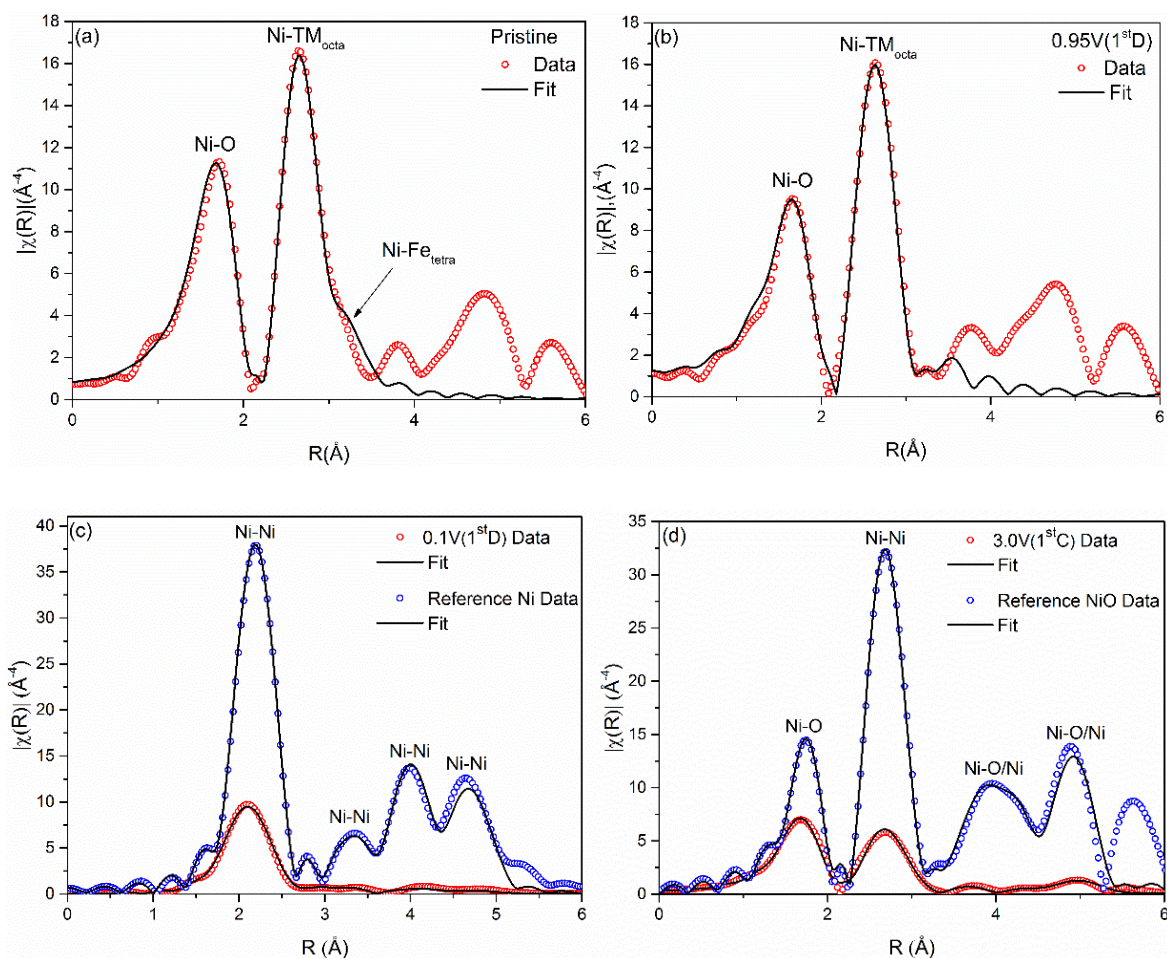


Fig. 8 EXAFS fits to the data measured at the Ni K-edge of NiFe_2O_4 in various states during charge and discharge and relative reference compounds.

Table. 1 illustrates the refined average bond length of the 1st and 2nd coordination shells around

3.2 Nano-crystalline NiFe₂O₄ anode

Fe and Ni cations as derived from the fits. A clear increase can be observed around Fe cations in two coordination shells, which is caused by the reduction of Fe³⁺ to Fe²⁺ and migration of Fe²⁺ ions. On the contrary, the refined bond length R_{mean} for both Ni-O and Ni-TM shells around Ni cations are almost constant, suggesting that Ni ions are nearly unaffected as the cell is discharged to 0.95V. Unfortunately, with further discharge to 0.75V, the EXAFS data cannot be fitted at both the Fe and Ni K-edges because of the complexity of the conversion reactions that have taken place in the electrode. The XAS signal at this voltage may represent a mixture of several metastable phases. Therefore, it is hard to find out the proper fraction for each structure in the mixture of phases to fit the data.

Table 1. Refined average bond length of 1st and 2nd coordination shells around Fe and Ni atoms of NiFe₂O₄ in the pristine state and after discharge to 0.95V.

Sample name	Fe-O (1 st shell)	Fe-TM (2 nd shell)	Ni-O (1 st shell)	Ni-TM (2 nd shell)
Pristine	1.915(8)	2.866(8)	1.930(6)	2.887(4)
0.95V(1 st D)	1.982(8)	2.956(9)	1.919(10)	2.883(5)

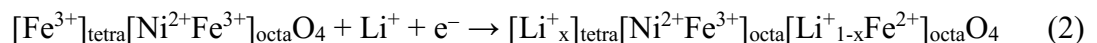
For transition metal oxides in the spinel structure, it is widely accepted that nano-sized metallic products form as the cell is discharged and then re-oxidized during subsequent charge[1]. In NiFe₂O₄, the fitting results are in good agreement with the formation of nano-sized metallic clusters. We find that the spinel NiFe₂O₄ is reduced to metallic iron and nickel as the cell is deeply discharged and then re-oxidized to Fe₂O₃ and NiO during the following charge. However, there is one important observation: Compared with the reference materials, the amplitude of each peak is reduced in R space for the newly formed metallic nanoparticles and their corresponding oxides as shown in Fig. 7(c, d) and Fig. 8(c, d), respectively. The amplitude of the EXAFS signal for each coordination shell in the structure is mainly affected by two factors: (1) the product of $S_o^2 \times N$, where S_o^2 is the amplitude reduction factor and N is the number of coordinating atoms in that shell; (2) The Debye-Waller factor σ^2 which represents static and thermal disorder for a given shell. Therefore, it is crucial not to vary S_o^2 and N for any shell simultaneously in one fit. Since S_o^2 is transferable between compounds with the same absorbing atom–ligand combination, it can

3.2 Nano-crystalline NiFe₂O₄ anode

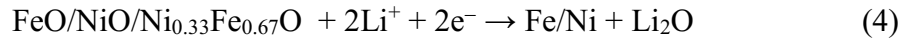
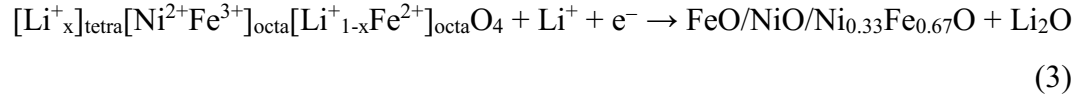
be constrained to the value obtained from reference compounds. Thus, N and σ^2 can be refined for each shell.

According to the refined number of nearest neighbors of absorbing Fe and Ni atoms for the 1st coordination shell as the cell is discharged to 0.1V, the coordination number for metallic Fe is reduced to 6.0(8) (for bcc α -iron this should be 8) and for metallic Ni to 8.1(4) (for fcc nickel this should be 12). The reduced coordination number N suggests that the metal particles formed during the discharge process are quite small since N can play a significant role in the signal amplitude suppression only when the particle size is smaller than 5 nm according to a calculation based on the crystallite size and crystallite structure[34]. Similar results are also reported for NiCo₂O₄ anode materials[35]. As the NiCo₂O₄ electrode is fully discharged to 0V, it gives a coordination number N~5 for Co and N~4 for Ni, respectively, without concerning the effect of disorder to the signal[35]. In principal, the Debye-Waller factor σ^2 will increase as the particle size decreases in nano-crystalline materials because of surface effects. At the surface, the coordination number is reduced compared to the bulk.

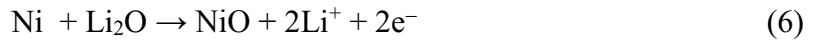
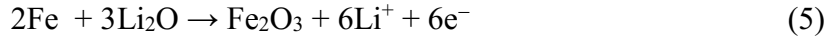
Based on the electrochemical and structural analysis of the NiFe₂O₄ anode during the 1st lithiation and de-lithiation presented above, a new lithium storage mechanism of NiFe₂O₄ is proposed without taking into account the possible formation of SEI. At the beginning of lithiation, lithium ions can enter both empty tetrahedral or octahedral sites in the spinel structure. However because of the strong repulsive interactions between Li⁺ and Fe³⁺ ions, tetrahedral site Fe³⁺ ions are reduced to Fe²⁺ and forced to move to the empty octahedral sites, c.f. Eq.(2). This structural relaxation has also been reported in many other spinel ferrites such as MgFe₂O₄[14], ZnFe₂O₄[20], MnFe₂O₄[36] and Fe₃O₄[37]. With further lithiation (uptake of up to 2 lithium per formula unit), the lithiated phase starts to decompose into Li₂O and rock-salt monoxide phases, c.f. Eq. (3). Unfortunately, we cannot determine the accurate chemical composition of the newly formed rock-salt phase because of the similar backscattering powers of Fe and Ni atoms. A simple Ni_{0.33}Fe_{0.67}O phase or a mixture of FeO and NiO phases are presumably formed at this voltage. As the cell is discharged to 0.1V, the monoxides are further reduced to metallic particles dispersed in a Li₂O matrix, c.f. Eq. (4). A total of 8 lithium ions are reacted with per formula unit NiFe₂O₄ in the course of 1st discharge.



3.2 Nano-crystalline NiFe₂O₄ anode



During de-lithiation, metallic iron and nickel are oxidized to Fe₂O₃ and NiO, respectively, corresponding to 8 lithium ions that can be delivered according to Eqs. (5) and (6).



4. Conclusions

X-ray absorption spectroscopy was used to investigate electronic and local structural modifications around Fe and Ni atoms in the inverse spinel ferrite NiFe₂O₄ anode material at various states of discharge and charge during the 1st cycle. Although Fe and Ni absorbers behave differently during cycling, both of them are reduced to the metallic state during lithiation and re-oxidized during subsequent de-lithiation as clearly observed by both XANES and EXAFS. At the onset of discharge to 0.95V, tetrahedral site Fe³⁺ ions are first reduced to Fe²⁺ and then displaced to octahedral sites due to the strong repulsive interactions between inserted Li⁺ ions and Fe²⁺ ions. This corresponds to the uptake of 2 lithium ions per unit formula. Unlike for Fe, no clear changes can be observed for Ni. Upon further lithiation, the spinel structure collapses and transforms to a rock-salt monoxide phase. However no signal from metallic iron or nickel can be observed as 6 lithium are inserted per formula unit at 0.75V, which indicates that the inserted lithium ions are possibly partially consumed due to the formation of SEI and other side reactions during the phase transition from spinel to rock-salt monoxide. Finally, the monoxide is reduced to metallic iron and nickel nanoparticles. The refined EXAFS results reveal that the metallic iron and nickel particles are highly disordered with a number of nearest neighbors of 6.0(8) and 8.1(4) for Fe and Ni, respectively. During the subsequent de-lithiation process, the metal particles are re-oxidized to highly disordered nano-sized Fe₂O₃ and NiO particles instead of the original spinel NiFe₂O₄.

Acknowledgements

This work is sponsored by the Helmholtz Association and the China Scholarship Council.

Reference

- [1] P. Poizot, S. Laruelle, S. Grugeon, L. Dupont, J.M. Tarascon, *Nature* 407 (2000) 496-499.
- [2] R. Alcántara, M. Jaraba, P. Lavela, J.L. Tirado, J.C. Jumas, J. Olivier-Fourcade, *Electrochemistry Communications* 5 (2003) 16-21.
- [3] J. Cabana, L. Monconduit, D. Larcher, M.R. Palacín, *Advanced Materials* 22 (2010) E170-E192.
- [4] J.B. Goodenough, Y. Kim, *Chemistry of Materials* 22 (2010) 587-603.
- [5] G. Zhou, D.-W. Wang, F. Li, L. Zhang, N. Li, Z.-S. Wu, L. Wen, G.Q. Lu, H.-M. Cheng, *Chemistry of Materials* 22 (2010) 5306-5313.
- [6] J. Jiang, Y. Li, J. Liu, X. Huang, C. Yuan, X.W. Lou, *Advanced Materials* 24 (2012) 5166-5180.
- [7] Y.-N. NuLi, Q.-Z. Qin, *Journal of Power Sources* 142 (2005) 292-297.
- [8] R. Kalai Selvan, N. Kalaiselvi, C.O. Augustin, C.H. Doh, C. Sanjeeviraja, *Journal of Power Sources* 157 (2006) 522-527.
- [9] X. Guo, X. Lu, X. Fang, Y. Mao, Z. Wang, L. Chen, X. Xu, H. Yang, Y. Liu, *Electrochemistry Communications* 12 (2010) 847-850.
- [10] P. Lavela, N.A. Kyeremateng, J.L. Tirado, *Materials Chemistry and Physics* 124 (2010) 102-108.
- [11] C. He, S. Wu, N. Zhao, C. Shi, E. Liu, J. Li, *ACS Nano* 7 (2013) 4459-4469.
- [12] A.S. Hameed, H. Bahiraei, M.V. Reddy, M.Z. Shoushtari, J.J. Vittal, C.K. Ong, B.V.R. Chowdari, *ACS Applied Materials & Interfaces* 6 (2014) 10744-10753.
- [13] L. Duan, Y. Wang, L. Wang, F. Zhang, L. Wang, *Materials Research Bulletin* 61 (2015) 195-200.
- [14] S. Permien, S. Indris, M. Scheuermann, U. Schurmann, V. Mereacre, A.K. Powell, L. Kienle, W. Bensch, *Journal of Materials Chemistry A* 3 (2015) 1549-1561.
- [15] M.V. Reddy, C.Y. Quan, K.W. Teo, L.J. Ho, B.V.R. Chowdari, *The Journal of Physical Chemistry C* 119 (2015) 4709-4718.
- [16] S. Permien, S. Indris, A.-L. Hansen, M. Scheuermann, D. Zahn, U. Schürmann, G. Neubüser, L. Kienle, E. Yegudin, W. Bensch, *ACS Applied Materials & Interfaces* 8 (2016) 15320-15332.

3.2 Nano-crystalline NiFe₂O₄ anode

- [17] S. Permien, S. Indris, U. Schürmann, L. Kienle, S. Zander, S. Doyle, W. Bensch, *Chemistry of Materials* 28 (2016) 434-444.
- [18] C.T. Cherian, M.V. Reddy, G.V.S. Rao, C.H. Sow, B.V.R. Chowdari, *Journal of Solid State Electrochemistry* 16 (2012) 1823-1832.
- [19] J.-M. Tarascon, S. Grugeon, M. Morcrette, S. Laruelle, P. Rozier, P. Poizot, *Comptes Rendus Chimie* 8 (2005) 9-15.
- [20] D. Bresser, E. Paillard, R. Kloepsch, S. Krueger, M. Fiedler, R. Schmitz, D. Baither, M. Winter, S. Passerini, *Advanced Energy Materials* 3 (2013) 513-523.
- [21] Y. Ding, Y. Yang, H. Shao, *Journal of Power Sources* 244 (2013) 610-613.
- [22] C.T. Cherian, J. Sundaramurthy, M.V. Reddy, P. Suresh Kumar, K. Mani, D. Pliszka, C.H. Sow, S. Ramakrishna, B.V.R. Chowdari, *ACS Applied Materials & Interfaces* 5 (2013) 9957-9963.
- [23] S.D. Kelly, K.M. Kemner, J.B. Fein, D.A. Fowle, M.I. Boyanov, B.A. Bunker, N. Yee, *Geochim. Cosmochim. Acta* 66 (2002) 3855-3871.
- [24] B. Ravel, M. Newville, *Journal of Synchrotron Radiation* 12 (2005) 537-541.
- [25] A.L. Ankudinov, B. Ravel, J.J. Rehr, S.D. Conradson, *Physical Review B* 58 (1998) 7565-7576.
- [26] G. Balachandran, D. Dixon, N. Bramnik, A. Bhaskar, M. Yavuz, L. Pfaffmann, F. Scheiba, S. Mangold, H. Ehrenberg, *ChemElectroChem* 2 (2015) 1510-1518.
- [27] J. Wong, F.W. Lytle, R.P. Messmer, D.H. Maylotte, *Physical Review B* 30 (1984) 5596-5610.
- [28] C.M.B. Henderson, J.M. Charnock, D.A. Plant, *Journal of Physics: Condensed Matter* 19 (2007) 076214.
- [29] M.M. Thackeray, W.I.F. David, J.B. Goodenough, *Materials Research Bulletin* 17 (1982) 785-793.
- [30] C.J. Chen, M. Greenblatt, J.V. Waszczak, *Solid State Ionics* 18–19, Part 2 (1986) 838-846.
- [31] R. Dedryvère, S. Laruelle, S. Grugeon, P. Poizot, D. Gonbeau, J.M. Tarascon, *Chemistry of Materials* 16 (2004) 1056-1061.
- [32] E. Sobczak, N.N. Dorozhkin, *Journal of Alloys and Compounds* 286 (1999) 108-113.

3.2 Nano-crystalline NiFe₂O₄ anode

[33] D. Carta, M.F. Casula, A. Falqui, D. Loche, G. Mountjoy, C. Sangregorio, A. Corrias, *The Journal of Physical Chemistry C* 113 (2009) 8606-8615.

[34] A.V. Chadwick, *Solid State Ionics* 177 (2006) 2481-2485.

[35] A.V. Chadwick, S.L.P. Savin, S. Fiddy, R. Alcántara, D. Fernández Lisboa, P. Lavela, G.F. Ortiz, J.L. Tirado, *The Journal of Physical Chemistry C* 111 (2007) 4636-4642.

[36] S. Permien, H. Hain, M. Scheuermann, S. Mangold, V. Mereacre, A.K. Powell, S. Indris, U. Schurmann, L. Kienle, V. Duppel, S. Harm, W. Bensch, *RSC Advances* 3 (2013) 23001-23014.

[37] S. Komaba, T. Mikumo, N. Yabuuchi, A. Ogata, H. Yoshida, Y. Yamada, *Journal of The Electrochemical Society* 157 (2010) A60-A65.

3.2.1 Supporting information

Table S.1: Fe EXAFS fit parameters for NiFe₂O₄ anode in the pristine state.

$S_o^2 = 0.83(8)$	$\Delta E_0 = 2.4(1.5)$					
Path	N_{degen}	$R_{theory}(\text{\AA})$	$\alpha_{fit}(\text{\AA})$	$\Delta R(\text{\AA})$	$R_{fit}(\text{\AA})$	$\sigma_{fit}^2(\text{\AA}^2)$
Fe-O	4	1.897	-0.016(4)	-0.030(8)	1.867(8)	0.008(1)
Fe-O	6	1.992	-0.016(4)	-0.030(8)	1.962(8)	0.022(15)
Fe-Fe	6	2.901	0.018(3)	0.052(9)	2.953(9)	0.010(1)
Fe-Fe	4	3.410	0.011(3)	0.038(10)	3.448(10)	0.009(1)
Fe-O	12	3.433	-0.069(16)	-0.237(54)	3.196(54)	0.022(15)
Fe-O	2	3.446	-0.069(16)	-0.238(55)	3.208(55)	0.022(15)
Fe-Fe	4	3.563	0.018(3)	0.064(10)	3.627(10)	0.009(1)
Fe-O	6	3.603	-0.069(16)	-0.249(58)	3.354(58)	0.022(15)

Table S.2: Fe EXAFS fit parameters for NiFe₂O₄ anode discharged to 0.95 V.

$S_o^2 = 0.87(8)$	$\Delta E_0 = 2.2(9)$					
Path	N_{degen}	$R_{theory}(\text{\AA})$	$\alpha_{fit}(\text{\AA})$	$\Delta R(\text{\AA})$	$R_{fit}(\text{\AA})$	$\sigma_{fit}^2(\text{\AA}^2)$
Fe-O	6	1.992	-0.005(4)	-0.010(8)	1.982(8)	0.013(2)
Fe-Fe	6	2.901	0.018(3)	0.052(9)	2.953(9)	0.012(1)
Fe-O	2	3.446	-0.051(4)	-0.176(14)	3.270(14)	0.0030(2)
Fe-O	6	3.603	-0.051(4)	-0.184(14)	3.419(14)	0.0030(2)

3.2 Nano-crystalline NiFe₂O₄ anode

Table S.3: Fe EXAFS fit parameters for NiFe₂O₄ anode discharged to 0.1 V.

$S_o^2 = 0.72$	$\Delta E_0 = -3.4(1.8)$					
Path	N_{degen}	$R_{theory}(\text{\AA})$	$\alpha_{fit}(\text{\AA})$	$\Delta R(\text{\AA})$	$R_{fit}(\text{\AA})$	$\sigma_{fit}^2(\text{\AA}^2)$
Fe-Fe	6.0(8)	2.539	-0.032(4)	-0.082(9)	2.457(9)	0.012(1)
Fe-Fe	6	2.932	-0.045(16)	-0.132(47)	2.800(47)	0.037(10)
Fe-Fe	12	4.146	-0.031(12)	-0.129(50)	4.017(50)	0.041(6)
Fe-Fe	24	4.861	-0.031(12)	-0.150(58)	4.711(58)	0.041(6)
Fe-Fe	8	5.078	-0.031(12)	-0.157(61)	4.921(61)	0.041(6)

Table S.4: Fe EXAFS fit parameters for reference Fe foil.

$S_o^2 = 0.72(6)$	$\Delta E_0 = 1.2(5)$					
Path	N_{degen}	$R_{theory}(\text{\AA})$	$\alpha_{fit}(\text{\AA})$	$\Delta R(\text{\AA})$	$R_{fit}(\text{\AA})$	$\sigma_{fit}^2(\text{\AA}^2)$
Fe-Fe	8	2.539	-0.030(1)	-0.076(4)	2.463(4)	0.005(1)
Fe-Fe	6	2.932	-0.033(2)	-0.097(6)	2.835(6)	0.006(1)
Fe-Fe	12	4.146	-0.025(1)	-0.104(4)	4.042(4)	0.008(1)
Fe-Fe	24	4.861	-0.025(1)	-0.122(5)	4.739(5)	0.008(1)
Fe-Fe	8	5.078	-0.025(1)	-0.127(5)	4.951(5)	0.008(1)

3.2 Nano-crystalline NiFe₂O₄ anode

Table S.5: Fe EXAFS fit parameters for NiFe₂O₄ anode charged to 3.0 V.

$S_o^2 = 0.67(8)$	$\Delta E_0 = -7.0(1.7)$					
Path	N_{degen}	$R_{theory}(\text{\AA})$	$\alpha_{fit}(\text{\AA})$	$\Delta R(\text{\AA})$	$R_{fit}(\text{\AA})$	$\sigma_{fit}^2(\text{\AA}^2)$
Fe-O	3	1.983	-0.050(5)	-0.100(10)	1.883(10)	0.010(1)
Fe-O	3	2.062	-0.050(5)	-0.100(10)	1.962(10)	0.010(1)
Fe-Fe	1	2.887	0.005(6)	0.014(17)	2.901(17)	0.015(3)
Fe-Fe	3	2.970	0.005(6)	0.015(18)	2.985(18)	0.015(3)
Fe-Fe	3	3.367	-0.094(16)	-0.316(54)	3.051(54)	0.027(10)
Fe-O	3	3.368	0.018(13)	-0.061(44)	3.307(44)	0.009(6)
Fe-O	3	3.616	0.018(13)	-0.065(47)	3.551(47)	0.009(6)
Fe-Fe	6	3.704	-0.094(16)	-0.348(59)	3.356(59)	0.027(10)
Fe-O	3	3.848	0.018(13)	-0.069(50)	3.779(50)	0.009(6)
Fe-Fe	1	3.990	-0.094(16)	-0.375(64)	3.615(64)	0.027(10)

3.2 Nano-crystalline NiFe₂O₄ anode

Table S.6: Fe EXAFS fit parameters for reference Fe₂O₃ oxide.

$S_o^2 = 1.00(14)$	$\Delta E_0 = 5.6(1.3)$					
Path	N_{deg}	$R_{theory}(\text{\AA})$	$\alpha_{fit}(\text{\AA})$	$\Delta R(\text{\AA})$	$R_{fit}(\text{\AA})$	$\sigma_{fit}^2(\text{\AA}^2)$
Fe-O	3	1.983	-0.018(6)	-0.035(12)	1.948(12)	0.013(2)
Fe-O	3	2.062	-0.018(6)	-0.037(12)	2.025(12)	0.013(2)
Fe-Fe	1	2.887	-0.005(4)	-0.014(12)	2.873(12)	0.007(1)
Fe-Fe	3	2.970	-0.005(4)	-0.015(12)	2.955(12)	0.007(1)
Fe-Fe	3	3.367	-0.006(3)	-0.020(10)	3.347(10)	0.009(1)
Fe-O	3	3.368	0.026(18)	0.088(61)	3.456(61)	0.009(8)
Fe-O	3	3.616	0.026(18)	0.094(65)	3.710(65)	0.009(8)
Fe-Fe	6	3.704	-0.006(3)	-0.022(11)	3.682(11)	0.009(1)
Fe-O	3	3.848	0.026(18)	0.100(69)	3.748(69)	0.009(8)
Fe-Fe	1	3.990	-0.006(3)	-0.024(12)	3.966(5)	0.009(1)

Table S.7: Ni EXAFS fit parameters for NiFe₂O₄ anode in the pristine state.

$S_o^2 = 1.18(8)$	$\Delta E_0 = 5.7(7)$					
Path	N_{deg}	$R_{theory}(\text{\AA})$	$\alpha_{fit}(\text{\AA})$	$\Delta R(\text{\AA})$	$R_{fit}(\text{\AA})$	$\sigma_{fit}^2(\text{\AA}^2)$
Ni-O	6	1.992	0.031(3)	0.062(6)	1.930(6)	0.009(1)
Ni-Ni	6	2.909	0.011(2)	0.032(6)	2.941(6)	0.009(1)
Ni-Ni	6	3.411	0.003(4)	0.010(12)	3.421(12)	0.010(2)
Ni-O	2	3.446	-0.014(6)	-0.048(20)	3.398(20)	0.002(3)
Ni-O	6	3.603	-0.014(6)	-0.050(22)	3.553(22)	0.002(3)

3.2 Nano-crystalline NiFe₂O₄ anode

Table S.8: Ni EXAFS fit parameters for NiFe₂O₄ anode discharged to 0.95 V.

$S_o^2 = 1.14(13)$	$\Delta E_0 = 7.5(1.2)$					
Path	N_{degen}	$R_{theory}(\text{\AA})$	$\alpha_{fit}(\text{\AA})$	$\Delta R(\text{\AA})$	$R_{fit}(\text{\AA})$	$\sigma_{fit}^2(\text{\AA}^2)$
Ni-O	6	1.992	0.036(5)	0.073(10)	1.919(10)	0.010(2)
Ni-Ni	6	2.909	0.013(3)	0.038(9)	2.947(9)	0.008(1)
Ni-Ni	6	3.411	0.004(8)	0.014(28)	3.425(28)	0.011(3)
Ni-O	2	3.446	-0.008(10)	-0.028(34)	3.418(34)	0.001(4)
Ni-O	6	3.603	-0.008(10)	-0.029(36)	3.574(36)	0.001(4)

Table S.9: Ni EXAFS fit parameters for NiFe₂O₄ anode discharged to 0.1 V.

$S_o^2 = 0.9$	$\Delta E_0 = -2.8(7)$					
Path	N_{degen}	$R_{theory}(\text{\AA})$	$\alpha_{fit}(\text{\AA})$	$\Delta R(\text{\AA})$	$R_{fit}(\text{\AA})$	$\sigma_{fit}^2(\text{\AA}^2)$
Ni-Ni	8.1(4)	2.503	-0.017(2)	-0.042(5)	2.461(5)	0.015(1)
Ni-Ni	6	3.540	-0.010(8)	-0.035(28)	3.505(28)	0.030(4)
Ni-Ni	24	4.336	0.002(13)	0.009(58)	4.345(58)	0.053(10)
Ni-Ni	12	5.006	0.002(13)	0.010(65)	4.996(65)	0.053(10)

3.2 Nano-crystalline NiFe₂O₄ anode

Table S.10: Ni EXAFS fit parameters for reference Ni foil.

$S_o^2 = 0.89(5)$	$\Delta E_0 = 2.9(6)$					
Path	N_{degen}	$R_{theory}(\text{\AA})$	$\alpha_{fit}(\text{\AA})$	$\Delta R(\text{\AA})$	$R_{fit}(\text{\AA})$	$\sigma_{fit}^2(\text{\AA}^2)$
Ni-Ni	12	2.503	-0.009(1)	-0.022(2)	2.481(2)	0.007(0)
Ni-Ni	6	3.540	-0.008(3)	-0.028(10)	3.512(10)	0.010(1)
Ni-Ni	24	4.336	-0.002(1)	-0.009(4)	4.327(4)	0.010(1)
Ni-Ni	12	5.006	-0.002(1)	-0.010(5)	4.996(5)	0.010(1)

Table S.11: Ni EXAFS fit parameters for NiFe₂O₄ anode charged to 3.0 V.

$S_o^2 = 0.73(8)$	$\Delta E_0 = 7.5(1.0)$					
Path	N_{degen}	$R_{theory}(\text{\AA})$	$\alpha_{fit}(\text{\AA})$	$\Delta R(\text{\AA})$	$R_{fit}(\text{\AA})$	$\sigma_{fit}^2(\text{\AA}^2)$
Ni-O	6	2.089	-0.024(4)	-0.050(8)	2.039(8)	0.010(1)
Ni-Ni	12	2.954	0.005(3)	0.015(9)	2.969(9)	0.019(1)
Ni-O	8	3.618	-0.038(28)	-0.137(101)	3.481(101)	0.033(18)
Ni-Ni	6	4.178	0.003(13)	0.013(54)	4.165(54)	0.030(6)
Ni-O	24	4.671	-0.006(12)	-0.028(56)	4.643(56)	0.026(12)
Ni-Ni	24	5.117	0.008(5)	0.041(26)	5.158(26)	0.024(3)

3.2 Nano-crystalline NiFe₂O₄ anode

Table S.12: Ni EXAFS fit parameters for reference NiO oxide.

$S_o^2 = 1.11(8)$	$\Delta E_0 = 9.6(7)$					
Path	N_{degen}	$R_{theory}(\text{\AA})$	$\alpha_{fit}(\text{\AA})$	$\Delta R(\text{\AA})$	$R_{fit}(\text{\AA})$	$\sigma_{fit}^2(\text{\AA}^2)$
Ni-O	6	2.089	-0.001(4)	-0.003(12)	2.086(12)	0.007(1)
Ni-Ni	12	2.954	0.002(1)	0.006(3)	2.960(3)	0.007(1)
Ni-O	8	3.618	-0.015(9)	-0.054(32)	3.564(32)	0.011(5)
Ni-Ni	6	4.178	0.0003(17)	0.001(7)	4.179(7)	0.009(1)
Ni-O	24	4.671	-0.006(3)	-0.028(14)	4.643(14)	0.006(2)
Ni-Ni	24	5.117	0.005(2)	0.026(10)	5.143(10)	0.007(1)

3.3 Nano-crystalline ZnFe₂O₄ anode material

Local structural changes of nano-crystalline ZnFe₂O₄ during lithiation and de-lithiation studied by X-ray absorption spectroscopy

Dong Zhou^a, Haiping Jia^b, Jatinkumar Rana^a, Tobias Placke^b, Tobias Scherb^a, Richard Kloepsch^b, Gerhard Schumacher^a, Martin Winter^{b,c}, John Banhart^{a,d}

^a Helmholtz-Zentrum Berlin für Materialien und Energie, Hahn-Meitner-Platz 1, 14109 Berlin, Germany

^b University of Münster, MEET Battery Research Center & Institute of Physical Chemistry, Corrensstr. 46&28/30, 48149 Münster, Germany

^c Helmholtz Institute Münster, IEK-12, Forschungszentrum Jülich GmbH, Corrensstr. 46, 48149 Münster, Germany

^d Technische Universität Berlin, Materials Science and Technology, Hardenberg str. 36, 10623 Berlin, Germany

Abstract

X-ray absorption spectroscopy was carried out to investigate the electronic and local structural changes around Fe and Zn atoms of the nano-crystalline spinel ferrite ZnFe₂O₄ anode material at various states-of-charge during the 1st and 2nd lithiation/de-lithiation. From the X-ray absorption near edge structure (XANES) and extended X-ray absorption fine structure (EXAFS), we propose a possible structure evolution process of the ZnFe₂O₄ electrode during the 1st discharge and charge cycle. A mixture of metallic iron, ZnO, metallic zinc, LiZn and Li₂O phases seems to be formed as the cell is firstly discharged to 0.02 V. Instead of the original ZnFe₂O₄ spinel phase, the metallic iron and zinc particles are re-oxidized to Fe₂O₃ and ZnO phases during the subsequent de-lithiation. A reversible redox reaction between Fe₂O₃, ZnO and lithium ions is found in the 2nd cycle. The formation of SEI layer in the initial cycles plays a major role in the irreversible capacity of the electrode. The inactive disordered ZnO formed due to the conversion reaction of ZnFe₂O₄ during the 1st lithiation is probably the main reason for the poor electrochemical behavior of the nano-crystalline ZnFe₂O₄ electrode.

1. Introduction

In recent years, conversion materials, in particular transition metal oxides (TMOs), have attracted great research interest as they are potential candidates for next-generation anodes in lithium-ion batteries. This is due to their high theoretical capacity compared to graphite, which is still the most common and state-of-the-art lithium intercalation anode material[1-3]. Nevertheless, conversion materials typically suffer from a high average de-lithiation potential (> 1 V vs. Li/Li⁺) compared to graphite anodes (0.2 V vs. Li/Li⁺), which results in a low cell voltage in combination with a cathode material and, thus, in low energy densities and specific energies. Furthermore, conversion materials exhibit a large voltage hysteresis, which leads to a poor energy efficiency[4, 5]. The lithium storage mechanism of TMO materials is based on the reduction and re-oxidization of transition metals to metallic nanoparticles during lithiation and de-lithiation, which is called the conversion reaction[1, 6]. Among the TMOs, iron oxide appears favorable as it is naturally abundant, environmentally friendly, and biocompatible for lithium ions. The capacity of iron oxide TMO can be increased by replacing one iron atom by zinc as lithium ions intercalate into zinc and form an alloy. This leads to an enhancement of theoretical capacity from 926 mAh g⁻¹ (Fe₃O₄) to 1000 mAh g⁻¹ (ZnFe₂O₄)[7].

Unfortunately, the capacity of ZnFe₂O₄ electrodes fades fast within few cycles due to the formation of the solid electrolyte interphase (SEI)[8], which results in a loss of active lithium, and loss of the mechanical integrity caused by the drastic volume changes upon cycling[7, 9, 10]. Therefore, various nanostructured materials such as carbon coated ZnFe₂O₄[7], yolk-shell structured ZnFe₂O₄[11], porous ZnFe₂O₄/α-Fe₂O₃[12] and others[4, 13, 14] have been designed to attend a higher capacity and cycle life.

Due to limitations of the most frequently used techniques for clarifying the lithium storage and fading mechanism during discharge and charge, such as *ex-situ/in-situ* X-ray diffraction (XRD), transmission electron microscopy (TEM), X-ray photoelectron spectroscopy (XPS) and Mössbauer spectroscopy, the conversion reaction is still not well understood. For example, no reflections are observed during *in-situ* XRD measurements on TMO electrodes when the cell is deeply discharged and charged back, as the crystalline grains of the newly formed phases are probably too small to be detected by XRD[1, 7, 15]. On the other hand, XPS measurements can only provide surface information of the electrodes with a limited probing depth (5nm to 10 nm).

3.3 Nano-crystalline ZnFe₂O₄ anode

A better understanding of the conversion reactions occurring during lithiation and de-lithiation in TMO electrodes is urgently needed in order to improve the electrochemical properties of existing and new high-performance electrode materials.

X-ray absorption spectroscopy (XAS) is promising technique to clarify chemical and local structural changes in TMO electrodes since it can provide both chemical and structural information of each absorbing atom in the materials during cycling. The X-ray absorption near edge structure (XANES) caused by the transition of a core electron to bound states yields information about the valence state, chemical bonding and site symmetry of absorbing atoms. The Extended X-ray absorption fine structure (EXAFS) results from the scattering of excited photons by neighbors around absorbers, provides quantitative local structural information of absorbing atoms such as the metal-ligand bond length, coordination number and Debye-Waller factor by refining the data to a model structure[16].

In this paper, X-ray absorption near edge structure (XANES) and extend X-ray absorption fine structure (EXAFS) measurements were employed to elucidate the electrical and local structural changes of nano-crystalline ZnFe₂O₄ used as an anode material during the conversion reaction upon lithiation and de-lithiation in the first two discharge/charge cycles.

2. Experimental

The XRD measurement of pristine ZnFe₂O₄ was performed on a Bruker D8 Advance X-ray diffractometer (Bruker AXS GmbH, Cu-K α radiation, $\lambda = 0.154$ nm). The morphology of ZnFe₂O₄ nanoparticles was investigated using a field emission scanning electron microscope (Carl Zeiss AURIGA, Carl Zeiss Microscopy GmbH).

Electrodes based on ZnFe₂O₄ nanoparticles (particle size <100 nm, purity: >99% trace metal basis, Sigmal-Aldrich) were prepared by mixing 75 wt.% of active material, 15 wt.% of conductive carbon (Super C65, Imerys) and 10 wt.% of sodium carboxymethyl cellulose (Na-CMC; Walocel CRT 2000 PA 12, Dow Wolff Cellulosics). Firstly, the CMC was dissolved in deionized water to obtain a 1.5 wt.% solution. Then, Super C65 and ZnFe₂O₄ particles were added to the solution and ground with a planetary ball-mill for 2 h. The resulting electrode paste was cast on copper foil and dried in air at 20 °C for 2 hours. Square electrodes with an area of (35×35) mm² were cut out and dried under reduced pressure (< 0.1 mbar) at 120 °C for 12 h. The

3.3 Nano-crystalline ZnFe₂O₄ anode

mass loading of active material for each electrode is $\sim 2.5 \text{ mg cm}^{-2}$. Electrochemical charge and discharge cycling experiments were carried out in two-electrode pouch cells with high-purity lithium metal foils (Rockwood Lithium) as a counter electrode. A nano-porous polypropylene separator (Celgard 2400) was used and a 1M solution of LiPF₆ in mixture of a 30 wt.% ethylene carbonate (EC) and 70 wt.% diethyl carbonate (DEC), was used as electrolyte. The cells were assembled in a dry room with an atmospheric water content of less than 10 ppm. Galvanostatic cycling was performed at a Maccor Battery Test 4300 system in the voltage range between 0.02 V and 3.0 V at 20 °C. Cyclic voltammetry (CV) experiments were performed using a VMP multichannel constant-voltage/constant-current system (Bio-Logic Science Instruments). The scan rate for the CV measurements was 0.02 mVs^{-1} . After charging or discharging the cells to a certain state-of-charge, they were opened in a dry room and the electrodes were washed with DEC solution to remove the electrolyte salt. The active materials were ground and transferred to a 25 μm thick adhesive Kapton tape (Goodfellow) to obtain a homogenous XAS sample.

Ex situ XAS measurements at both the Fe and Zn K-edges on ZnFe₂O₄ samples at various states-of-charge of the first two cycles were performed at the beamline KMC-2 of the BESSY-II synchrotron light source, Berlin, Germany. A graded Si-Ge (111) double-crystal monochromator was used at this beamline and higher harmonics were rejected by detuning the monochromator such that the intensity of the beam at the sample location was 65% of the maximum possible intensity. Pure metal foil was measured simultaneously with each sample for an absolute energy calibration of the monochromator. The samples were measured in the transmission mode and an ionization chamber filled with a mixture of argon and nitrogen was used to get an optimum signal-to-noise ratio. The data were first processed by using the software *ATHENA*[17, 18]. All spectra were energy-calibrated with respect to the first peak in the derivative spectrum of the corresponding pure metal spectrum. Normalized EXAFS signals were transformed to k space and multiplied by k^3 in order to compensate for signal damping at high k -values. Then the k^3 -weighted $\chi(k)$ signal was Fourier transformed without phase shift correction. The model function was calculated by using the code *FEFF8.2*[19] and fitted to the data using the software *ARTEMIS* of the package *IFEFFIT*. The fractional change α_{fit} of bond length and mean-squared relative displacement parameters σ^2 for each coordination shell were refined in each fit. The parameters for multiple scattering paths (α_{fit} and σ^2) were constrained in terms of those of corresponding single scattering paths. The amplitude reduction factor S_0^2 is constrained to the value obtained by

fitting the EXAFS data of the pure iron foil (S_0^2 : 0.72). The quality of each EXAFS fit was judged based on its R-factor.

3. Results

3.1 Morphological and structural characterization of ZnFe₂O₄ particles

The morphology and particle size of the nano-crystalline ZnFe₂O₄ powders are revealed by scanning electron microscopy (SEM) and the results are displayed in Figure 1. The nanoparticles agglomerate with each other showing an average particle size of 40 ± 10 nm.

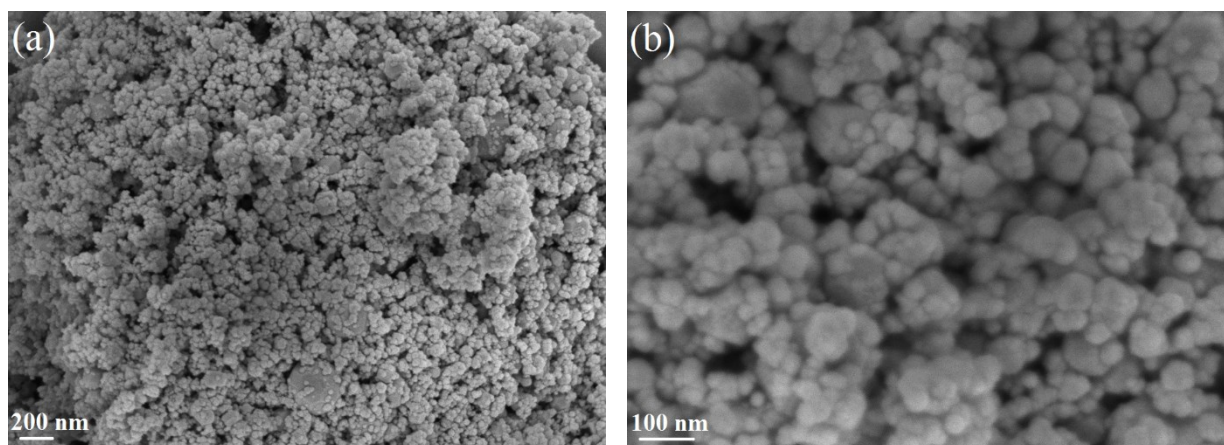


Figure 1. SEM images of ZnFe₂O₄ powder.

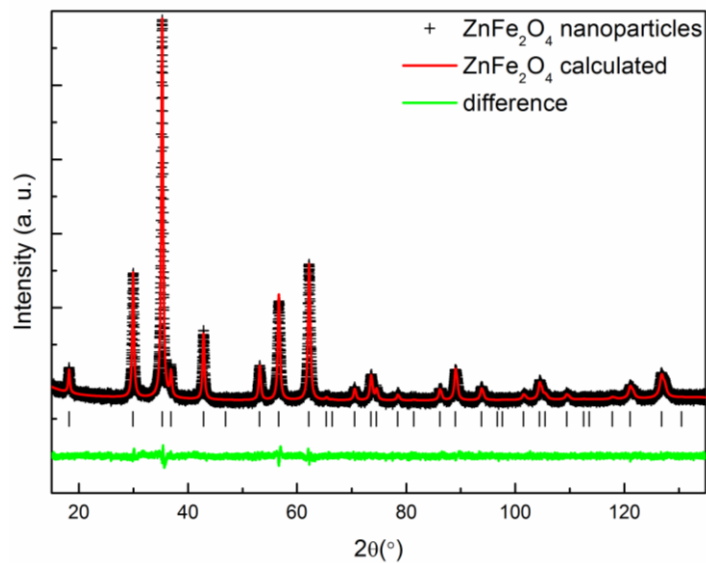


Figure 2. XRD pattern of the ZnFe₂O₄ nanoparticles. The calculated X-ray pattern of ZnFe₂O₄ is shown for comparison.

3.3 Nano-crystalline ZnFe₂O₄ anode

Figure 2. shows the powder XRD pattern of ZnFe₂O₄ nanoparticles. All of diffraction reflections can be indexed to a cubic spinel structure with a space group $Fd\bar{3}m$ (No. 227, PDF card No. 04-008-5691)[20] and a refined lattice parameter of $a = 8.4403(1)$ Å. No reflections from impurities are observed. To model the sample contribution to the peak profile the Double-Voigt approach is used. The instrumental contributions to the profile is calculated with the fundamental parameters approach implemented in *TOPAS 4.2* software and refined with a LaB6 standard (NIST660b). The instrumental contribution is kept fixed during the refinement of the ZnFe₂O₄ nano powder. The sample broadening is modeled with a set of four fit parameters (Cry Size L, Cry Size G, Strain L and Strain G). From these fit parameters, which have no direct physical meaning, the volume averaged column height, calculated from the integral breadth (L_{Vol}), is calculated. The relationship between the volume averaged column height, and the nominal crystallite dimensions (crystallite size) depend on the crystallite shape. The crystallite size L_C is estimated for spherical crystallites and calculated according to $L_C = 4/3 L_{Vol} = 27(1)$ nm.

3.2 Electrochemical analyses

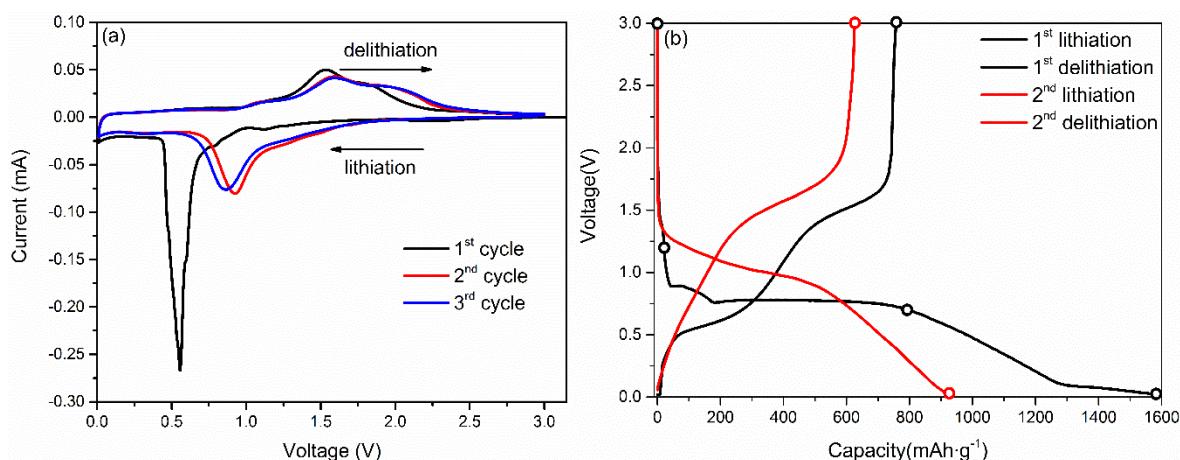


Figure 3. Electrochemical properties of nano-crystalline ZnFe₂O₄ powders during lithiation and delithiation: (a) cyclic voltammogram of the first three cycles and (b) voltage vs. specific capacity profiles for the 1st and 2nd discharge (D) or charge (C) cycles measured at constant current and using charge and discharge rates of 0.05 C (1 C = 1053 mA g⁻¹). Circles indicate the states-of-charge selected for XAS measurements.

The first three cyclic voltammograms (CVs) of the ZnFe₂O₄ electrode recorded at a scan rate of 0.02 mVs⁻¹ between 0.01 V and 3.0 V are shown in Figure 3a. Significant differences of the CV curves can be observed between the first and subsequent cycles, which is well known for the

3.3 Nano-crystalline ZnFe₂O₄ anode

conversion-type spinel electrodes. The sharp cathodic peak at 0.55 V in the first cycle corresponds to the reduction of transition metals to metallic state, formation of Li₂O and Li-Zn alloy[4, 7, 10, 20]. In the subsequent 2nd and 3rd cycles, one broad peak at 0.9 V is observed, which can be ascribed to the reversible reduction reaction of Fe₂O₃ and ZnO[21, 22]. Upon the anodic reaction in the first cycle, two broad peaks are observed at 1.5 V and 1.8 V, which are usually attributed to the oxidation of metallic zinc and iron to ZnO and Fe₂O₃, respectively[7, 10, 20]. The voltage profiles of ZnFe₂O₄ between 0.02 V and 3.0 V in the initial two cycles can be seen in Figure 3b. The nano-crystalline ZnFe₂O₄ shows discharge/charge capacities of 1590 and 750 mAh g⁻¹, respectively, in first cycle, and a corresponding Coulombic efficiency of 47%. The large irreversible capacity during the initial cycles is mainly caused by the formation of a solid electrolyte interface (SEI) layer and incomplete conversion reaction[7, 10, 11, 23]. The seven marked circles at various states-of-charge in the voltage profiles are studied by *ex situ* X-ray absorption spectroscopy.

3.3 XANES

The normalized Fe and Zn K-edge XANES spectra of ZnFe₂O₄ at various states-of-charge in the 1st and 2nd cycle are shown in Figure 4a, 4b, 4c and 4d, respectively. For 3d transition metal oxides, K-edge XANES spectra feature two peaks: the pre-edge peak and the main absorption edge peak. The former can be interpreted by the dipole forbidden 1s to 3d transition, while the main peak is due to the 1s to 4p transition. In the case of the Fe K-edge in Figure 4a, both the pre-edge peak (~7113 eV) and the main edge peak (~7133 eV) can be observed for the pristine spinel ZnFe₂O₄, and these two peaks are located closely to that of the Fe₂O₃ reference oxide. At the beginning of discharge (= lithiation), no clear changes can be seen except for a small shift of the main edge to a lower energy. Considerable differences can be observed with further lithiation. The main edge becomes smooth and looks identical to that of the reference iron foil as the cell is discharged to 0.7 V. At the end of discharge and subsequent charge in the 1st cycle, the spectrum remains without obvious shape changes. After the cell has been discharged to 0.02 V in 2nd cycle, the spectrum is consistent with that of the first fully discharged cell, thus proving good reversibility. After this, the main absorption edge becomes sharper and shifts back to ~7133 eV as shown in Figure 4b when the cell is charged (= de-lithiation) to 3.0 V again in the 2nd cycle.

3.3 Nano-crystalline ZnFe₂O₄ anode

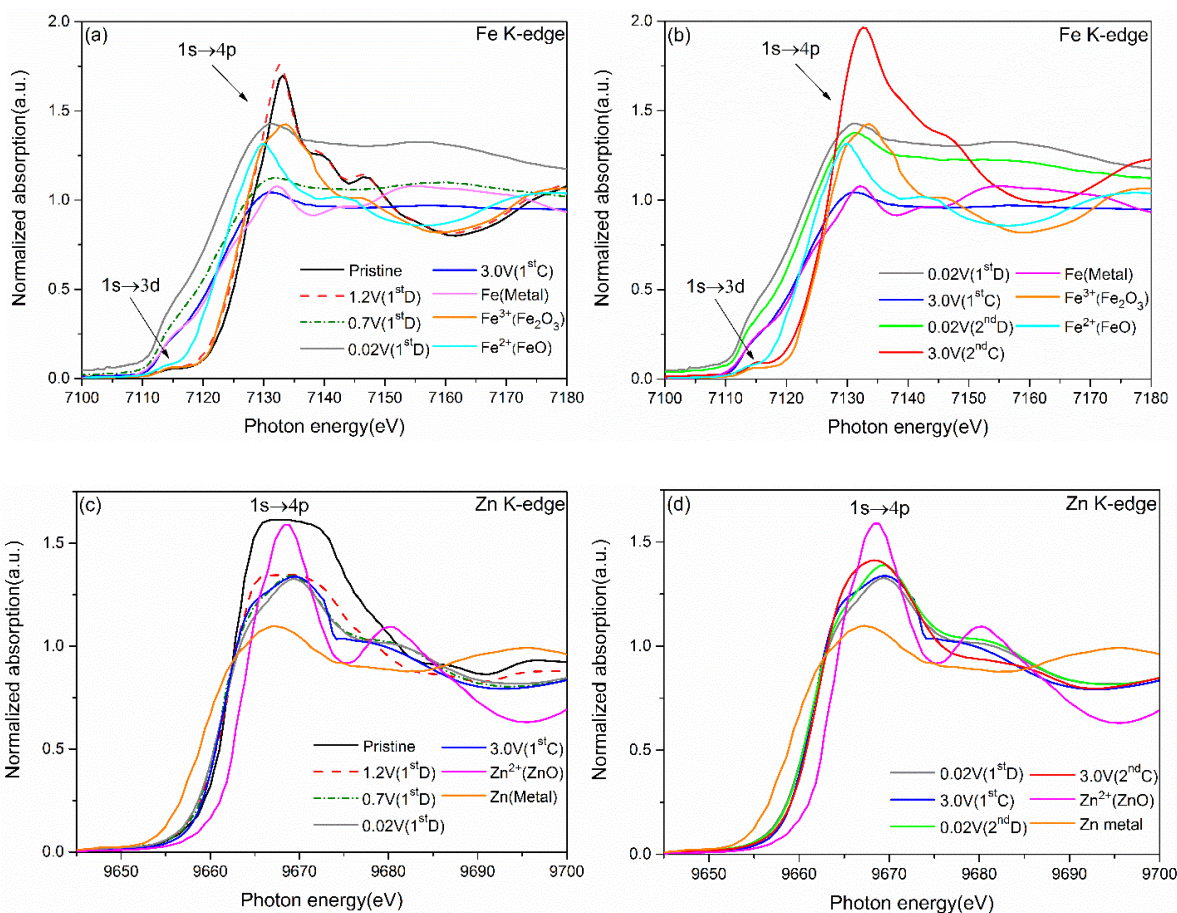


Figure 4. Normalized absorption spectra at the Fe (a, b) and Zn (c, d) K-edge of ZnFe₂O₄ in various states-of-charge in the 1st and 2nd cycle. Notations: 1.2 V (1st D) means the cell was discharged to 1.2 V in first cycle, and so on. 3.0 V (1st C) means the cell was charged to 3.0 V after it had been discharged to 0.02 V in 1st cycle.

Unlike Fe K-edge XANES, no pre-edge peak can be observed at the Zn K-edge because of the fully occupied 3d orbitals of Zn as shown in both Figure 4c and 4d. The main edge of the pristine ZnFe₂O₄ is close to that of ZnO at ~9668 eV, but the peak is broader. According to literature reports, the shape and energy position of absorption edges in XANES mainly depend on the coordination number, ligand symmetry and oxidation state of the absorber[16]. The broad main edge peak of the pristine spinel ZnFe₂O₄ probably results from the cationic exchange in nm-sized ZnFe₂O₄[24-26]. In normal spinel ZnFe₂O₄, Zn²⁺ ions occupy tetrahedral sites, while Fe³⁺ ions are located at octahedral sites. However, when the particle size of ZnFe₂O₄ decreases to the nm-scale, ZnFe₂O₄ shows a mixed spinel structure where Zn²⁺ and Fe³⁺ ions are distributed at both tetrahedral and octahedral sites[26]. As the cell is discharged to 0.7 V, a weak absorption peak

3.3 Nano-crystalline ZnFe₂O₄ anode

risers at ~9665 eV, which locates at slightly lower energy than for the reference zinc metal. Interestingly, during the following discharge to 0.02 V and subsequent charge to 3.0 V in the 1st cycle, no clear changes can be observed in Figure 4d. The spectra of the cycled samples (2nd cycle) are similar to those of the samples in the same voltage states in the 1st cycle.

3.4 EXAFS

The k^3 -weighted EXAFS $\chi(k)$ signals at the Fe K-edge of ZnFe₂O₄ and their corresponding Fourier transforms are shown in Figure 5a and 5b, respectively. At the beginning of discharge to 1.2 V, no changes can be seen in the $\chi(k)$ signal. As the cell is discharged to 0.7 V, the shape of the signal varies along with an amplitude suppression. With further discharge to 0.02 V, the signal remains and minute changes can be observed during subsequent charge to 3.0 V. As the cell is discharged to 0.02 V in the 2nd cycle, the signal overlaps with that of the first fully discharged state. In contrast, clear differences between the signals of the charged (= de-lithiated) samples in the 1st and 2nd cycle can be seen. In the corresponding Fourier transforms in Figure 5b, three main peaks are visible below 4 Å for pristine ZnFe₂O₄, located at R ~1.7 Å, ~2.8 Å and ~3.2 Å. The first peak arises from the backscattering of oxygen anions in the first coordinate shell, while the second and third peaks are mainly due to scattering from second nearest neighbors[27]. For spinel ferrite, the peak structure between 2 Å and 4 Å is highly correlated to the cation distribution. If the central absorbing cations occupied octahedral sites in the structure, a strong peak at R ~2.6 Å should be seen in r-space together with a small peak at ~3.1 Å. On the contrary, there will be one strong peak centered at round 3.1 Å if the cations reside on tetrahedral sites. Therefore, the two peaks at R ~2.8 Å and ~3.2 Å presented here signify the occupation of Fe³⁺ cations at both tetrahedral and octahedral sites in the structure, which is consistent with the literature[24-26, 28].

As the cell is discharged to 1.2 V, the spectrum appears unchanged. Unexpectedly, after further discharge to 0.7 V, only one intensive peak at 1.7 Å to 3.0 Å can be observed, which remains till the end of discharge to 0.02 V. Similar results have been reported by other groups who attributed this peak to the scattering of the first-shell Fe neighbors in disordered metallic iron[29, 30]. During subsequent charge to 3.0 V (1st cycle), the broad peak splits into one small peak at 1.1 Å - 1.7 Å (Fe-O) and one intensive peak at ~2.1 Å (Fe-Fe_{metal}), respectively. As the cell is discharged

3.3 Nano-crystalline ZnFe₂O₄ anode

to 0.02 V in the 2nd cycle, the broad Fe-Fe_{metal} peak reappears and then vanishes during subsequent charge back to 3.0 V.

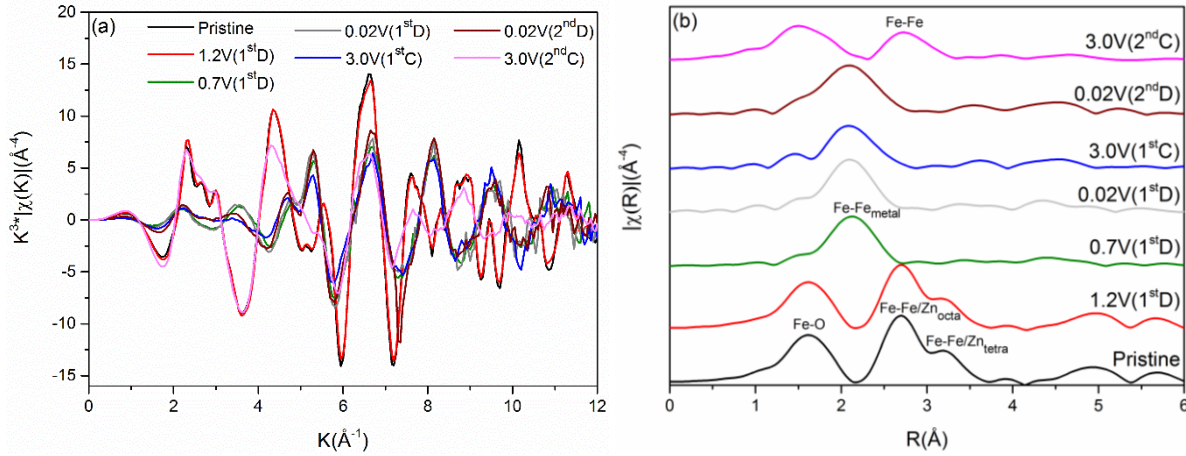


Figure 5. k^3 -weighted EXAFS $\chi(k)$ signals (a) and their Fourier transforms (b) at the Fe K-edge of ZnFe₂O₄ in various states during the 1st and 2nd discharge or charge cycles. Notations: In Figure 5b, Fe-O corresponds to oxygen atoms in the 1st shell around Fe absorbers, Fe-Fe/Zn_{octa} to Fe/Zn atoms situated on an octahedral site in the 2nd shell around Fe absorbers, Fe-Fe/Zn_{tetra} to Fe/Zn atoms situated on a tetrahedral site around Fe absorbers, Fe-Fe_{metal} to Fe atoms in the 1st shell around Fe absorbers in metallic iron, Fe-Fe to Fe atoms in the 2nd shell around Fe absorbers in Fe₂O₃.

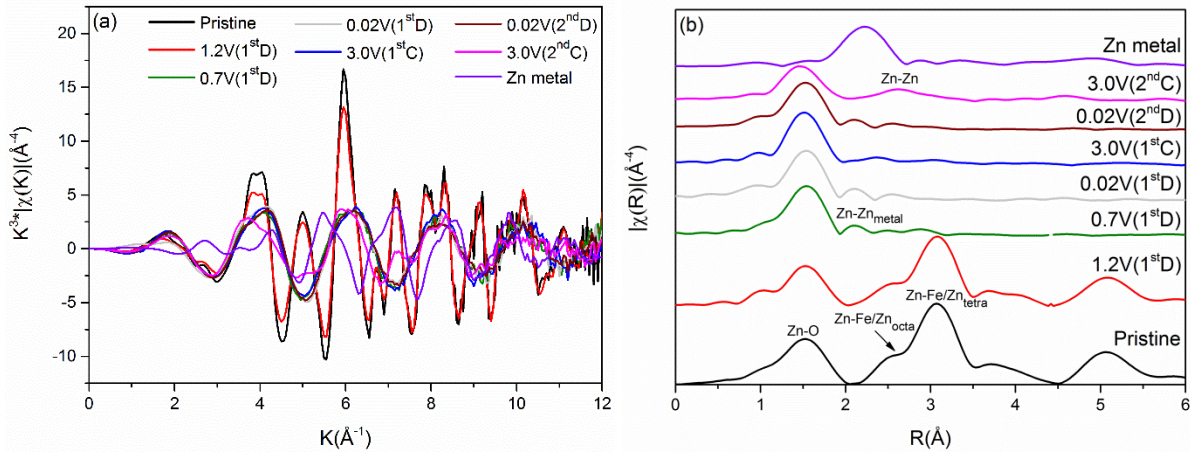


Figure 6. k^3 -weighted EXAFS $\chi(k)$ signals (a) and their Fourier transforms (b) at the Zn K-edge of ZnFe₂O₄ in various states during the 1st and 2nd discharge or charge cycles. Notations: In Figure 6b, Zn-O corresponds to oxygen atoms in the 1st shell around Zn absorbers, Zn-Fe/Zn_{octa} to Fe/Zn atoms situated on an octahedral site in the 2nd shell around Zn absorbers, Zn-Fe/Zn_{tetra} to Fe/Zn atoms situated on a tetrahedral site around Zn absorbers, Zn-Zn_{metal} to Zn atoms in the 1st shell around Zn absorbers in metallic zinc, Zn-Zn to Zn atoms in the 2nd shell around Zn absorbers in ZnO.

3.3 Nano-crystalline ZnFe₂O₄ anode

Figure 6a and 6b illustrate the k^3 -weighted EXAFS $\chi(k)$ signals at the Zn K-edge of ZnFe₂O₄ and their corresponding Fourier transforms. The signal in k-space is slightly suppressed as the cell is discharged to 1.2 V, see Figure 6a, after which it varies with continuous discharge to 0.7 V. Small changes can be observed upon further discharge to 0.02 V and subsequent charge to 3.0 V in the 1st and 2nd cycle, which are more pronounced in the corresponding Fourier transformed EXAFS data in Figure 6b. In the spectrum of pristine ZnFe₂O₄, three peaks centered at $R \sim 1.6$ Å, ~ 2.6 Å and ~ 3.1 Å can be observed. This observation is in good agreement with the results on nano-crystalline ZnFe₂O₄ powder reported by Oliver *et al.*[24], according to which 55% of the Zn²⁺ ions occupy tetrahedral sites and 45% of Zn²⁺ are located at octahedral sites. As the cell is discharged to 1.2 V, no obvious changes can be seen except the slightly reduced peak intensity. With further discharge to 0.7 V, only the first Zn-O peak and two small Zn-Zn_{metal} (~ 2.2 Å) and Zn-Zn (~ 2.7 Å) peaks can be observed. They remain the same during subsequent discharge to 0.02 V in the 1st and 2nd cycle. As for the fully charged samples in the first two cycles, the intensity of the Zn-Zn_{metal} peak decreases along with the cycle number while an opposite trend can be observed for the Zn-Zn peak.

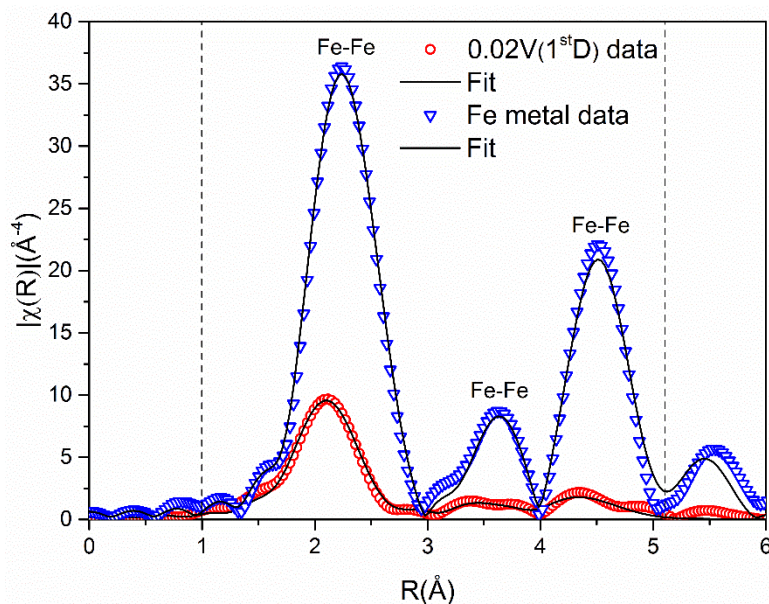


Figure 7. Comparison of EXAFS fits to the data measured at the Fe K-edge of ZnFe₂O₄ electrode discharged to 0.02 V and pure iron metal foil. Short dot lines indicate the fitting range.

A comparison of the Fe K-edge Fourier transforms between the ZnFe₂O₄ electrode discharged to 0.02 V (1st cycle) and pure iron metal foil is shown in Figure 7. The corresponding fit parameters

3.3 Nano-crystalline ZnFe₂O₄ anode

are listed in Table 1. The structure of iron metal is used (space group: $Im\bar{3}m$) and the data is in good agreement with theory as the R-factors of the fits are less than 0.02. The peaks corresponding to Fe-O distances in ZnFe₂O₄ are missing as the cell is discharged (= lithiated), indicating the absence of oxygen atoms during lithiation. Similar results have also been observed during the electrochemical reaction of Li and Na with a negative NiCo₂O₄ electrode[29] and in our former work in a NiFe₂O₄ electrode[31]. With continuous lithiation of the NiCo₂O₄ electrode, only one strong Co-Co and Ni-Ni peak can be observed at the end of discharge. Unfortunately, the data measured at the Zn K-edge for the ZnFe₂O₄ electrode during cycling cannot be fitted with the proposed model structure because of the complexity of the reaction between lithium and ZnO, and the large disorder introduced in the structure during the conversion reaction.

Table 1. Fe EXAFS fit results for a reference Fe metal foil and the ZnFe₂O₄ sample discharged to 0.02 V in the 1st cycle.

Fe metal foil			ZnFe ₂ O ₄			
			0.02V(1 st D)			
Path	N_{degen}	$R_{fit}(\text{\AA})$	$\sigma_{fit}^2(\text{\AA}^2)$	N_{degen}	$R_{fit}(\text{\AA})$	$\sigma_{fit}^2(\text{\AA}^2)$
Fe-Fe	8	2.463(4)	0.005(1)	8.4(8)	2.463(5)	0.013(1)
Fe-Fe	6	2.835(6)	0.006(1)	6	2.835(8)	0.026(3)
Fe-Fe	12	4.042(4)	0.008(1)	12	4.059(16)	0.027(2)
Fe-Fe	24	4.739(5)	0.008(1)	24	4.759(19)	0.027(2)
Fe-Fe	8	4.951(5)	0.008(1)	8	4.971(20)	0.027(2)

4. Discussion

It has been widely accepted that the features of the absorption edge (energy position and shape of the edge) measured by XANES spectroscopy indicate the density of states, chemical bonding, valence state and crystal or cluster symmetry of the absorbing atom[32-35]. The edge features will shift to lower energy as the valence state of absorbing atom decreases and vice versa. This can be realized by the Fe and Zn K-edge XANES data in Figure 4. The shifts and changes of the

3.3 Nano-crystalline ZnFe₂O₄ anode

absorption edges at the Fe K-edge in Figure 4a and 4b manifest the reduction of Fe³⁺ ions during lithiation. When the cell is discharged to 0.02 V in the 1st and 2nd cycle, the absorption edge is identical with that of iron foil, indicating a reversible formation of metallic iron during lithiation. The movement of the main edge to higher energy for the charged (= de-lithiated) samples in the 2nd cycle reveals the oxidation of metallic iron. Differences of the edge features between samples charged to 3.0 V in the 1st and 2nd cycle reflect the existence of different local environments around Fe atoms due to the incomplete oxidation of the metallic iron in the first cycle[30]. In contrast, only small changes can be observed at the Zn K-edge XANES spectra in Figure 4c and 4d during cycling. The appearance of the peak at ~9665 eV indicates the formation of LiZn alloy during discharge[36], which shows a typical metallic bond character with a broad and smooth absorption line. The remaining peak at ~9668 eV corresponds to the unreacted Zn²⁺ ions in the electrode. The persistence of the two peaks during lithiation and de-lithiation points at a co-existence of ZnO and LiZn phases during cycling. Unfortunately, the peak at ~9666 eV caused by the formation of metallic zinc can hardly be recognized in both Figure 4c and 4d due to an overlap of the peaks and limited energy resolution.

A schematic illustration of the possible structure evolution of a nano-crystalline ZnFe₂O₄ electrode during the 1st discharge and charge cycle is given in Figure 8. When the cell is discharged to 1.2 V in the 1st cycle, accounting to a specific capacity of 18 mAh g⁻¹ or a lithium uptake of 0.16 per unit of nano-crystalline ZnFe₂O₄, no clear changes can be observed at both the Fe and Zn K-edges except for a small amplitude reduction in EXAFS. This can be expected as the inserted lithium ions will increase disorder of the structure due to interactions between different cations. With further discharge to 0.7 V, corresponding to 7 lithium ions inserted into the structure, the spinel structure collapses and converts to different phases. The strong Fe-Fe_{metal} peak in Figure 5b reflects the formation of metallic iron while the Zn-O and Zn-Zn_{metal} signal in Figure 6b implies the co-existence of ZnO and metallic Zn phases in the electrode.

Decomposition of lithiated transition oxides to Li₂O and the formation of a new rock-salt monoxide phase with further lithiation has been reported[1, 15, 37, 38]. Bresser *et al.*[7] found that the XRD pattern of carbon-coated ZnFe₂O₄ particles measured *in-situ* during lithiation fitted well to those of ZnO and Fe_{0.99}O with a slight shift to higher 2 θ values. They attributed the shift of the XRD pattern to the formation of a distorted cubic Zn_xFe_yO phase, having an x:y ratio of 1:2 (and x + y \approx 1). Upon further lithiation, the reflections vanished and no features could be

3.3 Nano-crystalline ZnFe₂O₄ anode

observed due to the formation of a fully amorphous phase consisting of highly dispersed LiZn and metallic iron in an amorphous Li₂O matrix[10]. In our system, we propose that, instead of the cubic Zn_xFe_yO phase, the lithiated spinel phase ZnFe₂O₄ converts to FeO and ZnO phases and then the monoxide phases are reduced to the metallic state during lithiation as shown in Figure 8. If this was not true, a strong Fe-O peak should be observed in Figure 5b as the cell is the first discharged to 0.02 V due to the intensive Zn-O peak in Figure 6b at the same voltage.

According to the refined structure parameters in Table 1, it is clear that the metallic iron formed at 0.02 V has the same number of nearest neighbors in the 1st coordination shell as the reference iron foil. However, the refined Debye-Waller factor σ^2 of the coordinate shells is much higher than that of the iron foil, indicating the presence of high disorder in the newly formed metallic iron phase. The EXAFS data of Zn K-edge proves that, unlike FeO, the ZnO newly formed during the 1st lithiation is partially reduced to the metallic state and then is alloying with lithium when the cell is discharged to 0.02 V. However, the reason why FeO and ZnO phases show a different reactivity to lithium ions in the 1st lithiation step is has not yet been clarified and requires more attention in the future.

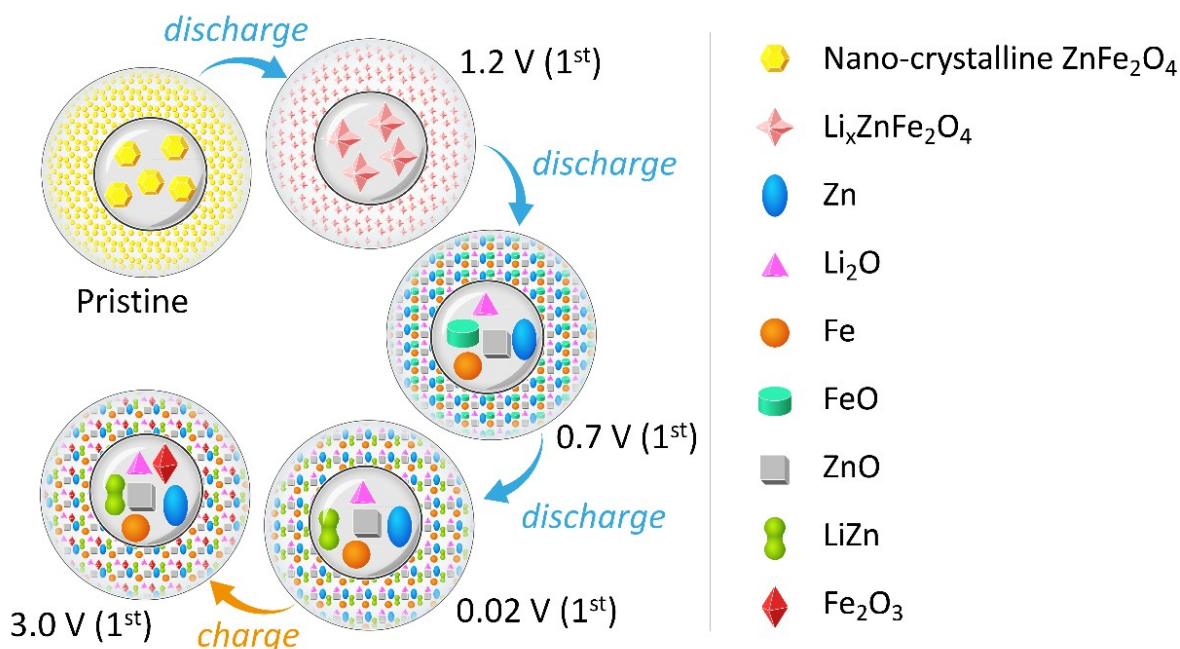


Figure 8. Schematic illustrations of the possible structure evolution of the nano-crystalline ZnFe₂O₄ electrode during the 1st discharge/charge cycle.

3.3 Nano-crystalline ZnFe₂O₄ anode

During the first de-lithiation, a capacity of 780 mAh g⁻¹ is achieved, which corresponds to 7 lithium atoms released per unit cell. Only small changes can be observed in the XANES and EXAFS data at both the Fe and Zn K-edges as the cell is charged, which implies that the metallic iron and zinc atoms are partially re-oxidized during the 1st de-lithiation. SEI decomposition during charge within the first few cycles has already been reported for many other 3d transition metal oxides, such as Cu₂O, CuO and NiO[39-41]. Therefore, it is reasonable to assume that the de-lithiation capacity may come from the decomposition of the SEI layer to some extent, which needs more detailed investigation in future. After the cell is activated in the first cycle, a reversible reaction between the metal oxide and lithium can be observed in the second lithiation and de-lithiation step in Figure 5 and Figure 6. The oxidation of metallic iron to Fe₂O₃ and metallic zinc to ZnO can be deduced from both XANES and EXAFS results as the cell is charged to 3.0 V in the 2nd cycle, which is in good agreement with the results from the cyclic voltammograms shown in Figure 3 and results reported about other spinel electrodes[42-44]. The improvement of the redox reaction activities between lithium and transition metal oxides in the 2nd cycle maybe attributed to the formation of the stable SEI during cycling.

5. Conclusions

The electronic and local structural modifications around Fe and Zn atoms in the spinel ferrite ZnFe₂O₄ anode material at various states-of-charge during the 1st and 2nd cycle were investigated by XRD, SEM, cyclic voltammogram (CV) and X-ray absorption spectroscopy. Both the absorbing components Fe and Zn are reduced to the metallic state during lithiation and re-oxidized in the subsequent de-lithiation. The reversibility of the redox reaction between lithium and transition metal oxides are strongly improved in the 2nd cycle. At the beginning of discharging the cell to 1.2 V, the inserted lithium ions first occupy the empty sites of the structure. With increasing insertion of lithium ions, the matrix collapses and converts to rock-salt phases FeO and ZnO. A mixture of metallic iron, ZnO, metallic zinc, LiZn and Li₂O phases were attained at the end of discharge (= lithiation). The refined EXAFS result reveals that the reduced metallic iron particles contain a large degree of disorder. During subsequent de-lithiation in the 1st cycle, the metallic particles are partially re-oxidized to Fe₂O₃ and ZnO. Unlike FeO, only parts of the newly formed rock-salt ZnO phase seem to be reactive with the inserted lithium ions. Formation of the SEI layer in the initial cycles significantly contributes to the irreversible

3.3 Nano-crystalline ZnFe₂O₄ anode

capacity of the electrode. The inactive disordered ZnO phase in the electrode is partially responsible for the poor electrochemical behavior of a ZnFe₂O₄ electrode.

Acknowledgements

Allocation of beamtime at KMC-2, BESSY-II, Berlin, Germany, is gratefully acknowledged. The authors would also like to thank Stefan Zander for technical support at KMC-2 beamline, and the financial support from China Scholarship Council.

References

- [1] P. Poizot, S. Laruelle, S. Grugeon, L. Dupont, J.M. Tarascon, Nano-sized transition-metal oxides as negative-electrode materials for lithium-ion batteries, *Nature*. 407 (2000) 496-499.
- [2] J.O. Besenhard, M. Winter, Advances in Battery Technology: Rechargeable Magnesium Batteries and Novel Negative-Electrode Materials for Lithium Ion Batteries, *ChemPhysChem*. 3 (2002) 155-159.
- [3] M. Winter, J.O. Besenhard, Lithiated carbons, in: J.O. Besenhard (Ed.) *Handbook of Battery Materials*, Wiley-VCH, Weinheim, 1999, pp. 383-418.
- [4] H. Jia, R. Kloepsch, X. He, M. Evertz, S. Nowak, J. Li, M. Winter, T. Placke, Nanostructured ZnFe₂O₄ as Anode Material for Lithium Ion Batteries: Ionic Liquid-Assisted Synthesis and Performance Evaluation with Special Emphasis on Comparative Metal Dissolution, *Acta Chim Slov*. 63 (2016) 470-483.
- [5] P. Meister, H. Jia, J. Li, R. Kloepsch, M. Winter, T. Placke, Best Practice: Performance and Cost Evaluation of Lithium Ion Battery Active Materials with Special Emphasis on Energy Efficiency, *Chem Mater*. 28 (2016) 7203-7217.
- [6] J. Cabana, L. Monconduit, D. Larcher, M.R. Palacín, Beyond Intercalation-Based Li-Ion Batteries: The State of the Art and Challenges of Electrode Materials Reacting Through Conversion Reactions, *Adv Mater*. 22 (2010) E170-E192.
- [7] D. Bresser, E. Paillard, R. Kloepsch, S. Krueger, M. Fiedler, R. Schmitz, D. Baither, M. Winter, S. Passerini, Carbon Coated ZnFe₂O₄ Nanoparticles for Advanced Lithium-Ion Anodes, *Advanced Energy Materials*. 3 (2013) 513-523.
- [8] M. Winter, The Solid Electrolyte Interphase – The Most Important and the Least Understood Solid Electrolyte in Rechargeable Li Batteries, *Zeitschrift für Physikalische Chemie*. (2009), pp. 1395.
- [9] J.-M. Tarascon, S. Grugeon, M. Morcrette, S. Laruelle, P. Rozier, P. Poizot, New concepts for the search of better electrode materials for rechargeable lithium batteries, *Comptes Rendus Chimie*. 8 (2005) 9-15.
- [10] X. Guo, X. Lu, X. Fang, Y. Mao, Z. Wang, L. Chen, X. Xu, H. Yang, Y. Liu, Lithium storage in hollow spherical ZnFe₂O₄ as anode materials for lithium ion batteries, *Electrochem Commun*. 12 (2010) 847-850.
- [11] J.M. Won, S.H. Choi, Y.J. Hong, Y.N. Ko, Y.C. Kang, Electrochemical properties of yolk-shell structured ZnFe₂O₄ powders prepared by a simple spray drying process as anode material for lithium-ion battery, *Sci Rep*. 4 (2014) 5857.

3.3 Nano-crystalline ZnFe₂O₄ anode

- [12] D. Zhao, Y. Xiao, X. Wang, Q. Gao, M. Cao, Ultra-high lithium storage capacity achieved by porous ZnFe₂O₄/ α -Fe₂O₃ micro-octahedrons, *Nano Energy*. 7 (2014) 124-133.
- [13] J. Xie, W. Song, G. Cao, T. Zhu, X. Zhao, S. Zhang, One-pot synthesis of ultrafine ZnFe₂O₄ nanocrystals anchored on graphene for high-performance Li and Li-ion batteries, *RSC Advances*. 4 (2014) 7703-7709.
- [14] L. Yao, X. Hou, S. Hu, J. Wang, M. Li, C. Su, M.O. Tade, Z. Shao, X. Liu, Green synthesis of mesoporous ZnFe₂O₄/C composite microspheres as superior anode materials for lithium-ion batteries, *J Power Sources*. 258 (2014) 305-313.
- [15] D. Larcher, G. Sudant, J.-B. Leriche, Y. Chabre, J.-M. Tarascon, The Electrochemical Reduction of Co₃O₄ in a Lithium Cell, *J Electrochem Soc*. 149 (2002) A234-A241.
- [16] B.K. Teo, EXAFS: Basic Principles and Data Analysis, Springer, Berlin, 1986.
- [17] S.D. Kelly, K.M. Kemner, J.B. Fein, D.A. Fowle, M.I. Boyanov, B.A. Bunker, N. Yee, X-ray absorption fine structure determination of pH-dependent U-bacterial cell wall interactions, *Geochim Cosmochim Acta*. 66 (2002) 3855-3871.
- [18] B. Ravel, M. Newville, ATHENA, ARTEMIS, HEPHAESTUS: data analysis for X-ray absorption spectroscopy using IFEFFIT, *J Synchrotron Radiat*. 12 (2005) 537-541.
- [19] A.L. Ankudinov, B. Ravel, J.J. Rehr, S.D. Conradson, Real-space multiple-scattering calculation and interpretation of x-ray-absorption near-edge structure, *Phys Rev B*. 58 (1998) 7565-7576.
- [20] L. Yao, X. Hou, S. Hu, Q. Ru, X. Tang, L. Zhao, D. Sun, A facile bubble-assisted synthesis of porous Zn ferrite hollow microsphere and their excellent performance as an anode in lithium ion battery, *J Solid State Electrochem*. 17 (2013) 2055-2060.
- [21] X.H. Huang, X.H. Xia, Y.F. Yuan, F. Zhou, Porous ZnO nanosheets grown on copper substrates as anodes for lithium ion batteries, *Electrochim Acta*. 56 (2011) 4960-4965.
- [22] C.T. Cherian, J. Sundaramurthy, M. Kalaivani, P. Ragupathy, P.S. Kumar, V. Thavasi, M.V. Reddy, C.H. Sow, S.G. Mhaisalkar, S. Ramakrishna, B.V.R. Chowdari, Electrospun α -Fe₂O₃ nanorods as a stable, high capacity anode material for Li-ion batteries, *J Mater Chem*. 22 (2012) 12198-12204.
- [23] F. Zou, X. Hu, Z. Li, L. Qie, C. Hu, R. Zeng, Y. Jiang, Y. Huang, MOF-Derived Porous ZnO/ZnFe₂O₄/C Octahedra with Hollow Interiors for High-Rate Lithium-Ion Batteries, *Adv Mater*. 26 (2014) 6622-6628.

3.3 Nano-crystalline ZnFe₂O₄ anode

- [24] S.A. Oliver, V.G. Harris, H.H. Hamdeh, J.C. Ho, Large zinc cation occupancy of octahedral sites in mechanically activated zinc ferrite powders, *Appl Phys Lett.* 76 (2000) 2761-2763.
- [25] S. Nakashima, K. Fujita, K. Tanaka, K. Hirao, T. Yamamoto, I. Tanaka, First-principles XANES simulations of spinel zinc ferrite with a disordered cation distribution, *Phys Rev B.* 75 (2007) 174443.
- [26] M.J. Akhtar, M. Nadeem, S. Javaid, M. Atif, Cation distribution in nanocrystalline ZnFe₂O₄ investigated using x-ray absorption fine structure spectroscopy, *Journal of Physics: Condensed Matter.* 21 (2009) 405303.
- [27] V.G. Harris, N.C. Koon, C.M. Williams, Q. Zhang, M. Abe, J.P. Kirkland, Cation distribution in NiZn-ferrite films via extended x-ray absorption fine structure, *Appl Phys Lett.* 68 (1996) 2082-2084.
- [28] B. Jeyadevan, K. Tohji, K. Nakatsuka, Structure analysis of coprecipitated ZnFe₂O₄ by extended x-ray-absorption fine structure, *J Appl Phys.* 76 (1994) 6325-6327.
- [29] A.V. Chadwick, S.L.P. Savin, S. Fiddy, R. Alcántara, D. Fernández Lisboa, P. Lavela, G.F. Ortiz, J.L. Tirado, Formation and Oxidation of Nanosized Metal Particles by Electrochemical Reaction of Li and Na with NiCo₂O₄: X-ray Absorption Spectroscopic Study, *J Phys Chem C.* 111 (2007) 4636-4642.
- [30] G. Balachandran, D. Dixon, N. Bramnik, A. Bhaskar, M. Yavuz, L. Pfaffmann, F. Scheiba, S. Mangold, H. Ehrenberg, Elucidation of the Electrochemical Reaction Mechanism in MFe₂O₄ (M=Ni, Co) Conversion-Type Negative Electrode Systems by using In Situ X-ray Absorption Spectroscopy, *ChemElectroChem.* 2 (2015) 1510-1518.
- [31] D. Zhou, S. Permien, J. Rana, M. Krenzel, F. Sun, G. Schumacher, W. Bensch, J. Banhart, Investigation of electronic and local structural changes during lithium uptake and release of nanocrystalline NiFe₂O₄ by X-ray absorption spectroscopy, *J Power Sources.* 342 (2017) 56-63.
- [32] E.A. Stern, Theory of the extended x-ray-absorption fine structure, *Phys Rev B,* 10 (1974) 3027-3037.
- [33] P.A. Lee, J.B. Pendry, Theory of the extended x-ray absorption fine structure, *Phys Rev B.* 11 (1975) 2795-2811.
- [34] J.J. Rehr, E.A. Stern, R.L. Martin, E.R. Davidson, Extended x-ray-absorption fine-structure amplitudes—Wave-function relaxation and chemical effects, *Phys Rev B.* 17 (1978) 560-565.
- [35] E.A. Stern, B.A. Bunker, S.M. Heald, Many-body effects on extended x-ray absorption fine structure amplitudes, *Phys Rev B.* 21 (1980) 5521-5539.

3.3 Nano-crystalline ZnFe₂O₄ anode

- [36] C.J. Pelliccione, Y. Ding, E.V. Timofeeva, C.U. Segre, In Situ XAFS Study of the Capacity Fading Mechanisms in ZnO Anodes for Lithium-Ion Batteries, *J Electrochem Soc.* 162 (2015) A1935-A1939.
- [37] M.M. Thackeray, W.I.F. David, J.B. Goodenough, Structural characterization of the lithiated iron oxides $\text{Li}_x\text{Fe}_3\text{O}_4$ and $\text{Li}_x\text{Fe}_2\text{O}_3$ ($0 < x < 2$), *Mater Res Bull.* 17 (1982) 785-793.
- [38] C.J. Chen, M. Greenblatt, J.V. Waszczak, Lithium insertion into spinel ferrites, *Solid State Ionics.* 18–19, Part 2 (1986) 838-846.
- [39] A. Débart, L. Dupont, P. Poizot, J.-B. Leriche, J.M. Tarascon A Transmission Electron Microscopy Study of the Reactivity Mechanism of Tailor-Made CuO Particles toward Lithium, *J Electrochem Soc.* 148 (2001) A1266-A1274.
- [40] S. Grugeon, S. Laruelle, R. Herrera-Urbina, L. Dupont, P. Poizot, J.-M. Tarascon, Particle Size Effects on the Electrochemical Performance of Copper Oxides toward Lithium, *J Electrochem Soc.* 148 (2001) A285-A292.
- [41] X.H. Huang, J.P. Tu, B. Zhang, C.Q. Zhang, Y. Li, Y.F. Yuan, H.M. Wu, Electrochemical properties of NiO–Ni nanocomposite as anode material for lithium ion batteries, *J Power Sources.* 161 (2006) 541-544.
- [42] R. Alcántara, M. Jaraba, P. Lavela, J.L. Tirado, J.C. Jumas, J. Olivier-Fourcade, Changes in oxidation state and magnetic order of iron atoms during the electrochemical reaction of lithium with NiFe₂O₄, *Electrochem Commun.* 5 (2003) 16-21.
- [43] P. Lavela, J.L. Tirado, CoFe₂O₄ and NiFe₂O₄ synthesized by sol–gel procedures for their use as anode materials for Li ion batteries, *J Power Sources.* 172 (2007) 379-387.
- [44] J.L. Tirado, P. Lavela, C. Pérez Vicente, B. León, C. Vidal-Abarca, Unfolding the role of iron in Li-ion conversion electrode materials by ⁵⁷Fe Mössbauer spectroscopy, *Hyperfine Interact.* 207 (2012) 53-59.

4 Conclusions

In the present work, electronic and local structural changes of three different anode systems at various states-of-charge are investigated by X-ray absorption spectroscopy. The main findings can be summarized as followings:

- The large reversible capacity of porous NiSi₂/Si composite anodes is mainly attributed to the alloying/de-alloying reaction between lithium and the silicon component during the lithiation/de-lithiation process. A small fraction of NiSi₂ in the composite reacts with lithium reversibly forming a non-stoichiometric compound NiSi_{2-y} and an amorphous Li_xSi_y phase, which can contribute to the capacity to some extent. Apart from that, NiSi₂ is primarily used as a buffer matrix to alleviate the huge volume changes arising from alloying during cycling.
- The lithium storage mechanism of the nano-crystalline inverse spinel ferrite NiFe₂O₄ anode material is shown to be based on the redox reaction between lithium and transition metal oxides during the 1st cycle. At the beginning of lithiation, prior to Ni²⁺, iron ions on the tetrahedral site are reduced from +3 to +2 and forced to move to empty octahedral sites in the spinel due to the strong repulsive interactions between Li⁺ and Fe²⁺. With further lithiation, the spinel matrix is first converted to a rock-salt monoxide phase and then reduced to metallic iron and nickel nanoparticles of a highly disordered structure. Part of the inserted lithium ions are probably consumed by the formation of solid electrolyte interface (SEI) and other side reactions during the conversion reactions. The metallic iron and nickel have numbers of nearest neighbors of 6.0(8) and 8.1(4), respectively, which are largely suppressed compared to that of the pure iron and nickel metals. Instead of forming NiFe₂O₄, the metal particles are re-oxidized to Fe₂O₃ and NiO, respectively, during the subsequent charge process.
- As for the nano-crystalline ZnFe₂O₄ anode material, a mixture of metallic iron, ZnO, metallic zinc, LiZn and Li₂O phases are formed as the cell is deeply lithiated in the 1st cycle. During subsequent de-lithiation, the metallic particles are partially re-oxidized to Fe₂O₃ and ZnO phases, respectively. The formation of the SEI layer in the initial cycles contributes a lot to the irreversible capacity loss of the electrode. The reversibility of the

redox reaction between lithium and transition metal oxides strongly improves in the 2nd cycle. During the 1st lithiation process, the spinel ZnFe_2O_4 collapses and converts to FeO and ZnO. However, unlike FeO, ZnO phase is only partially reduced with further lithiation. The reason for the uncomplete reduction of ZnO has not yet been clarified. The inactive ZnO phase in the electrode could be the main reason of the poor electrochemical behavior of the electrode.

5 Outlook

The following issues need to be addressed in the future:

- (1) It has been observed that the ZnO phase formed during the 1st lithiation of the nano-crystalline ZnFe₂O₄ electrode shows a different redox activity compare to the FeO phase, which may contribute a lot to the irreversible capacity of the electrode. It is important to find out the reason why ZnO is only partially reactive to the inserted lithium in the 1st cycle in order to develop new ZnFe₂O₄ anode with better electrochemical behavior.
- (2) It is necessary to investigate a series of NiFe₂O₄ and ZnFe₂O₄ anodes with various particle size to clarify the capacity fading mechanism of these materials and the relation between the particle size of the active materials and structural changes during cycling.
- (3) It would be interesting to investigate the electrochemical performance and structural changes in other spinel anode systems such as MgFe₂O₄, MnFe₂O₄, CuFe₂O₄ or Zn_{1-x}Mn_xFe₂O₄ in order to understand the charge compensation mechanism during lithiation/de-lithiation with changing of cation ions within the spinel.

6 Acknowledgements

I would like to thank my advisor Prof. John Banhart and Prof. Gerhard Schumacher for giving me the opportunity to pursue my Ph.D at Helmholtz Zentrum Berlin. I also thank Prof. Dr. Christiane Stephan and Dr. Tobias Placke for being the evaluators of my thesis. I would like to take this opportunity to express my sincere gratitude to Prof. Gerhard Schumacher and Dr. Jatinkumar Rana, who always support my ideas and offer me selfless help.

I would like to thank my colleagues Tobias Scherb, Andrea Fantin, De Ning, Li Zhang, Fu Sun and Florian Vogel for their assistance on both scientific and other occasions. I would like to thank other members of our group such as Claudia Leistner and Christiane Föster for their help in my experiments. My special thanks to Ms. Ciceron for helping me with all paper-work throughout my Ph.D.

I would like to thank Haiping Jia, Tobias Placke and Richard Kloepsch from Prof. Martin Winter's group in University of Münster for providing me samples for my thesis. Likewise, Stefan Permien from Prof. Wolfgang Bensch's group in Kiel University is also acknowledged.

I would like to thank for the financial support from China Scholarship Council.

Finally, I would like to thank my parents and my wife for supporting me all the way. Without their sacrifice and love, I could not have reached so far.

Erklärung

Ich erkläre hiermit, dass ich die vorliegende Dissertation selbst verfasst und keine anderen als die angegebenen Quellen und Hilfsmittel verwendet habe.

Berlin, 2017

Dong Zhou